NONLINEAR TRAVELLING WAVE SOLUTIONS IN SQUARE DUCT FLOW

Shinya Okino

Abstract

Incompressible viscous flow through a straight duct with a square cross section driven by a constant pressure gradient is believed to be linearly stable as in the case of pipe flow and plane Couette flow. Therefore, there exists no solution which bifurcates from the laminar state and the transition to turbulence is abruptly caused by a finite amplitude disturbance. The turbulent state for these flows is considered to be represented by the trajectory in the phase space wandering around unstable nonlinear solutions, which are disconnected to the laminar state. While a number of nonlinear solutions have been published in pipe flow and plane Couette flow, only three nonlinear solutions have been reported so far in square duct flow (Wedin *et al.*, *Phys. Rev.* E **79**, 065305, 2009; Uhlmann *et al.*, *Phys. Fluids* **22**, 084102, 2010; Okino *et al.*, *J. Fluid Mech.* **657**, 413-429, 2010).

In this thesis, a number of nonlinear travelling wave solutions in square duct flow are presented. The first solution is discovered by a continuation approach from internally heated flow. The linear stability shows this solution is unstable from its onset. The next two solutions emerge from the first one via symmetry breaking bifurcations. We find one of them seems to be embedded in the laminar-turbulent boundary. The others are obtained by a continuation method using artificial body forces, which is invented by Waleffe, *Phys. Rev. Lett.* **81**, 4140-4143 (1998). The richness of the nonlinear solutions implies the complexity of the phase space and these solutions are expected to be the fundamental building blocks of turbulence in a square duct. Moreover, striking similarity between the solutions in square duct flow and pipe flow is shown throughout the thesis.

Acknowledgements

I would like to thank my supervisor Prof. Dr. Masato Nagata for his guidance and encouragement during my PhD course. He introduced me to the interesting and challenging field of mathematical science, and always gave me appropriate advices throughout my study for this thesis.

I would also like to thank Dr. Håkan Wedin and Prof. Dr. Alessandro Bottaro at DICAT, University of Genova for the stimulating discussion.

Finally, I would like to thank my father, Masuwo Okino, and my mother, Tomoko Okino for their cordial support and understanding.

Shinya Okino

Contents

List of Figures

List of Tables

Chapter 1

Introduction

How do shear flows become turbulent? Transition to turbulence in canonical unidirectional shear flows is still an unsolved problem in fluid mechanics since the pioneering experimental study on pipe flow by Osborne Reynolds in 1883. The difficulty consists in extracting relevant information from the Navier-Stokes equations to describe turbulence, which is unsteady three-dimensional chaotic motion of viscous fluid. The routes to turbulence are basically divided into two types, depending on the linear stability of the laminar flow. The linear stability theory tells us whether the flow is asymptotically stable to infinitesimal perturbations. For linearly unstable flows such as Taylor-Couette flow and Rayleigh-Bénard convection, the onset of transition is predictable by the linear stability analysis of the laminar state (see e.g. Drazin & Reid 1981) and transition to turbulence is understood as a sequence of bifurcations of the nonlinear flow states.

The laminar flow through square duct is asymptotically stable to small disturbances (Tatsumi & Yoshimura 1990) as well as circular pipe flow (e.g. Davey & Drazin 1969; Salwen 1972, 1980; Meseguer & Trefethen 2003) and plane Couette flow (Romanov 1973). Hence to cause a shift from a laminar to a turbulent state for these flow cases a finite amplitude disturbance is necessary, and the threshold amplitude is a function of the disturbance shape. The experimental work by Dabyshire & Mullin (1995) on pipe flow demonstrates that the required finite-amplitude disturbance ϵ to initiate the transition to turbulence in circular pipe flow, scales like Re^{-1} - same scaling is reported in the experiments by Hof *et al.* (2003) in the range $2000 \leq Re \leq 20000$. This has also been theoretically recovered by Gavarini *et al.* (2005) on the same flow configuration. Likewise, Chapman (2002) postulates two scenarios of turbulence breakdown for plane Couette flow and plane Poiseuille flow using

asymptotic analysis of the Navier-Stokes equations. Therein it is found that ϵ scales in the interval $Re^{-1.5} \leq \epsilon \leq Re^{-1}$ depending on the postulated transition scenario and flow configuration. A similar result is obtained by Waleffe & Wang (2005) on plane Couette flow where the smallest disturbance amplitude needed to trigger transition scales as Re^{-1}.

The absence of a linear instability mechanisms has prevented the discovery of nonlinear solutions to linearly stable canonical flows such as plane Couette flow and circular pipe flow. However, Nagata (1986, 1988, 1990) found time-independent three-dimensional solutions to plane Couette flow for the first time by focusing on Taylor-Couette flow between co-rotating cylinders. The solutions to plane Couette flow were obtained by bringing down the system rotation to zero. His solution was reproduced by Clever & Busse (1992) and Waleffe (2003). Clever & Busse (1992) studied Rayleigh-Bénard convection subjected to a constant shear. Vanishing the temperature difference between the walls leads their three-dimensional solution to the solution in plane Couette flow. Waleffe (2003) obtained the same solution using the idea of a self-sustaining process (SSP) of turbulence proposed by Waleffe (1997, 1998). Later, several nonlinear solutions have been obtained for pipe flow, first by Faisst & Eckhardt (2003) using a continuation method similar to the one in Waleffe (1998), followed by Wedin & Kerswell (2004), Pringle & Kerswell (2007), Duguet, Pringle & Kerswell (2008), Duguet, Willis & Kerswell (2008) and Pringle *et al.* (2009).

The turbulent state is thought to be described by trajectories bouncing around unstable fixed points such as the travelling wave states initially discovered by Faisst & Eckhardt (2003) and Wedin & Kerswell (2004) for pipe flow. In linearly stable flows such equilibrium states, known as exact coherent structures (ECS), are disconnected from the laminar flow and are unstable in general (Kerswell & Tutty 2007). The ECS in Waleffe (2001, 2003) and the isolated unstable time-periodic solution in Kawahara & Kida (2001) in PCF are characterized by the same statistics as numerical turbulence. The nonlinear fixed points may thus provide information that could advance the understanding of turbulence, e.g. one could collect and classify these solutions and use them to describe the mean characteristics of a chaotic state. On the other hand the direct numerical simulations performed by Willis & Kerswell (2008) in pipe flow suggest that other types of solutions, of larger amplitude than those known, are needed in order to describe a fully turbulent flow and that the existing travelling waves are only related to transitional flows.

As far as the rectangular duct flow is concerned, the linear stability analysis performed by Tatsumi & Yoshimura (1990) shows the laminar flow is stable up to an aspect ratio of $A = 3.2$ of the rectangular cross section of the duct. It is only recently that nonlinear solutions for the square duct ($A = 1$) have been discovered by Wedin *et al.* (2009) and Uhlmann *et al.* (2010) by successfully adopting the SSP approach used in pipe flow. It is reported that the skin friction on the lower branch of the nonlinear solution by Wedin *et al.* (2009) has a value close to that obtained in direct numerical simulations by Uhlmann *et al.* (2007) and Biau & Bottaro (2009) at the transitional conditions. When the flow speed is sufficiently high, direct numerical simulations of square duct flow by Gavrilakis (1992), Huser & Biringen (1993), Uhlmann *et al.* (2007), Biau *et al.* (2008) and Pinelli *et al.* (2010) have all observed an eight-vortex mean flow with two vortices in each quadrant. For example, the study by Gavrilakis (1992) suggests that the secondary Reynolds stress terms cause this mean flow. The solution found by Uhlmann *et al.* (2010) also has the eight-vortex mean flow pattern, which is consistent with that of square duct turbulence. Recently, a linear stability analysis of vertical rectangular duct flow with an internal heat source performed by Uhlmann & Nagata (2006) has shown the parameter region in which the basic flow state becomes unstable for $A = 1$.

This thesis is organized as follows. In Chapter 2, we adopt an homotopy approach, alternative to the SSP, by adding the heat equation to the system. This is an extension of the linear stability analysis by Uhlmann & Nagata (2006). A new nonlinear solution to isothermal square duct is discovered by bringing the strength of the heat source to zero. The results in this chapter is published in Okino *et al.* (2010). Chapter 3 presents the result of linear stability of the solution obtained in Chapter 2. We calculate two asymmetric solutions, which emerge through symmetry breaking bifurcations. A comparison between one of the bifurcating solutions and the edge state of square duct flow is made thoroughly. Chapter 4 gives a various kinds of nonlinear solutions, where we introduce the artificial body forces in order to calculate the exact solutions in square duct flow. This approach is similar to Waleffe (1998, 2003). The similarity between the solutions in square duct flow and pipe flow is discussed. Finally, the thesis ends with the conclusion and the outlook for this study in Chapter 5.

Chapter 2

Nonlinear Analysis of Internally Heated Duct Flow

A new nonlinear travelling wave solution for a flow through an isothermal square duct is discovered. The solution is found by a continuation approach in parameter space, starting from a case where the fluid is heated internally. The Reynolds number for which the travelling wave emerges is much lower than that of the solutions discovered recently by an analysis based on the self-sustaining process (Wedin *et al.*, *Phys. Rev.* E **79**, 065305, 2009; Uhlmann *et al.*, *Phys. Fluids* **22**, 084102, 2010).

2.1 Mathematical formulation

2.1.1 Configuration and the governing equations

We consider the low speed motion of a fluid with the kinematic viscosity ν_*, the thermal diffusivity κ_* and the thermal expansion coefficient α_{T*} in a straight duct placed vertically in the gravity field. The temperature of all the four vertical walls are kept the same and constant. The cross section of the duct is a square with the side $2b_*$. The fluid is subject to internal heating which is homogeneously distributed with intensity q_*. We take the Cartesian coordinates with the origin at the centre of the duct. The x_*-axis is directed along the duct and the y_* and z_*-axes are parallel to the sides of the cross section, as shown in figure 2.1. Here, the subscript $*$ denotes dimensional quantity. With the Boussinesq approximation, the velocity $\boldsymbol{u}$, the pressure P and the temperature deviation T from the wall temperature are governed by the equation of continuity,

$$\nabla \cdot \boldsymbol{u} = 0, \tag{2.1}$$

the equation of momentum conservation,

$$\partial_t \boldsymbol{u} + (\boldsymbol{u}\cdot\nabla)\boldsymbol{u} = -\nabla P + \nabla^2 \boldsymbol{u} + T\boldsymbol{e}_x, \tag{2.2}$$

and the equation of energy conservation,

$$\partial_t T + (\boldsymbol{u}\cdot\nabla)T = Pr^{-1}(\nabla^2 T + 2Gr), \tag{2.3}$$

where $\boldsymbol{e}_i$ $(i = x, y, z)$ is the unit vector in the i-direction and all the variables have been non-dimensionalized by the length scale b_*, the time scale b_*^2/ν_*, the velocity scale ν_*/b_* and the temperature scale $\nu_*^2/(g_*\alpha_{T*}b_*^3)$, where g_* is the acceleration due to gravity. We have defined the Grashof number as:

$$Gr = \frac{g_*\alpha_{T*}q_*b_*^5}{2\nu_*^2\kappa_*}, \tag{2.4}$$

and the Prandtl number as:

$$Pr = \frac{\nu_*}{\kappa_*}. \tag{2.5}$$

The electrically conducting aqueous solution of $ZnCl_2$ is often used for internal heating experiments where the heat is released by currents. For 20% in weight aqueous solution of $ZnCl_2$, $Pr = 8.7$ at 20°C and $Pr = 6.08$ at 40°C (Generalis & Nagata 2003). Throughout this study we fix $Pr = 7$.

The no-slip condition for the velocity and the isothermal condition for the temperature are imposed on the wall:

$$\boldsymbol{u} = \boldsymbol{0},\ T = 0 \quad \text{at} \quad y = \pm 1 \ \text{ and } \ z = \pm 1. \tag{2.6}$$

For the x-direction we impose periodicity over a wave length of $2\pi/\alpha$.

2.1.2 Laminar solution

The x-independent steady laminar solution, $\boldsymbol{u} = \boldsymbol{U}_B = U_B(y,z)\boldsymbol{e}_x, P = P_B = -\chi x$ and $T = T_B(y,z)$, to the governing equations (2.1)–(2.3) with the boundary condition (2.6) obeys

$$0 = \chi + T_B + \triangle_2 U_B, \tag{2.7}$$

$$0 = \triangle_2 T_B + 2Gr, \tag{2.8}$$

$$U_B = T_B = 0 \quad \text{at} \quad y = \pm 1 \ \text{ and } \ z = \pm 1, \tag{2.9}$$

where χ is the non-dimensional pressure drop and $\triangle_2 \equiv \partial_{yy}^2 + \partial_{zz}^2$. Let $U_{B\mathrm{iso}}(y,z)$ be the laminar velocity field in the isothermal case ($Gr = 0, T_B \equiv 0$) and define the Reynolds number using the centerline velocity:

$$Re = U_{B\mathrm{iso}}(0,0) = \frac{U_{B\mathrm{iso}*}(0,0)b_*}{\nu_*}. \tag{2.10}$$

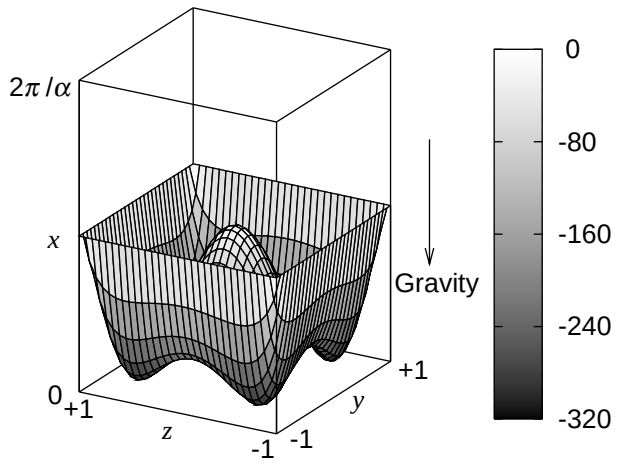

Figure 2.1: The configuration of the model with the laminar flow in grey scale at $Re = -3000$ and $Gr = 23000$.

The equations (2.7)–(2.9) are solved numerically. The proportionality of the pressure drop to the Reynolds number obeys $\chi = 3.3935Re$ (see Tatsumi & Yoshimura 1990). According to Uhlmann & Nagata (2006), the laminar state is classified into five groups (M_1-M_5) depending on the Reynolds number and the Grashof number for the thermal case as shown in figure 2.2. The regions are symmetric with respect to the origin. The examples of the laminar flow in each region are plotted in figure 2.3. These types of the laminar flows are distinguished by the number of disjoint inflection curves, except for the distinction between M_2 and M_3. The inflection curve is defined as the set of the points in the cross section where the second derivative of the laminar flow profile in the direction of its gradient is zero:

$$\frac{\mathrm{d}^2 U_B}{\mathrm{d}\boldsymbol{n}^2} = 0, \tag{2.11}$$

where $\boldsymbol{n} = \nabla U_B / |\nabla U_B|$. In the region M_1, the laminar flow is similar to the purely pressure driven flow (isothermal case, $Gr = 0$). The flow has the four inflection curves, which attach to the corners (see the centre of the first row in figure 2.3). In the region M_2, the additional nine inflection curves (one circular curve at the centre and two elongated ones for each quadrant) appear. The region M_2 is also characterized by no reverse flow (see figure 2.1 and the left frame of the second row in figure 2.3). The inflectional pattern in the region M_3 is same as that of M_2. The difference is the flow in M_3 has reverse flow: both positive and negative flow occurs. When entering the region M_4, the

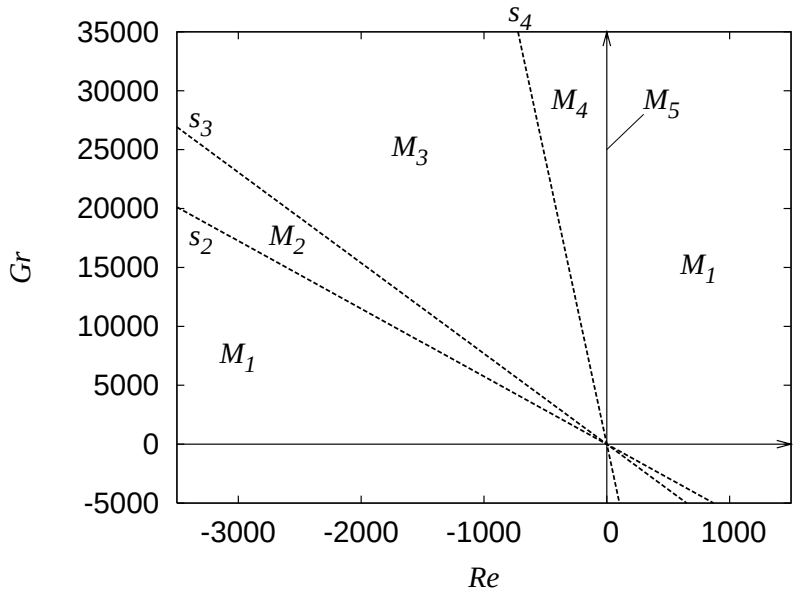

Figure 2.2: The regions in the Re–Gr plane where the laminar flow types M_i occur. The zone M_5 corresponds to the $Re = 0$ axis. The slopes s_i of the dividing lines defined by $Gr = s_i Re$ are given as follows: $s_2 = -5.75$, $s_3 = -7.69$ and $s_4 = -48.40$. Note that M_1 includes the $Gr = 0$ axis (isothermal case).

direction of the flow becomes fully upward and the inflection pattern changes into a single loop at the centre. In the region M_5 (the $Re = 0$ axis), the flow is characterized by the four inflection curves near the corners.

2.1.3 Disturbance equations

We superimpose disturbances, $\hat{\boldsymbol{u}}$, $\hat{p}$ and $\hat{\theta}$, on the laminar state, $U_B \boldsymbol{e}_x$, P_B and T_B, respectively. Disturbances are governed by the following equations:

$$\nabla \cdot \hat{\boldsymbol{u}} = 0, \tag{2.12}$$

$$\partial_t \hat{\boldsymbol{u}} + U_B \partial_x \hat{\boldsymbol{u}} + (\hat{\boldsymbol{u}} \cdot \nabla) U_B \boldsymbol{e}_x + (\hat{\boldsymbol{u}} \cdot \nabla)\hat{\boldsymbol{u}} = -\nabla \hat{p} + \hat{\theta} \boldsymbol{e}_x + \nabla^2 \hat{\boldsymbol{u}}, \tag{2.13}$$

$$\partial_t \hat{\theta} + U_B \partial_x \hat{\theta} + (\hat{\boldsymbol{u}} \cdot \nabla) T_B + (\hat{\boldsymbol{u}} \cdot \nabla)\hat{\theta} = Pr^{-1} \nabla^2 \hat{\theta}, \tag{2.14}$$

$$\hat{\boldsymbol{u}} = \boldsymbol{0},\ \hat{\theta} = 0 \quad \text{at} \quad y = \pm 1 \ \text{ and } \ z = \pm 1. \tag{2.15}$$

Disturbances $\hat{\boldsymbol{u}}$, $\hat{p}$, $\hat{\theta}$ are decomposed into their mean parts, $\hat{\boldsymbol{U}}(t, y, z)$, $\hat{P}(t, y, z)$, $\hat{\Theta}(t, y, z)$, and the residuals, $\check{\boldsymbol{u}}$, $\check{p}$, $\check{\theta}$, where $\hat{\boldsymbol{U}} \equiv \alpha/(2\pi) \int_0^{2\pi/\alpha} \hat{\boldsymbol{u}} \, \mathrm{d}x = (\hat{U}, \hat{V}, \hat{W})$, $\hat{P} \equiv \alpha/(2\pi) \int_0^{2\pi/\alpha} \hat{p} \, \mathrm{d}x$, $\hat{\Theta} \equiv \alpha/(2\pi) \int_0^{2\pi/\alpha} \hat{\theta} \, \mathrm{d}x$, and $\check{\boldsymbol{u}} = (\check{u}, \check{v}, \check{w})$. We consider the fixed pressure gradient constraint so that $\nabla \hat{P} = 0$.

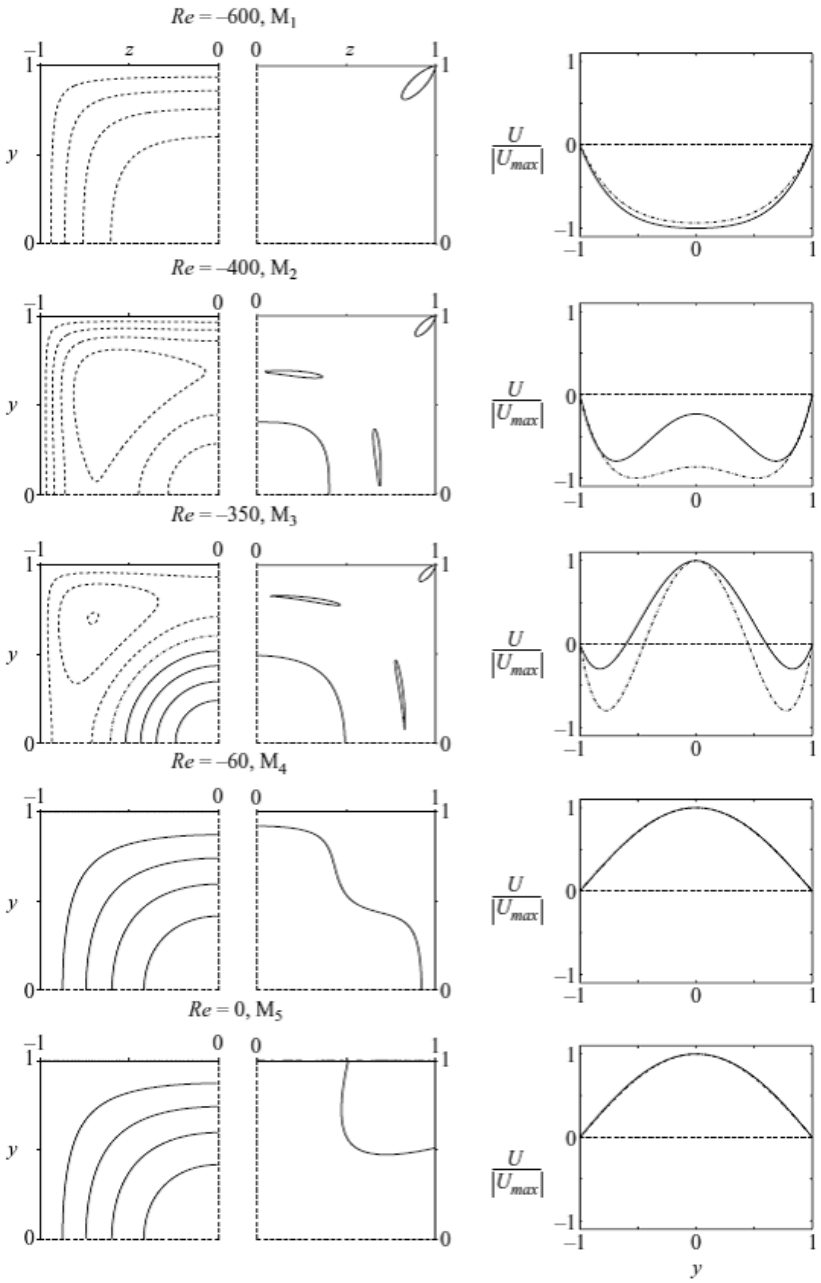

Figure 2.3: Figure 2 of Uhlmann & Nagata (2006). The five types of the laminar flows with $Gr = 3000$. (Left column) The isocontours of the laminar flow velocity at values $U_B/|U_{B,\max}| = -1, -0.8, \cdots, 0.8, 1$. Here, $U_{B,\max} = \max\{U_B(y,z)| -1 \le y \le +1, -1 \le z \le +1\}$. Positive and negative values are drawn by solid and dashed curves, respectively. (Centre column) The isocontours of $\mathrm{d}^2 U_B/\mathrm{d}\boldsymbol{n}^2 = 0$. As the laminar flow is doubly symmetric in y and z, only one quadrant is shown. (Right column) The velocity profiles on the centreline, $U_B(y,0)/|U_{B,\max}|$, are shown by the solid curves. The laminar flows when $A = \infty$ are drawn by the dashed curves for comparison.

First, we take the streamwise average of (2.12):

$$\partial_y \hat{V} + \partial_z \hat{W} = 0, \tag{2.16}$$

from which the stream function $\hat{\varphi}$ of the cross sectional mean flow $(\hat{V}, \hat{W})$ can be defined and satisfies

$$\hat{V} = \partial_z \hat{\varphi}, \quad \hat{W} = -\partial_y \hat{\varphi}. \tag{2.17}$$

Then subtracting (2.16) from (2.12), we obtain $\nabla \cdot \check{\boldsymbol{u}} = 0$. Solving for $\check{u}$ we have

$$\check{u} = -\partial_x^{-1}(\partial_y \check{v} + \partial_z \check{w}), \tag{2.18}$$

where the integrating operator with respect to x, $\partial_x^{-1} \equiv \int \mathrm{d}x$, is defined.

In the following we obtain equations for $\hat{U}$, $\hat{\varphi}$, $\hat{\Theta}$, $\check{v}$, $\check{w}$ and $\check{\theta}$. Operation of the streamwise average on $\boldsymbol{e}_x \cdot$(2.13), $\boldsymbol{e}_x \cdot \nabla \times$(2.13) and (2.14) followed by elimination of $\hat{V}, \hat{W}$ by (2.17) leads to

$$\partial_t \hat{U} + (\partial_z \hat{\varphi} \partial_y - \partial_y \hat{\varphi} \partial_z)\bar{U} - \hat{\Theta} - \triangle_2 \hat{U} + \partial_y \overline{\check{u}\check{v}} + \partial_z \overline{\check{u}\check{w}} = 0, \tag{2.19}$$

$$-(\partial_t + \partial_z \hat{\varphi} \partial_y - \partial_y \hat{\varphi} \partial_z - \triangle_2)\triangle_2 \hat{\varphi} + (\partial_{yy}^2 - \partial_{zz}^2)\overline{\check{v}\check{w}} + \partial_{yz}^2 \overline{\check{w}^2 - \check{v}^2} = 0, \tag{2.20}$$

$$\partial_t \hat{\Theta} + (\partial_z \hat{\varphi} \partial_y - \partial_y \hat{\varphi} \partial_z)\bar{\Theta} - Pr^{-1} \triangle_2 \hat{\Theta} + \partial_y \overline{\check{v}\check{\theta}} + \partial_z \overline{\check{w}\check{\theta}} = 0, \tag{2.21}$$

where $\overline{\cdot} \equiv \alpha/(2\pi) \int_0^{2\pi/\alpha} \cdot \, \mathrm{d}x$ and $\check{u}$ is given by (2.18). $\bar{U} = U_B + \hat{U}$ and $\bar{\Theta} = T_B + \hat{\Theta}$ are the streamwise mean flow and the mean temperature, respectively.

We eliminate $\check{p}$ by taking the rotation of (2.13). Operation of $\boldsymbol{e}_z \cdot \nabla \times$(2.13) and $\boldsymbol{e}_y \cdot \nabla \times$(2.13) leads to

$$\begin{aligned}
&\Big[\{\partial_t + (\bar{\boldsymbol{U}} \cdot \nabla) - \nabla^2 + \partial_y \hat{V}\}\partial_x - \partial_{yy}^2 \bar{U}\Big]\check{v} \\
&-\Big[\{\partial_t + (\bar{\boldsymbol{U}} \cdot \nabla) - \nabla^2 + \partial_y \hat{V}\}\partial_y + \partial_y \hat{W} \partial_z\Big]\check{u} \\
&\qquad +\Big(\partial_y \bar{U} \partial_z - \partial_z \bar{U} \partial_y - \partial_{yz}^2 \bar{U} + \partial_z \hat{V} \partial_x\Big)\check{w} \\
&\qquad\qquad -(\partial_t - \triangle_2)\partial_y \hat{U} - \partial_y (\hat{\boldsymbol{U}} \cdot \nabla)\bar{U} \\
&\qquad\qquad\quad +\partial_y(\hat{\Theta} + \check{\theta}) + \boldsymbol{e}_z \cdot \nabla \times \{(\check{\boldsymbol{u}} \cdot \nabla)\check{\boldsymbol{u}}\} = 0,
\end{aligned} \tag{2.22}$$

$$\begin{aligned}
&\Big[\{\partial_t + (\bar{\boldsymbol{U}} \cdot \nabla) - \nabla^2 + \partial_z \hat{W}\}\partial_x - \partial_{zz}^2 \bar{U}\Big]\check{w} \\
&-\Big[\{\partial_t + (\bar{\boldsymbol{U}} \cdot \nabla) - \nabla^2 + \partial_z \hat{W}\}\partial_z + \partial_z \hat{V} \partial_y\Big]\check{u} \\
&\qquad +\Big(\partial_z \bar{U} \partial_y - \partial_y \bar{U} \partial_z - \partial_{yz}^2 \bar{U} + \partial_y \hat{W} \partial_x\Big)\check{v} \\
&\qquad\qquad -(\partial_t - \triangle_2)\partial_z \hat{U} - \partial_z (\hat{\boldsymbol{U}} \cdot \nabla)\bar{U} \\
&\qquad\qquad\quad +\partial_z(\hat{\Theta} + \check{\theta}) - \boldsymbol{e}_y \cdot \nabla \times \{(\check{\boldsymbol{u}} \cdot \nabla)\check{\boldsymbol{u}}\} = 0,
\end{aligned} \tag{2.23}$$

where $\bar{\boldsymbol{U}} = (\bar{U}, \hat{V}, \hat{W})$. Subtraction of (2.21) from (2.14) gives

$$\partial_t \check{\theta} + (\bar{\boldsymbol{U}} \cdot \nabla)\check{\theta} + (\check{\boldsymbol{u}} \cdot \nabla)\bar{\Theta} + (\check{\boldsymbol{u}} \cdot \nabla)\check{\theta} - \partial_y \overline{\check{v}\check{\theta}} - \partial_z \overline{\check{w}\check{\theta}} = Pr^{-1}\nabla^2 \check{\theta}. \tag{2.24}$$

In (2.22)–(2.24) $\hat{V}$, $\hat{W}$ and $\check{u}$ are given by (2.17) and (2.18).

The boundary conditions for $\hat{U}, \hat{\varphi}, \hat{\Theta}, \check{v}, \check{w}$ and $\check{\theta}$ are

$$\hat{U} = \hat{\varphi} = \partial_y \hat{\varphi} = \partial_z \hat{\varphi} = \hat{\Theta} = \check{v} = \check{w} = \partial_y \check{v} = \check{\theta} = 0 \quad \text{at} \quad y = \pm 1, \tag{2.25}$$

$$\hat{U} = \hat{\varphi} = \partial_y \hat{\varphi} = \partial_z \hat{\varphi} = \hat{\Theta} = \check{v} = \check{w} = \partial_z \check{w} = \check{\theta} = 0 \quad \text{at} \quad z = \pm 1. \tag{2.26}$$

2.2 Numerical method

Our method to investigate the linear stability of the flow is exactly the same as the one used by Uhlmann & Nagata (2006). Therefore, only the method for the subsequent nonlinear analysis is presented. We seek a finite amplitude travelling wave solution with the streamwise phase velocity, c, so that the mean parts, $\hat{U}$, $\hat{\varphi}$ and $\hat{\Theta}$, are steady and the residuals, $\check{v}$, $\check{w}$ and $\check{\theta}$, of the disturbances are expanded as follows:

$$\begin{pmatrix} \check{v} \\ \check{w} \\ \check{\theta} \end{pmatrix}(x, y, z, t) = \sum_{\substack{l=-L \\ l \neq 0}}^{L} \begin{pmatrix} v_l(y, z) \\ w_l(y, z) \\ \theta_l(y, z) \end{pmatrix} \exp\left[il\alpha(x - ct)\right]. \tag{2.27}$$

Substitution of (2.18) and (2.27) into (2.19)–(2.21) gives

$$\begin{aligned} &(\partial_z \hat{\varphi} \partial_y - \partial_y \hat{\varphi} \partial_z)\bar{U} - \hat{\Theta} - \triangle_2 \hat{U} \\ &\quad + \sum_{l_1 + l_2 = 0} \frac{i}{l_1 \alpha} \big\{ (\partial_y v_{l_1} + \partial_z w_{l_1}) \partial_y v_{l_2} + (\partial_{yy}^2 v_{l_1} + \partial_{yz}^2 w_{l_1}) v_{l_2} \\ &\qquad\qquad + (\partial_y v_{l_1} + \partial_z w_{l_1}) \partial_z w_{l_2} + (\partial_{yz}^2 v_{l_1} + \partial_{zz}^2 w_{l_1}) w_{l_2} \big\} = 0, \end{aligned} \tag{2.28}$$

$$\begin{aligned} &-(\partial_z \hat{\varphi} \partial_y - \partial_y \hat{\varphi} \partial_z - \triangle_2)\triangle_2 \hat{\varphi} \\ &\quad + \sum_{l_1 + l_2 = 0} \big\{ \partial_{yy}^2 v_{l_1} w_{l_2} + 2\partial_y v_{l_1} \partial_y w_{l_2} + v_{l_1} \partial_{yy}^2 w_{l_2} \\ &\qquad - \partial_{zz}^2 v_{l_1} w_{l_2} - 2\partial_z v_{l_1} \partial_z w_{l_2} - v_{l_1} \partial_{zz}^2 w_{l_2} \\ &\qquad + 2\partial_y w_{l_1} \partial_z w_{l_2} + 2\partial_{yz}^2 w_{l_1} w_{l_2} - 2\partial_y v_{l_1} \partial_z v_{l_2} - 2\partial_{yz}^2 v_{l_1} v_{l_2} \big\} = 0, \end{aligned} \tag{2.29}$$

$$\begin{aligned} &(\partial_z \hat{\varphi} \partial_y - \partial_y \hat{\varphi} \partial_z)\bar{\Theta} - Pr^{-1} \triangle_2 \hat{\Theta} \\ &\qquad + \sum_{l_1 + l_2 = 0} \big\{ \partial_y v_{l_1} \theta_{l_2} + v_{l_1} \partial_y \theta_{l_2} + \partial_z w_{l_1} \theta_{l_2} + w_{l_1} \partial_z \theta_{l_2} \big\} = 0. \end{aligned} \tag{2.30}$$

By substituting (2.18) and (2.27) into (2.22)–(2.24) and operating $\int_0^{2\pi/\alpha} \cdot \exp[-il_0\alpha x]\mathrm{d}x$ ($l_0 = 1, \cdots, L$), we obtain the equations for v_l, w_l and θ_l as shown below:

$$
\begin{aligned}
&\Big[\big\{-c+\bar{U}-\frac{i}{l_0\alpha}(\partial_z\hat{\varphi}\partial_y-\partial_y\hat{\varphi}\partial_z+l_0^2\alpha^2-\triangle_2+\partial_{yz}^2\hat{\varphi})\big\}(-l_0^2\alpha^2+\partial_{yy}^2)\\
&\quad-\partial_{yy}^2\bar{U}+\frac{i}{l_0\alpha}\partial_{yy}^2\hat{\varphi}\partial_{yz}^2\Big]v_{l_0}\\
&+\Big[\big\{-c+\bar{U}-\frac{i}{l_0\alpha}(\partial_z\hat{\varphi}\partial_y-\partial_y\hat{\varphi}\partial_z+l_0^2\alpha^2-\triangle_2+\partial_{yz}^2\hat{\varphi})\big\}\partial_{yz}^2\\
&\quad+\frac{i}{l_0\alpha}\partial_{yy}^2\hat{\varphi}\partial_{zz}^2+\partial_y\bar{U}\partial_z-\partial_z\bar{U}\partial_y-\partial_{yz}^2\bar{U}+il_0\alpha\partial_{zz}^2\hat{\varphi}\Big]w_{l_0}+\partial_y\theta_{l_0}\\
&+\sum_{l_1+l_2=l_0}\big\{il_0(1-\frac{l_1}{l_2})\alpha v_{l_1}\partial_y v_{l_2}+\frac{i}{l_1\alpha}\partial_y v_{l_1}\partial_{yy}^2 v_{l_2}-\frac{i}{l_2\alpha}v_{l_1}\partial_{yyy}^3 v_{l_2}\\
&\quad-\frac{il_0l_1\alpha}{l_2}v_{l_1}\partial_z w_{l_2}+il_0\alpha\partial_z v_{l_1}w_{l_2}+i(\frac{1}{l_1\alpha}+\frac{1}{l_2\alpha})\partial_{yy}^2 v_{l_1}\partial_z w_{l_2}\\
&\quad-\frac{i}{l_1\alpha}\partial_{yz}^2 v_{l_1}\partial_y w_{l_2}+\frac{i}{l_1\alpha}\partial_y v_{l_1}\partial_{yz}^2 w_{l_2}-\frac{i}{l_2\alpha}v_{l_1}\partial_{yyz}^3 w_{l_2}-\frac{i}{l_1\alpha}\partial_{yyz}^3 v_{l_1}w_{l_2}\\
&\quad+i(\frac{1}{l_1\alpha}+\frac{1}{l_2\alpha})\partial_z w_{l_1}\partial_{yz}^2 w_{l_2}-\frac{i}{l_2\alpha}\partial_y w_{l_1}\partial_{zz}^2 w_{l_2}-\frac{i}{l_2\alpha}w_{l_1}\partial_{yzz}^3 w_{l_2}\big\}=0,
\end{aligned}
\tag{2.31}
$$

$$
\begin{aligned}
&\Big[\big\{-c+\bar{U}-\frac{i}{l_0\alpha}(\partial_z\hat{\varphi}\partial_y-\partial_y\hat{\varphi}\partial_z+l_0^2\alpha^2-\triangle_2-\partial_{yz}^2\hat{\varphi})\big\}(-l_0^2\alpha^2+\partial_{zz}^2)\\
&\quad-\partial_{zz}^2\bar{U}-\frac{i}{l_0\alpha}\partial_{zz}^2\hat{\varphi}\partial_{yz}^2\Big]w_{l_0}\\
&+\Big[\big\{-c+\bar{U}-\frac{i}{l_0\alpha}(\partial_z\hat{\varphi}\partial_y-\partial_y\hat{\varphi}\partial_z+l_0^2\alpha^2-\triangle_2-\partial_{yz}^2\hat{\varphi})\big\}\partial_{yz}^2\\
&\quad-\frac{i}{l_0\alpha}\partial_{zz}^2\hat{\varphi}\partial_{yy}^2+\partial_z\bar{U}\partial_y-\partial_y\bar{U}\partial_z-\partial_{yz}^2\bar{U}-il_0\alpha\partial_{yy}^2\hat{\varphi}\Big]v_{l_0}+\partial_z\theta_{l_0}\\
&+\sum_{l_1+l_2=l_0}\big\{il_0(1-\frac{l_1}{l_2})\alpha w_{l_1}\partial_z w_{l_2}+\frac{i}{l_1\alpha}\partial_z w_{l_1}\partial_{zz}^2 w_{l_2}-\frac{i}{l_2\alpha}w_{l_1}\partial_{zzz}^3 w_{l_2}\\
&\quad-\frac{il_0l_2\alpha}{l_1}\partial_y v_{l_1}w_{l_2}+il_0\alpha v_{l_1}\partial_y w_{l_2}+i(\frac{1}{l_1\alpha}+\frac{1}{l_2\alpha})\partial_y v_{l_1}\partial_{zz}^2 w_{l_2}\\
&\quad-\frac{i}{l_2\alpha}\partial_z v_{l_1}\partial_{yz}^2 w_{l_2}+\frac{i}{l_2\alpha}\partial_{yz}^2 v_{l_1}\partial_z w_{l_2}-\frac{i}{l_1\alpha}\partial_{yzz}^3 v_{l_1}w_{l_2}-\frac{i}{l_2\alpha}v_{l_1}\partial_{yzz}^3 w_{l_2}\\
&\quad+i(\frac{1}{l_1\alpha}+\frac{1}{l_2\alpha})\partial_y v_{l_1}\partial_{yz}^2 v_{l_2}-\frac{i}{l_2\alpha}\partial_z v_{l_1}\partial_{yy}^2 v_{l_2}-\frac{i}{l_2\alpha}v_{l_1}\partial_{yyz}^3 v_{l_2}\big\}=0,
\end{aligned}
\tag{2.32}
$$

$$\begin{aligned}&\big[-il_0\alpha c + il_0\alpha\bar{U} + \partial_z\hat{\varphi}\partial_y - \partial_y\hat{\varphi}\partial_z - Pr^{-1}(-l_0^2\alpha^2 + \partial_{yy}^2 + \partial_{zz}^2)\big]\theta_{l_0} \\ &+v_{l_0}\partial_y\bar{\Theta} + w_{l_0}\partial_z\bar{\Theta} + \sum_{l_1+l_2=l_0} -\frac{l_2}{l_1}(\partial_y v_{l_1} + \partial_z w_{l_1})\theta_{l_2} + v_{l_1}\partial_y\theta_{l_2} + w_{l_1}\partial_z\theta_{l_2} = 0.\end{aligned} \tag{2.33}$$

All the variables are expanded onto the basis functions ϕ_m and ψ_n as follows:

$$\begin{pmatrix} v_l \\ w_l \\ \theta_l \\ \hat{U} \\ \hat{\varphi} \\ \hat{\Theta} \end{pmatrix} = \sum_{m=2}^{M}\sum_{n=2}^{N} \begin{pmatrix} v_{lmn}\phi_m(y)\psi_n(z) \\ w_{lmn}\psi_m(y)\phi_n(z) \\ \theta_{lmn}\psi_m(y)\psi_n(z) \\ U_{mn}\psi_m(y)\psi_n(z) \\ \varphi_{mn}\phi_m(y)\phi_n(z) \\ \Theta_{mn}\psi_m(y)\psi_n(z) \end{pmatrix}, \tag{2.34}$$

where ϕ_m and ψ_n are the combination of the Chebyshev polynomials T_j:

$$\begin{cases} \phi_{2m} = T_{2m} + (m^2-1)T_0 - m^2T_2, \\ \phi_{2m+1} = T_{2m+1} + \dfrac{m^2+m-2}{2}T_1 - \dfrac{m^2+m}{2}T_3, \end{cases} \tag{2.35}$$

$$\begin{cases} \psi_{2n} = T_{2n} - T_0, \\ \psi_{2n+1} = T_{2n+1} - T_1. \end{cases} \tag{2.36}$$

Here, ϕ_m satisfies both the Dirichlet and Neumann conditions, whereas ψ_n satisfies the Dirichlet condition. To have a real solution, the amplitude coefficients, v_{lmn}, etc. in (2.34), must satisfy the reality condition, $v_{lmn}^* = v_{-lmn}$, etc. , where * denotes complex conjugate. One of the coefficients is fixed as

$$\Im[v_{252}] = 0 \tag{2.37}$$

in order to lock the phase of the travelling waves.

We discretize the governing equations (2.28)–(2.33) by the Galerkin method: the calculation of

$$\int_{-1}^{+1}\int_{-1}^{+1} \begin{pmatrix} (2.28)\ \psi_p(y)\psi_q(z) \\ (2.29)\ \phi_p(y)\phi_q(z) \\ (2.30)\ \psi_p(y)\psi_q(z) \\ (2.31)\ \phi_p(y)\psi_q(z) \\ (2.32)\ \psi_p(y)\phi_q(z) \\ (2.33)\ \psi_p(y)\psi_q(z) \end{pmatrix} W(y)W(z)\ \mathrm{d}y\mathrm{d}z \tag{2.38}$$

results in the quadratic equation,

$$A_{ij}x_j + B_{ijk}x_jx_k = 0, \;\; x_j = (v_{lmn}, w_{lmn}, \theta_{lmn}, U_{mn}, \varphi_{mn}, \Theta_{mn}, c)^T. \tag{2.39}$$

Here, the weight function $W(y) = 1/\sqrt{1-y^2}$. The properties of the Chebyshev polynomials are summarized in 2.7.1. We solve the algebraic equation (2.39) by the Newton-Raphson iterative method. The iteration is continued until the relative errors of all the components of the vector x_j reduce below 10^{-5}.

Following Wedin *et al.* (2009), we adopt the bulk Reynolds number in order to measure the magnitude of nonlinearity, to be compared to the laminar case where $Re_b = 0.47704Re$:

$$Re_b = \frac{1}{4}\int_{-1}^{+1}\int_{-1}^{+1} \bar{U}(y,z)\,\mathrm{d}y\mathrm{d}z. \tag{2.40}$$

The skin friction λ defined by

$$\lambda = \frac{4\chi}{Re_b^2}, \tag{2.41}$$

and the kinetic energy of the flow for one axial period defined by

$$E = \frac{1}{4}\int_{-1}^{+1}\int_{-1}^{+1} \frac{|\boldsymbol{U}_B + \hat{\boldsymbol{U}}|^2}{2}\mathrm{d}y\mathrm{d}z + \frac{\alpha}{8\pi}\int_0^{2\pi/\alpha}\int_{-1}^{+1}\int_{-1}^{+1} \frac{|\check{\boldsymbol{u}}|^2}{2}\mathrm{d}x\mathrm{d}y\mathrm{d}z. \tag{2.42}$$

also measure the nonlinearity.

2.3 Symmetry

Examination of the governing equations (see (2.28)–(2.33)) reveals the following four symmetry groups for the variables, v_l, w_l and θ_l:

$$\text{symmetry} \quad \mathrm{I} : v_l \begin{cases} (l^{+}; e, e) \\ (l^{++}; o, e) \end{cases}, w_l \begin{cases} (l^{+}; o, o) \\ (l^{++}; e, o) \end{cases}, \theta_l \begin{cases} (l^{+}; o, e) \\ (l^{++}; e, e) \end{cases}, \tag{2.43}$$

$$\text{symmetry} \quad \mathrm{II} : v_l \begin{cases} (l^{+}; e, o) \\ (l^{++}; o, e) \end{cases}, w_l \begin{cases} (l^{+}; o, e) \\ (l^{++}; e, o) \end{cases}, \theta_l \begin{cases} (l^{+}; o, o) \\ (l^{++}; e, e) \end{cases}, \tag{2.44}$$

$$\text{symmetry} \quad \mathrm{III} : v_l \begin{cases} (l^{+}; o, e) \\ (l^{++}; o, e) \end{cases}, w_l \begin{cases} (l^{+}; e, o) \\ (l^{++}; e, o) \end{cases}, \theta_l \begin{cases} (l^{+}; e, e) \\ (l^{++}; e, e) \end{cases}, \tag{2.45}$$

$$\text{symmetry} \quad \mathrm{IV} : v_l \begin{cases} (l^{+}; o, o) \\ (l^{++}; o, e) \end{cases}, w_l \begin{cases} (l^{+}; e, e) \\ (l^{++}; e, o) \end{cases}, \theta_l \begin{cases} (l^{+}; e, o) \\ (l^{++}; e, e) \end{cases}. \tag{2.46}$$

Here, l^{+} and l^{++} denote odd and even integers, respectively, for l in (2.27). The notation, e or o, implies that the variable is an even or odd function with

respect to the y- and z-coordinates. Any of the symmetry groups carries the following symmetry for the mean parts of the disturbance:

$$\hat{U}(e,e), \hat{\varphi}(o,o), \hat{\Theta}(e,e). \tag{2.47}$$

These symmetries are the extension of the four symmetry groups admitted by the linear stability analysis considered by Uhlmann & Nagata (2006). We focus on the symmetry I because it is satisfied by one of the modes which renders the flow unstable according to Uhlmann & Nagata (2006). Note that the symmetries I and IV are equivalent as there is no distinction between y and z in a square duct.

It is easily verified that the symmetry I is composed of the shift-and-reflect symmetry **S** and the mirror symmetry **Z** about the y-axis used by Wedin *et al.* (2009):

$$\mathbf{S}: \begin{pmatrix} u \\ v \\ w \\ T \end{pmatrix} (\xi, y, z) \rightarrow \begin{pmatrix} u \\ -v \\ w \\ T \end{pmatrix} (\xi + \frac{\pi}{\alpha}, -y, z), \tag{2.48}$$

$$\mathbf{Z}: \begin{pmatrix} u \\ v \\ w \\ T \end{pmatrix} (\xi, y, z) \rightarrow \begin{pmatrix} u \\ v \\ -w \\ T \end{pmatrix} (\xi, y, -z), \tag{2.49}$$

where $\xi = x - ct$. The symmetry of the flow in the cross section is schematically represented in figure 2.4.

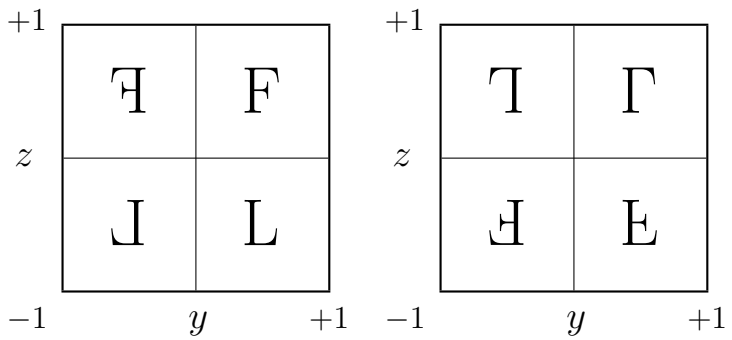

Figure 2.4: The schematic flow pattern with the symmetry I in the cross section at (left) $\xi = \xi_0$ and (right) $\xi = \xi_0 + \pi/\alpha$, where ξ_0 is an arbitrary constant. The letters "F" and "L" show some different flow patterns in the cross section.

2.4 Continuation to the isothermal solution

The linear stability analysis shows that the laminar flow becomes unstable to a perturbation with the streamwise wavenumber $\alpha = 1.0$ inside the dashed curve in the Re–Gr plane (see figure 2.5). This region overlaps the region M_2 for the laminar flow. In order to establish the continuation of a nonlinear solution in

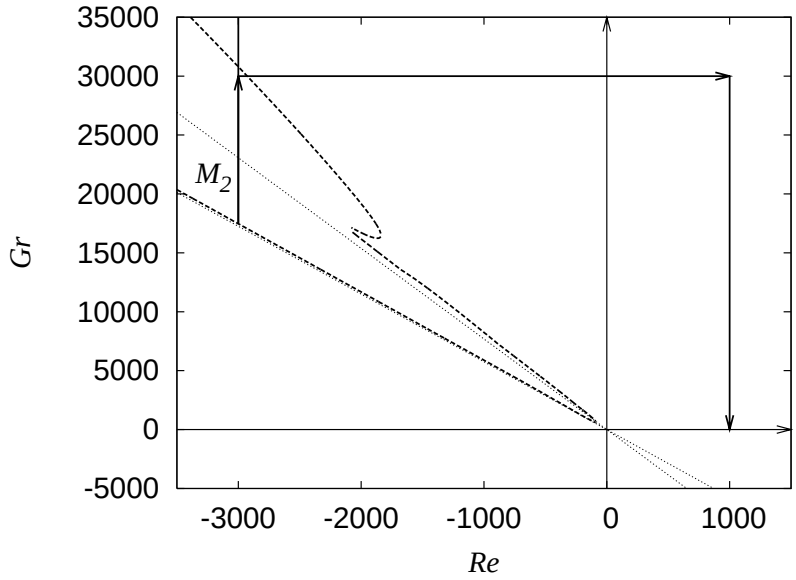

Figure 2.5: The path taken from the linear critical point of the internally heated duct flow to the isothermal solution indicated by the arrows. The dashed curve represents the neutral curve with $\alpha = 1.0$. The region M_2 is bounded by the two thin lines, $Gr/Re = -7.69$ and -5.75.

the Re–Gr plane we first obtain a nonlinear solution with $\alpha = 1.0$ bifurcating from the neutral curve. Our goal is to bring the solution to the isothermal case ($Gr = 0$); one successful continuation path was accomplished by following the arrows, as shown in figure 2.5. This path is composed of three sections: (a) varying Gr from 17470 to 30000 by fixing $Re = -3000$, (b) increasing Re from -3000 to 1000 by fixing $Gr = 30000$ and (c) decreasing Gr from 30000 down to zero by fixing $Re = 1000$. The amplitude of the solution at each section varies. Accordingly Re_b changes along the path. We plot Re_b at each section in figure 2.6. In the section (a) the path, which starts from the point (black triangle) on the laminar state (dotted curve), experiences several turning points before it reaches the point $(Gr, Re_b) = (30000, 4.11)$ (open triangle in figure 2.6a). The path in the section (b) continues from the point (open triangle) at $(Gr, Re_b) = (30000, 4.11)$ in the section (a). Along the path Re_b increases

monotonically as Re is increased and the path ends at $(Re, Re_b) = (1000, 1481)$ (open circle in figure 2.6b). As shown in figure 2.6(c), reducing the Grashof number from 30,000 brings the solution to the isothermal case $Gr = 0$ (closed circle on the branch indicated by 'lower' in the figure). The solution exists even when the Grashof number is decreased further down to -2369, where the path experiences a turning point. After going around the turning point the path crosses the line, $Gr = 0$, again (another closed circle on the branch indicated by 'upper' in the figure) as Gr is increased. We refer to the solution branch closer to the laminar state as the lower branch solution and the solution further away as the upper branch solution as shown in figure 2.6(c).

2.5 Mirror-symmetric travelling wave

The two isothermal solutions (closed circles in figure 2.6c) are continued in the Re-axis. The nature of the saddle-node bifurcation of these new travelling wave solution is shown in terms of the phase velocity c in figure 2.7. The accuracy of the solution close to the saddle-node point with respect to the truncation level is listed in table 2.1. The solution is seen to converge well at $(L, M, N) = (6, 33, 33)$, which we adopt in the following analysis unless stated otherwise. Also shown in figure 2.7 is the bifurcation of the travelling wave solution, referred to as WBN hereafter, obtained by the SSP approach of Wedin *et al.* (2009). The particular wavenumbers indicated in the figure, $\alpha = 1.14$ and 0.85, correspond to those which give their lowest bulk Reynolds numbers for the present solution and WBN, respectively. These wavenumbers are determined by tracing the existence domain of the solutions in (α, Re_b)-space. The domain shrinks as Re is decreased (see figure 2.8) and we pinpoint the wavenumbers at the saddle-node with the accuracy of the wavenumber increment $\Delta\alpha = 0.01$. The domain of our new travelling wave solution disappears at $Re = 827.5$.

Table 2.1: The phase velocity c, the bulk Reynolds number Re_b and the skin friction λ of the upper branch solution with $\alpha = 1.14$ at $Re = 836$ as a function of the truncation level (L, M, N).

(L, M, N)	c	Re_b	λ
(4, 29, 29)	451.34	331.86	0.10304
(6, 33, 33)	450.54	331.57	0.10322
(8, 37, 37)	450.62	331.60	0.10320
(10, 41, 41)	450.60	331.59	0.10320

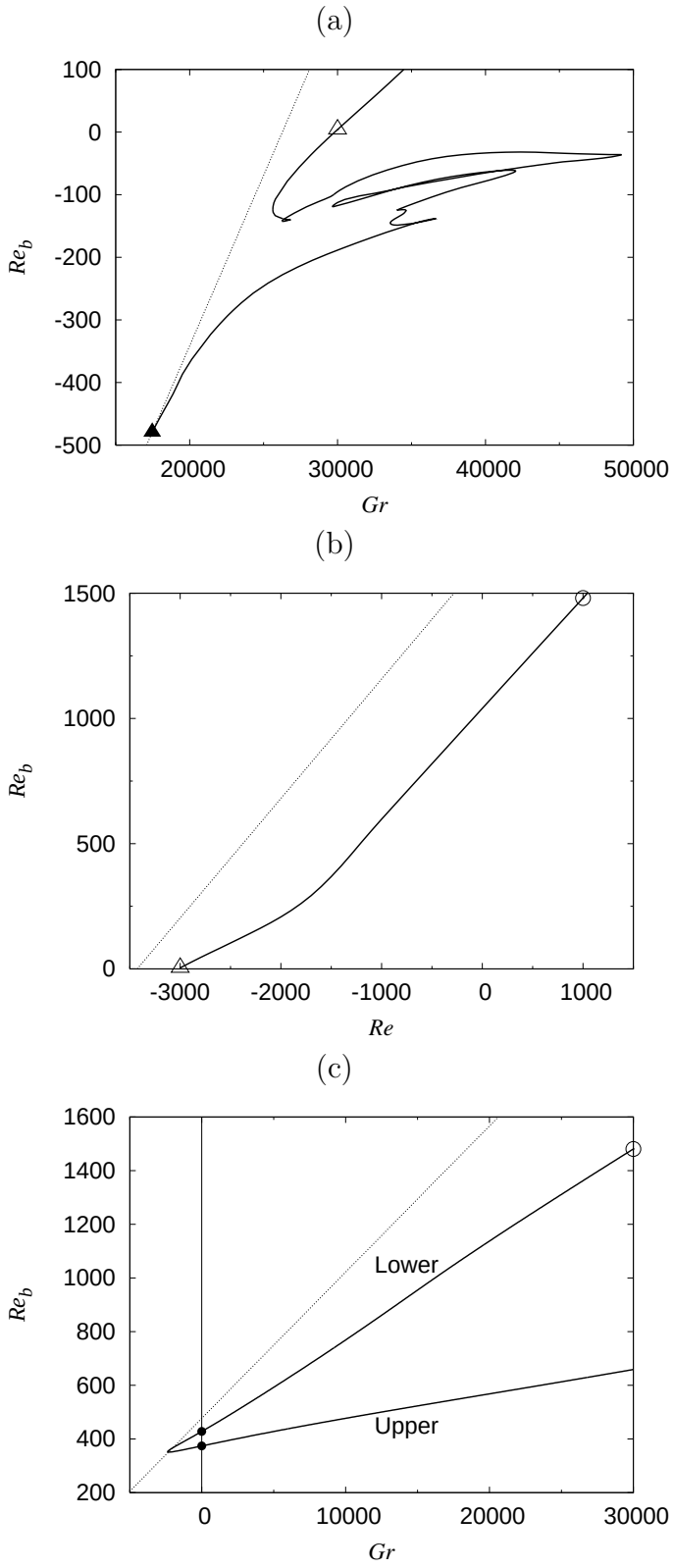

Figure 2.6: The variation of Re_b along the path in figure 2.5. (a) $Re = -3000$, (b) $Gr = 30000$, (c) $Re = 1000$. Two closed circles correspond to the isothermal solutions. The dotted line shows the laminar state, $Re_b = 0.47704Re + 0.054480Gr$.

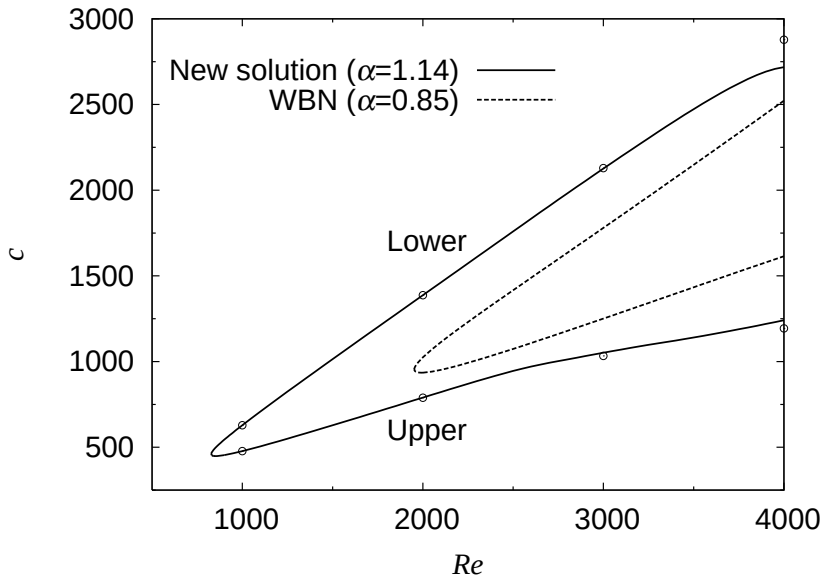

Figure 2.7: The phase velocity c. Solid curve: the new solution, dotted curve: WBN. The truncation level $(L, M, N) = (6, 33, 33)$ is used to draw the curve, whereas isolated points with $(L, M, N) = (10, 41, 41)$ are plotted with open circles.

The kinetic energy E of the flow for one axial period is plotted against Re in figure 2.9(a), highlighting the proximity of the lower branch state to the laminar solution. A similar effect can be ascertained by inspection of figure 2.9(b), which shows the bulk Reynolds number versus the Reynolds number. The mean velocity distribution of the upper branch solution is more deformed by the nonlinear interaction between the disturbances than that of the lower branch. It is also clear that the lower branch of WBN is further away from the laminar state at all values of Re.

Figure 2.10 shows the skin friction λ against the bulk Reynolds number. In addition to the result of our solution, WBN, the laminar solution and the experimental data of the fully developed turbulence, which obeys $\lambda = 28.45/Re_b$ and $\lambda^{-1/2} = 2\log_{10}(2.25Re_b\lambda^{1/2}) - 0.8$ (Jones 1976), respectively, are also plotted. The upper and lower branches of our solution approach the curves given by the experimental data and the laminar flow, respectively, as Re_b is increased. Our solution takes its minimum bulk Reynolds number, 332, at $\alpha = 1.14$, which is substantially smaller than that of WBN ($\min Re_b = 598$ at $\alpha = 0.85$).

The iso-surfaces of the streamwise vorticity and the streamwise velocity of the upper branch solution with $\alpha = 1.0$ at $Re = 1500$ are shown in figure 2.11. Notice the low-speed streak manifested as a wrinkle on the iso-surface of the

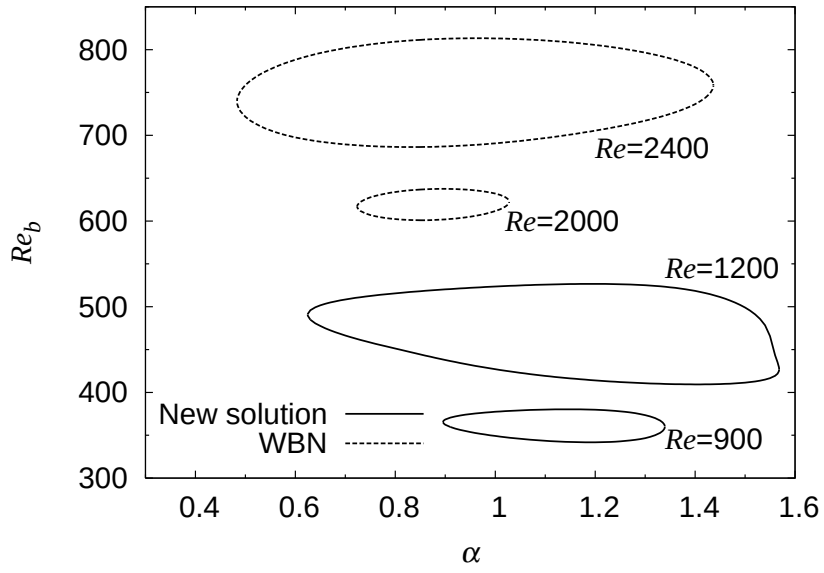

Figure 2.8: The domains of existence of the new travelling wave solutions (solid curves) and those by WBN (dotted curves).

streamwise velocity in the bottom figure near the wall at $z = -1$. As can be seen the low-speed streak is flanked by staggered quasi-streamwise vortices near the walls at $z = \pm 1$. This structure is often identified as the coherent structure of the near-wall turbulence. The top-left frames of figures 2.12 and 2.13 show the mean flow field, $(U_B + \hat{U}, \hat{V}, \hat{W})$. Both the lower and upper branches display outflow from the wall towards the centre of the duct along $y = 0$. We can also notice three stagnation points in terms of the velocity field $(\hat{V}, \hat{W})$ on $y = 0$: one at the origin of the axes and the other two approximately half way between the origin and the side walls $z = \pm 1$. Also noticeable is the eight-vortex structure (four dominant vortices and four minor vortices): one dominant and one minor vortex in each quadrant. This structure is different from the eight-vortex structure with diagonal symmetry observed in the fully developed turbulence at higher Re (Gavrilakis 1992; Uhlmann *et al.* 2007). The instantaneous total flow fields are displayed also in figures 2.12 and 2.13. The dominant vortices near the walls $z = \pm 1$ oscillate in the y-direction as they propagate in the x-direction (see also figure 2.11). The minor vortices observed in the mean flow field are not captured at the vorticity level plotted in figure 2.11. While the oscillatory motion of the lower branch solution is gentle, that of the upper branch solution is more active with a vortex oscillating along each of the walls at $z = \pm 1$. According to the DNS result by Uhlmann *et al.* (2007),

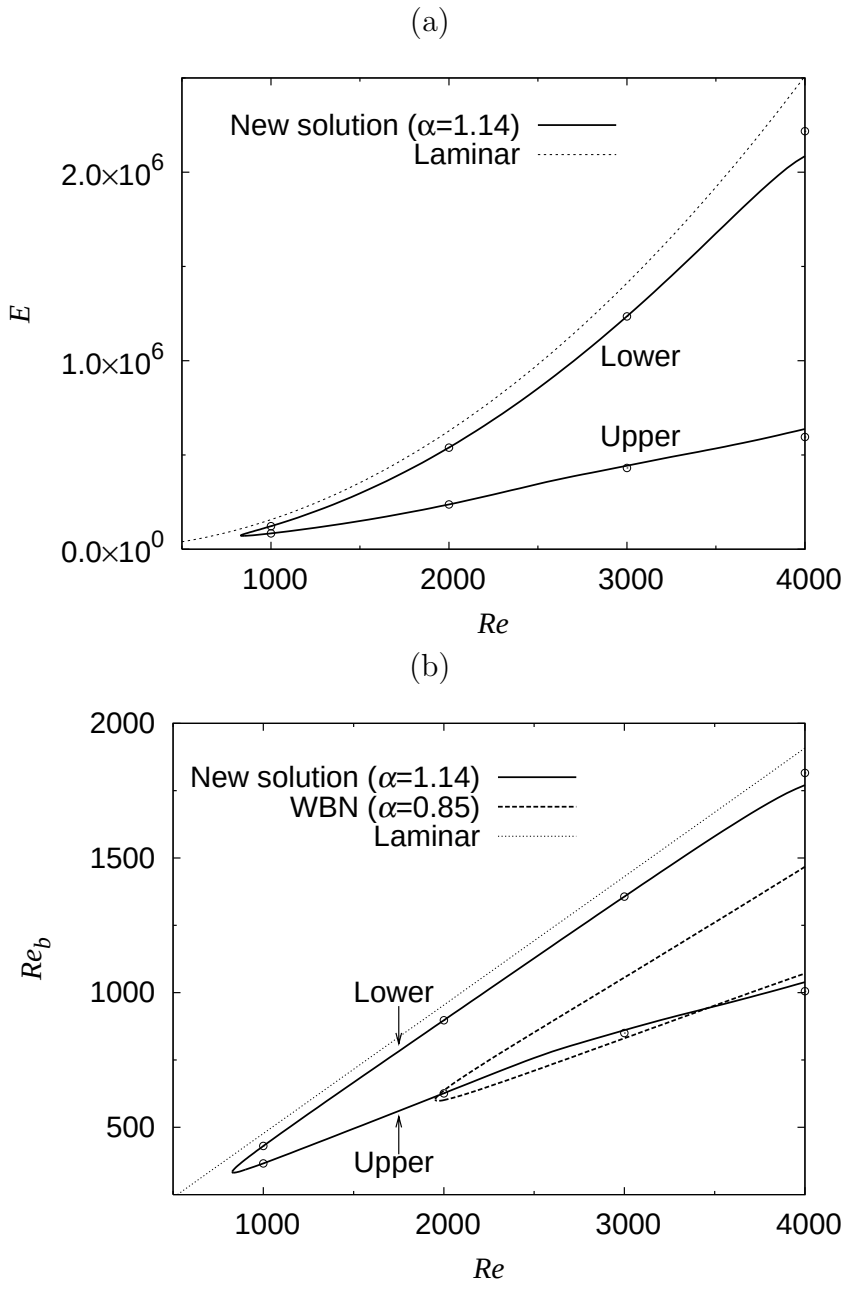

Figure 2.9: (a) Kinetic energy E of the new solution versus Re (solid curve). The dotted curve indicates the energy for the laminar flow given by $1/4 \int_{-1}^{1} \int_{-1}^{1} {U_B}^2/2 \ \mathrm{d}y\mathrm{d}z = 0.1568Re^2$. (b) Bulk Reynolds number versus Re. The truncation level $(L, M, N) = (6, 33, 33)$ is used to draw the curves, and the circles represent isolated solutions with higher truncation, $(L, M, N) = (10, 41, 41)$.

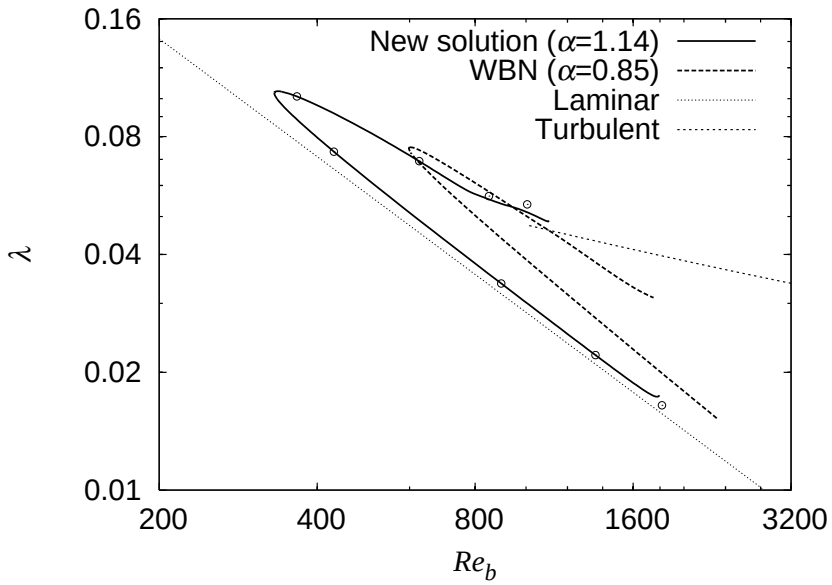

Figure 2.10: The skin friction against the bulk Reynolds number. The current solution: solid curve and WBN: dashed curve. $(L, M, N) = (6, 33, 33)$ except for the open circles of the current solution for which $(L, M, N) = (10, 41, 41)$. The laminar flow: dotted line. The experimental data by Jones (1976): thin dashed curve.

the marginally turbulent flow ($Re_b \sim 1100$) has a four-vortex structure: two near one of the walls and two more near the wall opposite to it (see figure 2.15). A similar four-vortex structure has been reported in the DNS by Wedin *et al.* (2008) (see their figure 12). The four-vortex patterns of Uhlmann *et al.* (2007) have two different orientations, vortices located near $z = \pm 1$ and $y = \pm 1$, that alternate (see figure 2.15a, b). Biau *et al.* (2008) also observed similar alternating patterns with two pairs of vortices near opposing walls before the flow eventually relaminarises (see their figure 4). In our system, in addition to the solution with four dominant vortices near $z = \pm 1$ displayed in figures 2.12 and 2.13, the flow with four vortices near $y = \pm 1$ is also a solution by symmetry.

Figure 2.14 shows the disturbance velocity field of the lower branch solution. Both the mean part $\hat{U}$, $\hat{V}$ and $\hat{W}$ (left figure) and the instantaneous state of the disturbance $\hat{u}$, $\hat{v}$ and $\hat{w}$ surprisingly resemble those of the mirror-symmetric solution M1 in pipe flow found by Pringle & Kerswell (2007) (see figure 2.16). The travelling wave M1 with the axial wavenumber α possesses the shift-and-reflect symmetry, $\mathbf{S}$: $(u, v, w)(s, \phi, z) \to (u, -v, w)(s, -\phi, z + \pi/\alpha)$, where (u, v, w) is the velocity components in the cylindrical coordinates (s, ϕ, z), and the shift-

and-rotate symmetry, $\mathbf{\Omega}_m$: $(u, v, w)(s, \phi, z) \rightarrow (u, v, w)(s, \phi + \pi/m, z + \pi/\alpha)$ with $m = 1$ (Pringle *et al.* 2009). Coupled with the symmetry $\mathbf{S}$, the symmetry $\mathbf{\Omega}_1$ implies the mirror symmetry, i.e. invariance under reflection in the line $\phi = \pm\pi/2$. For square duct flow the combined symmetry $\mathbf{S}(\mathbf{Z})$, where $\mathbf{S}$ and $\mathbf{Z}$ are given in (2.49), implies the shift-and-rotate symmetry by the angle π since $\mathbf{S}(\mathbf{Z})$: $(u, v, w)(\xi, y, z) \rightarrow \mathbf{S} : (u, v, -w)(\xi, y, -z) \rightarrow (u, -v, -w)$ $(\xi + \pi/\alpha, -y, -z)$. Therefore, the solution in square duct and M1 in pipe flow belong to the same symmetry group. Furthermore, the minimum bulk Reynolds number of our solution, 332 (defined by using the half width of the side as the length scale), is comparable to their 773 (defined by using the diameter of the pipe as the length scale).

2.6 Conclusion

The linear stability analysis of internally heated rectangular duct flow by Uhlmann & Nagata (2006) has been extended to the nonlinear case with the special focus on seeking a nonlinear solution in an isothermal case. We have presented a path to achieve this goal in the *Re*–*Gr* plane, starting from the travelling wave solution bifurcating from the linear critical point of the internally heated flow. The examination of the flow structures and the statistics such as the skin friction obtained so far experimentally (Jones 1976) and numerically (Gavrilakis 1992; Wedin *et al.* 2009; Uhlmann *et al.* 2010) has revealed that our isothermal travelling wave solution is a new solution. The present disturbance velocity fields exhibit a reflective symmetry about the (mirror) plane $z = 0$. This symmetry also holds for the SSP solution by Wedin *et al.* (2009). However, in contrast to the one low-speed streak located near the duct centre in Wedin *et al.* (2009) (see figure 4.7a), the present solution has two low-speed streaks, one near the wall at $z = 1$ and the other at $z = -1$ (see figure 2.11). Uhlmann *et al.* (2010) use the symmetry II, and therefore their flow structure with four low-speed streaks, each on the side of the duct cross section (see figure 4.10a), is clearly different from ours which uses the symmetry I. The minimum bulk Reynolds number for the existence of our solution is found to be 332, which is substantially lower than that of the solution found by Wedin *et al.* (2009). The skin frictions of our upper and lower solution branch approach the curves given by the experimental data and the laminar flow, respectively, as Re_b is increased. Comparison with the DNS results of Biau *et al.* (2008) for the flow which lives near the boundary between the laminar and turbulent states seems to suggest that the new solution is embedded in the edge state of

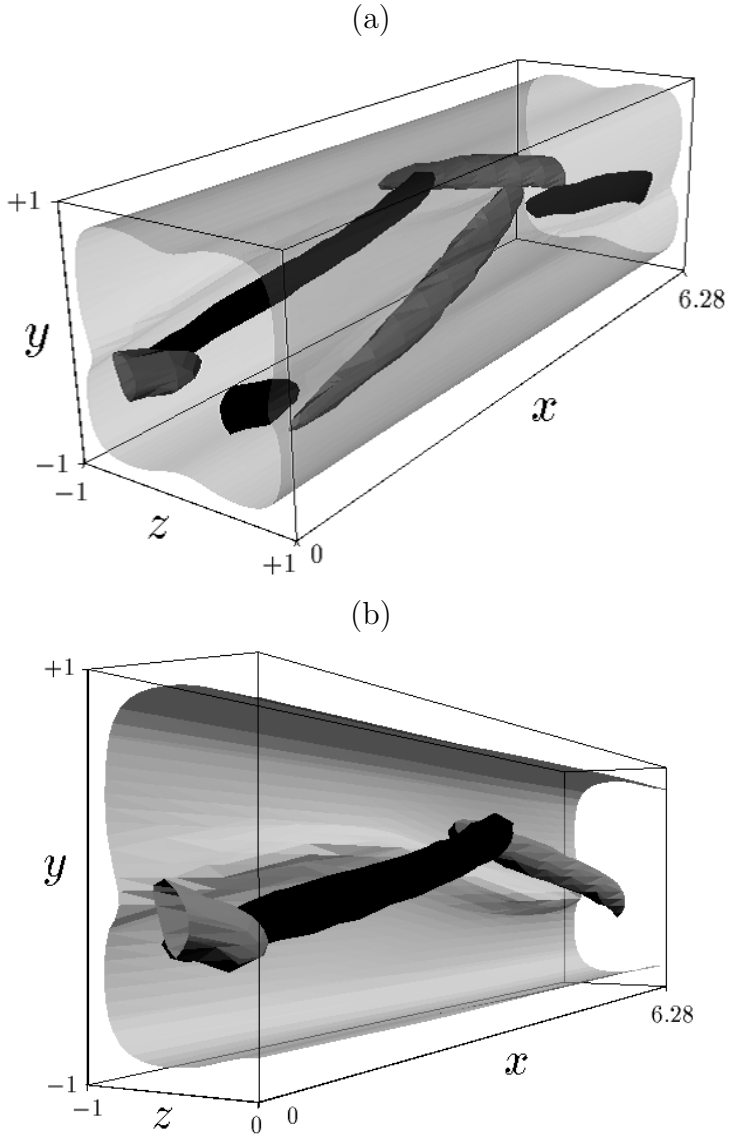

Figure 2.11: The iso-surfaces of the streamwise vorticity and the streamwise velocity of the upper branch solution with $\alpha = 1.0$ at $Re = 1500$ ($Re_b = 506$). Black (dark grey) represents +70% (-70%) of the maximum vorticity and light grey represents 40% of the maximum velocity. (a) The full flow domain and (b) the close-up of $z < 0$. The flow is from left to right.

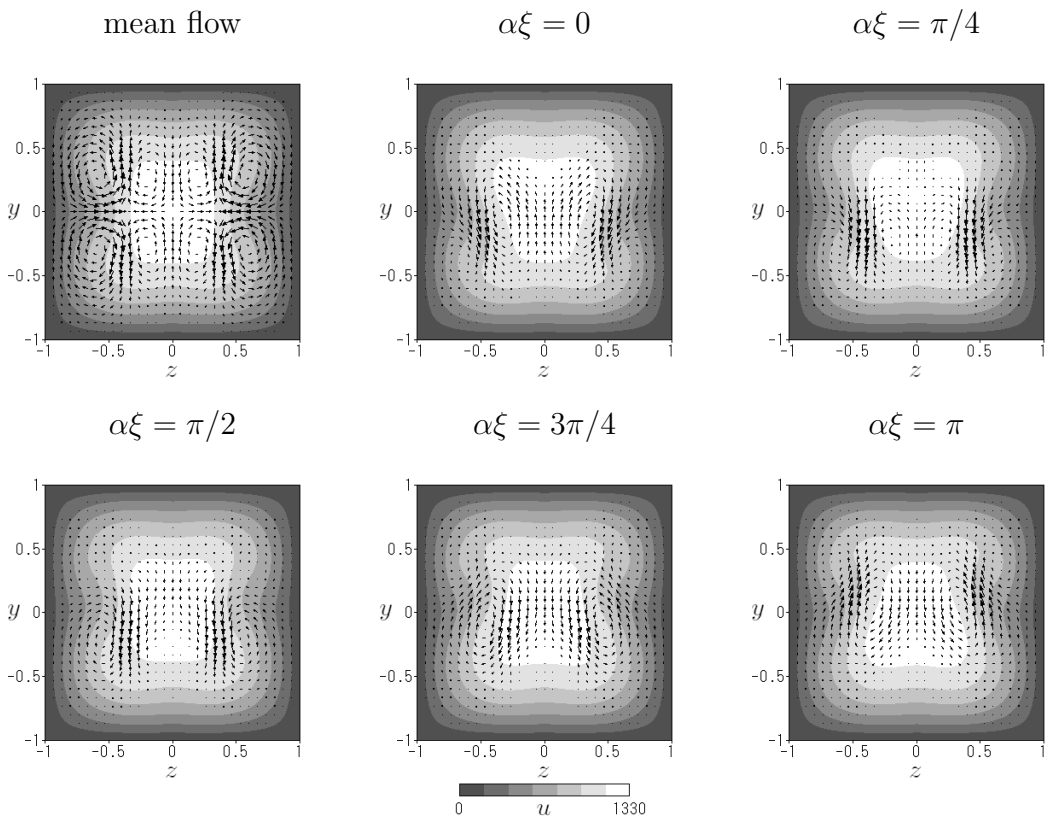

Figure 2.12: Mean flow $\bar{\boldsymbol{U}}$ (top-left) and images of the total flows $\boldsymbol{u}$ along ξ of the lower branch solution with $\alpha = 1.0$ at $Re = 1500$ ($Re_b = 664$). The velocity components are shown on the y-z plane (arrows) and along the x-direction (grey scale). $\xi = x - ct$.

the system (for more details about the edge state, see 3.2.1). The new solution is path independent. However, we could not exclude the possibility of yet other solutions that may exist at the Reynolds number lower than this new solution. Seeking a nonlinear solution which can exist at a smaller Reynolds number is meaningful as it might approach the critical Reynolds number for the globally stability of the flow, below which any disturbance eventually decays.

The flow states presented here is the counterpart of the mirror-symmetric solution in pipe flow obtained by Pringle & Kerswell (2007), although the geometries are very different: the rotational symmetry with an arbitrary angle for pipe flow allows for generalisation of solutions into larger families than the rotational symmetry with only 90 degrees for square duct flow. We expect that the mirror-symmetric solution in pipe flow found by Pringle & Kerswell (2007) will be reproduced by applying the same approach as shown in this chapter to internally heated pipe flow.

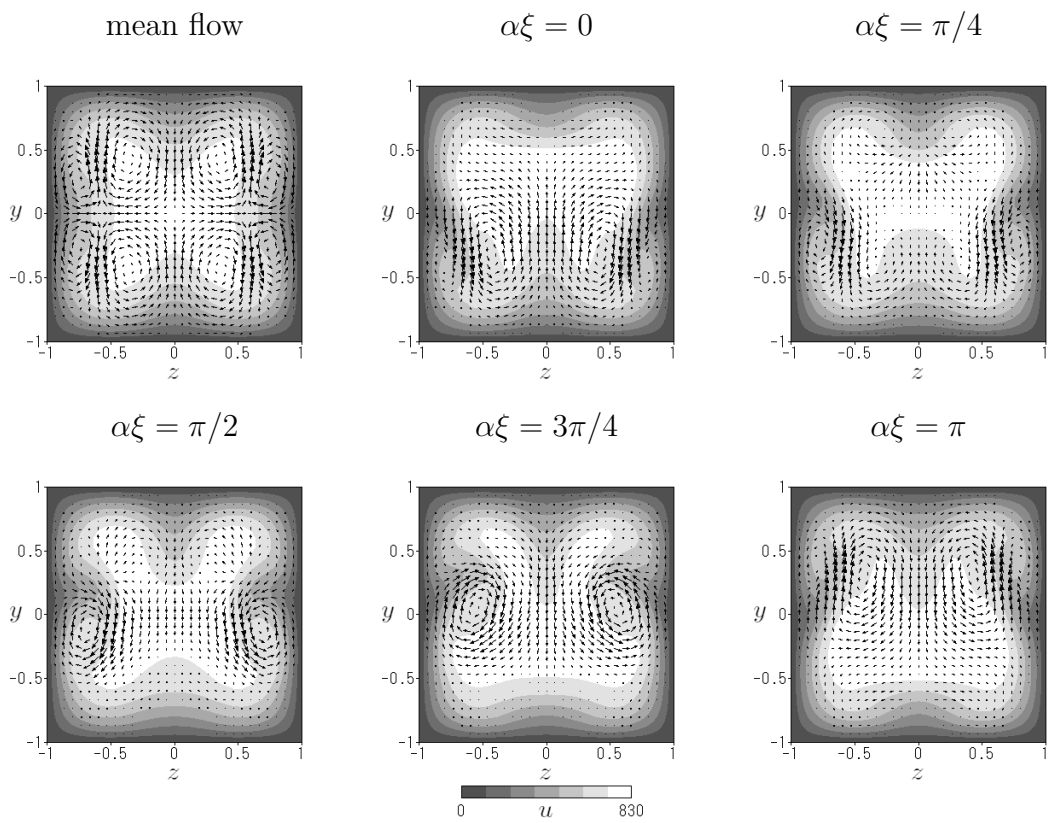

Figure 2.13: Same as figure 2.12 for the upper branch solution. Here, $Re_b = 506$.

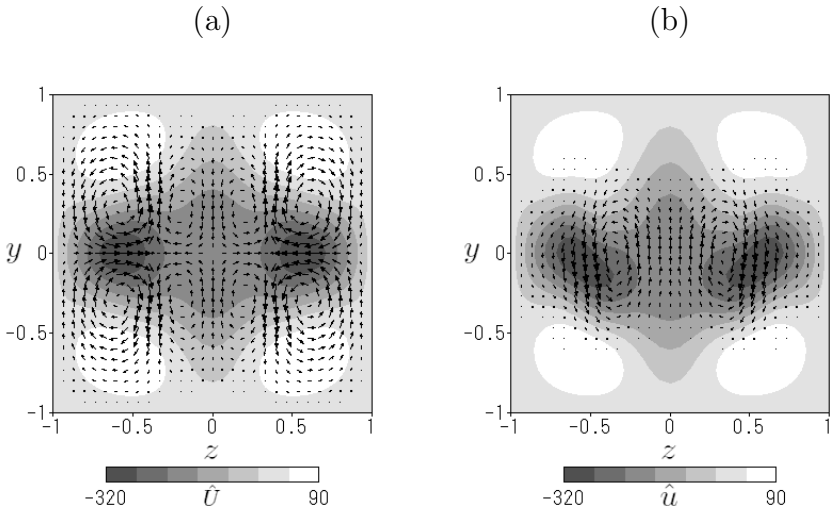

Figure 2.14: The disturbance velocity of the lower branch solution with $\alpha = 1.0$ at $Re = 1500$ ($Re_b = 664$). (a) The mean part $\hat{\boldsymbol{U}}$, (b) the disturbance $\hat{\boldsymbol{u}}$ at $\alpha\xi = 0$. For the meanings of arrows and grey scale see the legend of figure 2.12.

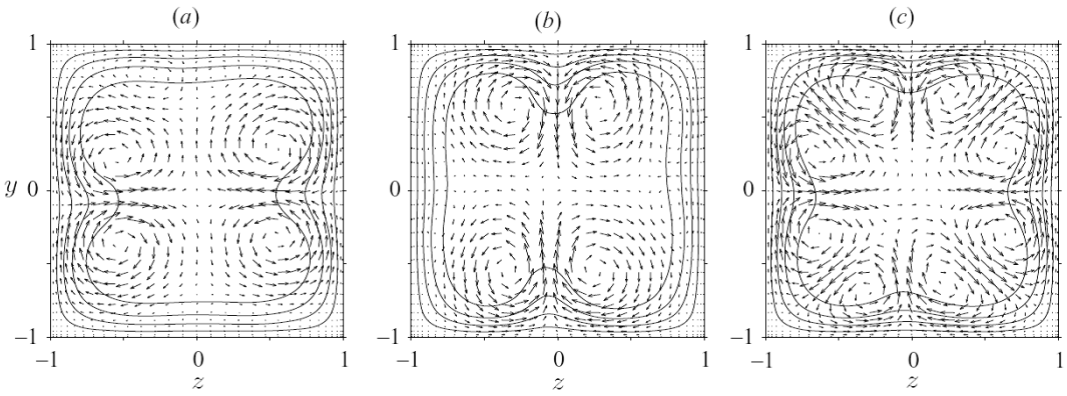

Figure 2.15: Figure 3 of Uhlmann *et al.* (2007). The contours of the streamwise mean flow and the vectors of the secondary mean flow for $Re_b = 1205$ and $\alpha = 1.0$. (a) The average over the time interval with length $771h/u_b$. (b) The average over the different time interval with length $482h/u_b$. (c) The long time integration including both previous intervals. Here, h and u_b are the dimensional quantities, and indicate the half width of the duct and the bulk velocity.

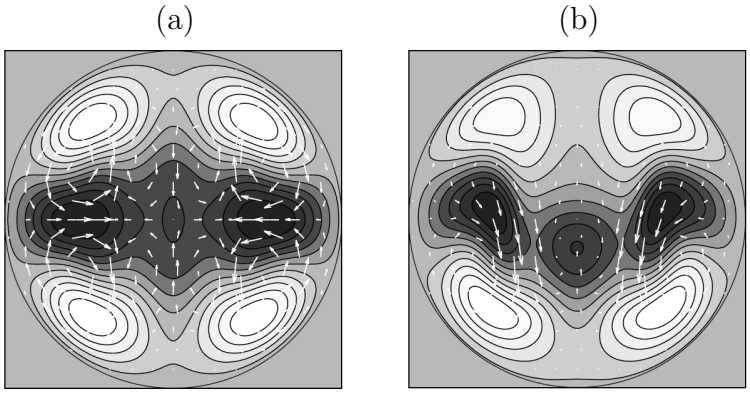

Figure 2.16: The bottom frames of figure 1 of Pringle & Kerswell (2007). Velocity fields of the disturbance for the mirror-symmetric travelling wave in a pipe. (a) The mean part. (b) The instantaneous field.

2.7 Appendix

2.7.1 Properties of the Chebyshev polynomials

The Chebyshev polynomials T_m are defined by

$$T_m(y) = \cos(m \cos^{-1} y). \tag{2.50}$$

Applying the orthogonality of the Chebyshev polynomials, we discretize the governing equations in this study. Here, we summarize the frequently-used properties of the Chebyshev polynomials.

The derivatives of the Chebyshev polynomials are given as follows:

$$T'_m = 2m \sum_{\substack{k=0 \\ m+k:\ \text{odd}}}^{m-1} \frac{T_k}{c_k}, \tag{2.51}$$

$$T''_m = m \sum_{\substack{k=0 \\ m+k:\ \text{even}}}^{m-2} (m^2 - k^2)\frac{T_k}{c_k}, \tag{2.52}$$

$$T'''_m = \frac{1}{4}m \sum_{\substack{k=0 \\ m+k:\ \text{odd}}}^{m-3} (m+k+1)(m+k-1)(m-k+1)(m-k-1)\frac{T_k}{c_k}, \tag{2.53}$$

$$T^{(4)}_m = \frac{1}{24}m \sum_{\substack{k=0 \\ m+k:\ \text{even}}}^{m-4} (m+k)(m-k)(m+k+2)(m+k-2)(m-k+2)(m-k-2)\frac{T_k}{c_k}, \tag{2.54}$$

where the coefficient c_k is defined as

$$c_k = \begin{cases} 2 & (\text{if } k = 0), \\ 1 & (\text{if } k \neq 0). \end{cases} \tag{2.55}$$

The Chebyshev polynomials has the orthogonality:

$$\int_{-1}^{+1} \frac{T_m(y)T_p(y)}{\sqrt{1-y^2}} \mathrm{d}y = \frac{c_p \pi}{2}\delta_{mp}, \tag{2.56}$$

where δ_{mp} is the Kronecker delta. The combinations of (2.51)–(2.54) and (2.56) lead to

$$\int_{-1}^{+1} \frac{T'_m(y)T_p(y)}{\sqrt{1-y^2}} \mathrm{d}y = \begin{cases} m\pi & (\text{if } m+p\text{: odd, and } p \leq m-1), \\ 0 & (\text{else}), \end{cases} \tag{2.57}$$

$$\int_{-1}^{+1} \frac{T_m''(y)T_p(y)}{\sqrt{1-y^2}}\mathrm{d}y = \begin{cases} \dfrac{1}{2}m(m^2-p^2)\pi & \text{(if } m+p\text{: even, and } p \le m-2\text{)}, \\ 0 & \text{(else)}, \end{cases} \tag{2.58}$$

$$\int_{-1}^{+1} \frac{T_m'''(y)T_p(y)}{\sqrt{1-y^2}}\mathrm{d}y = \begin{cases} \dfrac{1}{8}m(m+p+1)(m+p-1)(m-p+1)(m-p-1)\pi \\ \qquad \text{(if } m+p\text{: odd, and } p \le m-3\text{)}, \\ 0 \qquad \text{(else)}, \end{cases} \tag{2.59}$$

$$\begin{aligned} &\int_{-1}^{+1} \frac{T_m^{(4)}(y)T_p(y)}{\sqrt{1-y^2}}\mathrm{d}y \\ &= \begin{cases} \dfrac{1}{48}m(m+p)(m-p)(m+p+2)(m+p-2)(m-p+2)(m-p-2)\pi \\ \qquad \text{(if } m+p\text{: even, and } p \le m-4\text{)}, \\ 0 \qquad \text{(else)}. \end{cases} \end{aligned} \tag{2.60}$$

Also, the following relation is necessary to calculate the nonlinear term:

$$T_{m_1}T_{m_2} = \frac{1}{2}(T_{m_1+m_2} + T_{|m_1-m_2|}). \tag{2.61}$$

2.7.2 Convergence criterion of the nonlinear solution

As mentioned in section 2.2, we end the Newton iteration when the relative errors of all of the coefficients become below 10^{-5}:

$$\frac{|x_j^{(n+1)} - x_j^{(n)}|}{|x_j^{(n)}|} < 10^{-5} \quad \text{for all } j \tag{2.62}$$

where the superscript indicates the number of the iterations. It is shown that the tolerance level 10^{-5} is sufficient to guarantee the numerical convergence. The following examples shows the variations of the values (table 2.2) and the relative errors (figure 2.17) for the phase velocity c and some typical coefficients of the our isothermal solution at $Re = 2000$, $\alpha = 1.14$ with the truncation level $(L, M, N) = (6, 33, 33)$ as a function of the number of the iterations. The dimension of the system is 6242.

The solution is judged to be converged after the 6th iteration and the values of the elements in x_j at the time are underlined in table 2.2. At least 5 digits agree even for higher harmonics, such as $\Re[v_{6,31,16}]$ and $\Re[v_{6,33,32}]$. As shown in figure 2.17(a), (b), the relative errors for the phase velocity, c, and the example of the lower harmonic, $\Re[v_{1,4,2}]$, fluctuate around 10^{-11} or 10^{-12} after the 5th iteration. On the other hand, those of higher harmonics fluctuate around 10^{-6} or 10^{-8} (see figure 2.17c, d). In both cases, the convergence does not improve

afterwards. Therefore, the tolerance level 10^{-5} is a reasonable choice (if a tougher tolerance level is taken, the Newton iteration will be stuck).

Table 2.2: The values of the phase velocity c, $\Re[v_{1,4,2}]$, $\Re[v_{6,31,16}]$ and $\Re[v_{6,33,32}]$ against the number of the iterations.

Iteration	c	$\Re[v_{1,4,2}]$	$\Re[v_{6,31,16}]$	$\Re[v_{6,33,32}]$
0	757.20234	-2.8576215	3.7470195 $\times 10^{-4}$	3.1340373 $\times 10^{-5}$
1	796.51369	-2.5935051	1.2756321 $\times 10^{-3}$	2.8374936 $\times 10^{-5}$
2	789.97788	-2.5862998	1.9004427 $\times 10^{-4}$	4.4116145 $\times 10^{-5}$
3	789.78438	-2.5914831	-5.1934472 $\times 10^{-7}$	3.5835975 $\times 10^{-5}$
4	789.78578	-2.5914993	-7.7468959 $\times 10^{-7}$	3.5804028 $\times 10^{-5}$
5	789.78578	-2.5914994	-7.7467745 $\times 10^{-7}$	3.5804028 $\times 10^{-5}$
6	789.78578	-2.5914994	-7.7468113 $\times 10^{-7}$	3.5804028 $\times 10^{-5}$
7	789.78578	-2.5914994	-7.7468107 $\times 10^{-7}$	3.5804027 $\times 10^{-5}$
8	789.78578	-2.5914994	-7.7468271 $\times 10^{-7}$	3.5804029 $\times 10^{-5}$
9	789.78578	-2.5914994	-7.7468080 $\times 10^{-7}$	3.5804028 $\times 10^{-5}$
10	789.78578	-2.5914994	-7.7467625 $\times 10^{-7}$	3.5804028 $\times 10^{-5}$
11	789.78578	-2.5914994	-7.7468208 $\times 10^{-7}$	3.5804029 $\times 10^{-5}$
12	789.78578	-2.5914994	-7.7468409 $\times 10^{-7}$	3.5804029 $\times 10^{-5}$
13	789.78578	-2.5914994	-7.7467868 $\times 10^{-7}$	3.5804028 $\times 10^{-5}$
14	789.78578	-2.5914994	-7.7467896 $\times 10^{-7}$	3.5804028 $\times 10^{-5}$
15	789.78578	-2.5914994	-7.7468232 $\times 10^{-7}$	3.5804028 $\times 10^{-5}$
16	789.78578	-2.5914994	-7.7467987 $\times 10^{-7}$	3.5804027 $\times 10^{-5}$
17	789.78578	-2.5914994	-7.7468181 $\times 10^{-7}$	3.5804028 $\times 10^{-5}$
18	789.78578	-2.5914994	-7.7467868 $\times 10^{-7}$	3.5804028 $\times 10^{-5}$
19	789.78578	-2.5914994	-7.7468065 $\times 10^{-7}$	3.5804027 $\times 10^{-5}$
20	789.78578	-2.5914994	-7.7468089 $\times 10^{-7}$	3.5804028 $\times 10^{-5}$

2.7.3 Continuation to the isothermal case when $Pr = 0$

We consider the limit of vanishing Prandtl number, $Pr \to 0$. In this case, the governing equation for the temperature disturbance (2.14) becomes $\nabla^2\hat{\theta} = 0$. The isothermal condition on the wall (2.15) leads to $\hat{\theta} \equiv 0$ everywhere. Therefore, the temperature deviation equation is neglected and the problem becomes purely hydrodynamic. The degrees of freedom is reduced by approximately 1/3 from the thermal case.

The neutral curve when $Pr = 0$ is shown by the solid curve in figure 2.18. Here, we impose the symmetry I to the disturbances and set the wavenumber $\alpha = 1.0$. The laminar flow becomes unstable inside the curve. The unstable

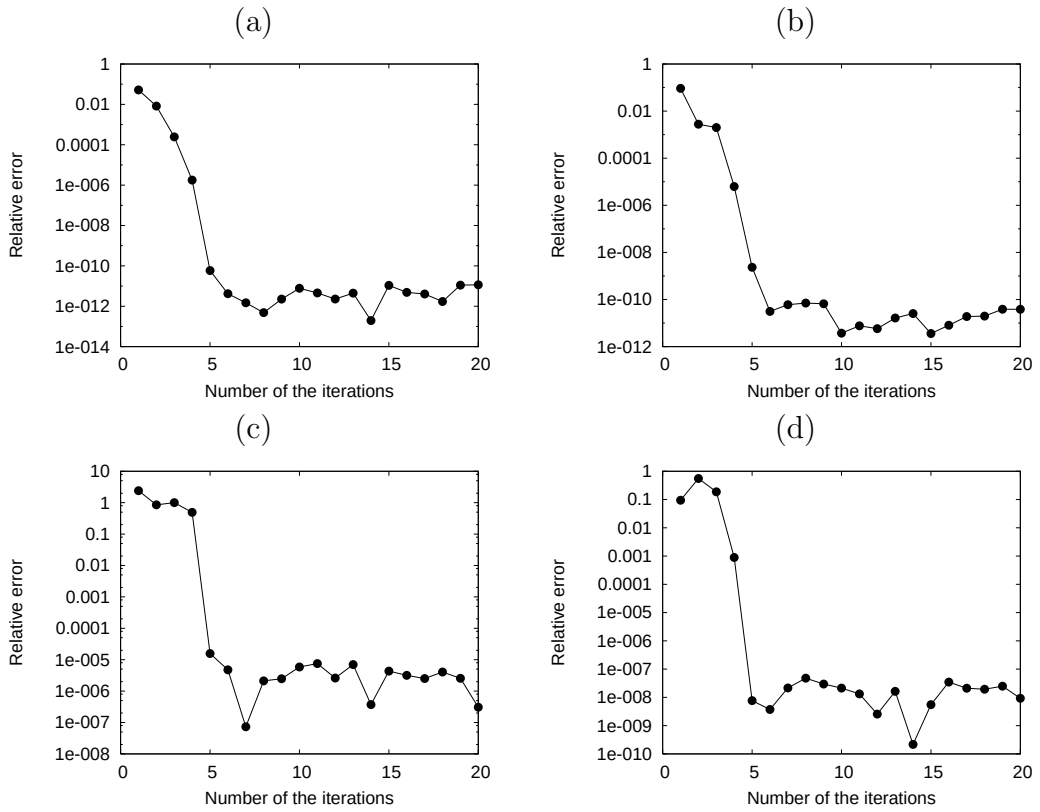

Figure 2.17: The relative errors for (a) the phase velocity c, (b) $\Re[v_{1,4,2}]$, (c) $\Re[v_{6,31,16}]$ and (d) $\Re[v_{6,33,32}]$ against the number of the iterations.

region when $Pr = 0$ exists mainly in M_3 and is almost included in that of $Pr = 7$ (shown by the dashed curve in figure 2.18). This instability is not detected in Uhlmann & Nagata (2006) because they only investigate the parameter range $0 \leq Gr \leq 8000$.

The continuation path to the isothermal solution when $Pr = 0$ is shown by the arrows in figure 2.18. The path is made up by the two sections: (a) increasing Re from -3934 (the linear critical point) to 1000 by fixing $Gr = 30000$, (b) decreasing Gr from 30000 down to zero by fixing $Re = 1000$. The variation of Re_b in each section is shown in figure 2.19. Figure 2.19(a) shows the bifurcation of the nonlinear solution from the critical point $(Re, Gr) = (-3934, 30000)$ (the open triangle) when fixing $Gr = 30000$. The bulk Reynolds number monotonically increases as the Reynolds number increases. The nonlinear solution at $(Re, Gr) = (1000, 30000)$ is indicated by the open circle in figure 2.19(a), (b). In figure 2.19, we reduce the Grashof number from 30000 and obtain the isothermal solution (the intersection between the bifurcation curve and the line $Gr = 0$ shown by the upper closed circle). The nonlinear solution undergoes

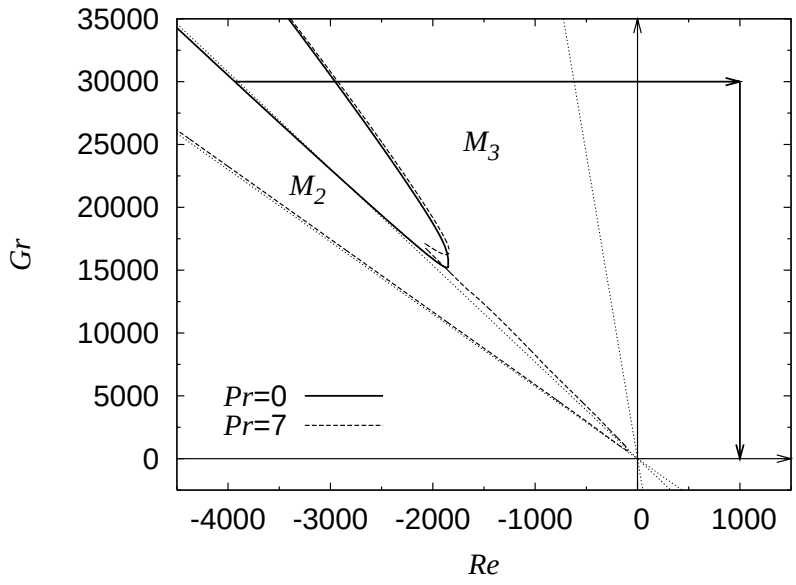

Figure 2.18: The path taken from the linear critical point of the internally heated duct flow to the isothermal solution indicated by the arrows when $Pr = 0$. The solid and dashed curves show the neutral curve with $\alpha = 1.0$ when $Pr = 0$ and $Pr = 7$, respectively. The region M_2 and M_3 are represented by $-7.69 < Gr/Re < -5.75$ and $-48.40 < Gr/Re < -7.69$, respectively.

the turning point at $Gr = -962$ and crosses $Gr = 0$ again (lower closed circle). The upper and lower closed circles correspond to the lower and upper branches of the isothermal solution obtained in section 2.4.

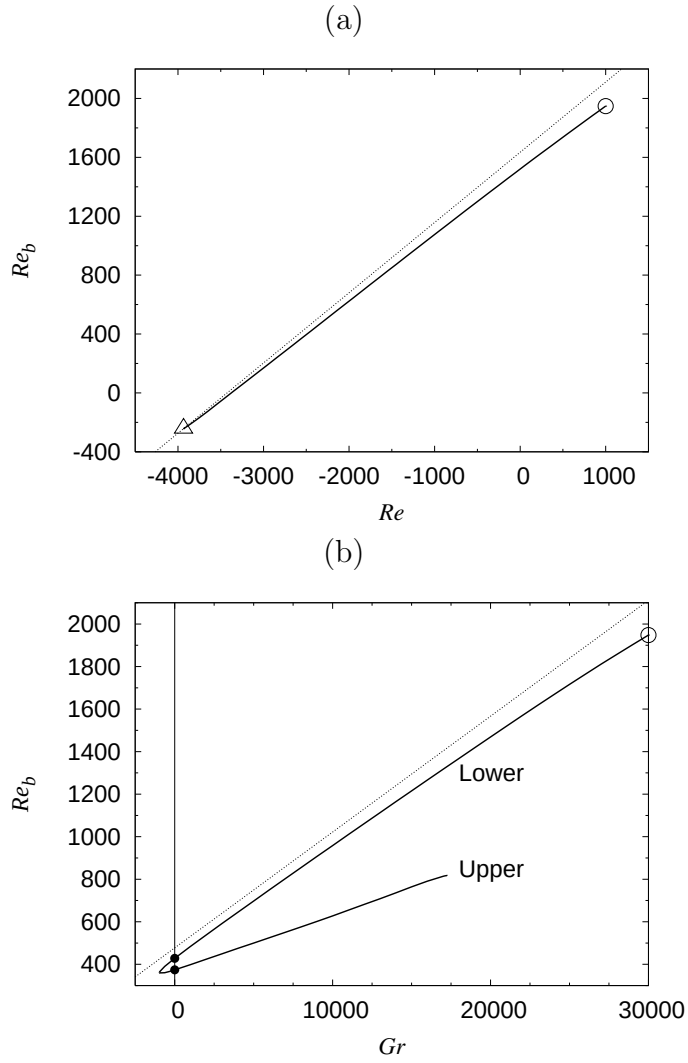

Figure 2.19: The variation of Re_b along the path in figure 2.18. (a) $Gr = 30000$, (b) $Re = 1000$. Two closed circles correspond to the isothermal solutions. The dotted line shows the laminar state, $Re_b = 0.47704Re + 0.054480Gr$. The bifurcation point is indicated by the open triangle.

Chapter 3

Asymmetric Travelling Wave Solutions

Linear stability analysis of the mirror-symmetric solutions in square duct flow discovered by Okino *et al.*, *J. Fluid Mech.* **657**, 413 (2010) is investigated. The solution is found to be unstable from the onset. Two types of asymmetric solutions, which emerge through a symmetry breaking bifurcation from the mirror-symmetric solutions, are found numerically. One of them is characterised by a pair of streamwise vortices and a low-speed streak localized near one of the side walls and retains the shift-and-reflect symmetry. The bifurcation nature as well as the flow structure of the solution shows striking resemblance to those of the asymmetric solution in pipe flow found by Pringle and Kerswell, *Phys. Rev. Lett.* **99**, 074502 (2007), despite the geometrical difference between their cross sections. The solution seems to be embedded in the edge state of square duct flow identified by Biau and Bottaro, *Phil. Trans. Roy. Soc.* A **367**, 529 (2009). The other is slightly deviated from the mirror-symmetric solution from which it bifurcates: the shift-and-rotate symmetry is retained but the mirror symmetry is broken.

3.1 Stability analysis of the mirror-symmetric travelling waves

In order to investigate the stability of the travelling wave solution, $(\boldsymbol{u}_{TW}, P_{TW})$, found in the previous chapter, we superimpose infinitesimal perturbations, $(\tilde{\boldsymbol{u}}, \tilde{P})$, on the solution.

$$\begin{pmatrix} \boldsymbol{u} \\ P \end{pmatrix} = \begin{pmatrix} \boldsymbol{u}_{TW} \\ P_{TW} \end{pmatrix} + \begin{pmatrix} \tilde{\boldsymbol{u}} \\ \tilde{P} \end{pmatrix}. \tag{3.1}$$

Substituting (3.1) into (2.1) and (2.2), we obtain the governing equations for the perturbations:

$$\nabla \cdot \tilde{\boldsymbol{u}} = 0, \tag{3.2}$$

and

$$\partial_t \tilde{\boldsymbol{u}} + (\bar{\boldsymbol{U}} \cdot \nabla)\tilde{\boldsymbol{u}} + (\tilde{\boldsymbol{u}} \cdot \nabla)\bar{\boldsymbol{U}} + (\check{\boldsymbol{u}} \cdot \nabla)\tilde{\boldsymbol{u}} + (\tilde{\boldsymbol{u}} \cdot \nabla)\check{\boldsymbol{u}} = -\nabla \tilde{P} + \nabla^2 \tilde{\boldsymbol{u}}, \tag{3.3}$$

where the nonlinear term, $(\tilde{\boldsymbol{u}} \cdot \nabla)\tilde{\boldsymbol{u}}$, is neglected. Operating $\boldsymbol{e}_z \cdot \nabla \times$ and $\boldsymbol{e}_y \cdot \nabla \times$ on (3.3) leads to

$$\begin{aligned} &\Big[\{\partial_t + (\bar{\boldsymbol{U}} \cdot \nabla) - \nabla^2 + \partial_y \hat{V}\}\partial_x - \partial_{yy}^2 \bar{U}\Big]\tilde{v} \\ &-\Big[\{\partial_t + (\bar{\boldsymbol{U}} \cdot \nabla) - \nabla^2 + \partial_y \hat{V}\}\partial_y + \partial_y \hat{W}\partial_z\Big]\tilde{u} \\ &\qquad +\Big(\partial_y \bar{U}\partial_z - \partial_z \bar{U}\partial_y - \partial_{yz}^2 \bar{U} + \partial_z \hat{V}\partial_x\Big)\tilde{w} \\ &\qquad\qquad +\boldsymbol{e}_z \cdot \nabla \times \{(\check{\boldsymbol{u}} \cdot \nabla)\tilde{\boldsymbol{u}} + (\tilde{\boldsymbol{u}} \cdot \nabla)\check{\boldsymbol{u}}\} = 0, \end{aligned} \tag{3.4}$$

$$\begin{aligned} &\Big[\{\partial_t + (\bar{\boldsymbol{U}} \cdot \nabla) - \nabla^2 + \partial_z \hat{W}\}\partial_x - \partial_{zz}^2 \bar{U}\Big]\tilde{w} \\ &-\Big[\{\partial_t + (\bar{\boldsymbol{U}} \cdot \nabla) - \nabla^2 + \partial_z \hat{W}\}\partial_z + \partial_z \hat{V}\partial_y\Big]\tilde{u} \\ &\qquad +\Big(\partial_z \bar{U}\partial_y - \partial_y \bar{U}\partial_z - \partial_{yz}^2 \bar{U} + \partial_y \hat{W}\partial_x\Big)\tilde{v} \\ &\qquad\qquad -\boldsymbol{e}_y \cdot \nabla \times \{(\check{\boldsymbol{u}} \cdot \nabla)\tilde{\boldsymbol{u}} + (\tilde{\boldsymbol{u}} \cdot \nabla)\check{\boldsymbol{u}}\} = 0. \end{aligned} \tag{3.5}$$

Based on the Floquet theory, the velocity perturbations, $\tilde{\boldsymbol{u}}$, is expanded as follows:

$$\tilde{\boldsymbol{u}}(x, y, z, t) = \sum_{l=-L}^{L} \tilde{\boldsymbol{u}}_l \exp\big[i(l\alpha + d)(x - ct) + \sigma t\big], \tag{3.6}$$

where σ is the growth rate. In this chapter, we only investigate the fundamental mode, $d = 0$. The interaction of the perturbations $\tilde{\boldsymbol{u}}$ and the disturbances $\check{\boldsymbol{u}}$ generates the feedbacks on the mean part. Therefore, we include the x-independent parts $(\tilde{U}, \tilde{V}, \tilde{W}) = (\tilde{u}_0, \tilde{v}_0, \tilde{w}_0)\exp[\sigma t]$ of the perturbations in (3.6) (cf. (2.27)). $\tilde{V}$ and $\tilde{W}$ are derived from the stream function $\tilde{\varphi}$ on the cross section:

$$\tilde{V} = \partial_z \tilde{\varphi}, \quad \tilde{W} = -\partial_y \tilde{\varphi}. \tag{3.7}$$

Taking the streamwise average of $\boldsymbol{e}_x \cdot$(3.3) and $\boldsymbol{e}_x \cdot \nabla \times$(3.3) leads to

$$\begin{aligned} &(\partial_t + \partial_z \hat{\varphi}\partial_y - \partial_y \hat{\varphi}\partial_z - \triangle_2)\tilde{U} + (\partial_z \tilde{\varphi}\partial_y - \partial_y \tilde{\varphi}\partial_z)\bar{U} \\ &\qquad + \partial_y \overline{\check{u}\check{v} + \tilde{u}\check{v}} + \partial_z \overline{\check{u}\check{w} + \tilde{u}\check{w}} = 0, \end{aligned} \tag{3.8}$$

$$\begin{aligned} &-(\partial_t + \partial_z \hat{\varphi}\partial_y - \partial_y \hat{\varphi}\partial_z - \triangle_2)\triangle_2 \tilde{\varphi} - (\partial_z \tilde{\varphi}\partial_y - \partial_y \tilde{\varphi}\partial_z)\triangle_2 \hat{\varphi} \\ &\qquad + (\partial_{yy}^2 - \partial_{zz}^2)\overline{\check{v}\check{w} + \check{v}\tilde{w}} + 2\partial_{yz}^2 \overline{\check{w}\tilde{w} - \check{v}\tilde{v}} = 0, \end{aligned} \tag{3.9}$$

where $\tilde{u}$ is solved by using (3.2) as $\tilde{u} = \tilde{U} - \partial_x^{-1}(\partial_y \tilde{v} + \partial_z \tilde{w})$.

The variables, $\tilde{u}_0$, $\tilde{\varphi}_0 (= \tilde{\varphi}/\exp[\sigma t])$, $\tilde{v}_l$ and $\tilde{w}_l$ satisfy the following boundary conditions:

$$\tilde{u}_0 = \tilde{\varphi}_0 = \partial_y \tilde{\varphi}_0 = \partial_z \tilde{\varphi}_0 = \tilde{v}_l = \tilde{w}_l = \partial_y \tilde{v}_l = 0 \quad \text{at} \quad y = \pm 1, \tag{3.10}$$

$$\tilde{u}_0 = \tilde{\varphi}_0 = \partial_y \tilde{\varphi}_0 = \partial_z \tilde{\varphi}_0 = \tilde{v}_l = \tilde{w}_l = \partial_z \tilde{w}_l = 0 \quad \text{at} \quad z = \pm 1. \tag{3.11}$$

All the variable are expanded using the appropriate basis functions, which satisfies the boundary conditions (see (2.35) and (2.36)).

$$\begin{pmatrix} \tilde{v}_l \\ \tilde{w}_l \\ \tilde{u}_0 \\ \tilde{\varphi}_0 \end{pmatrix} = \sum_{m=2}^{M} \sum_{n=2}^{N} \begin{pmatrix} \tilde{v}_{lmn} \phi_m(y) \psi_n(z) \\ \tilde{w}_{lmn} \psi_m(y) \phi_n(z) \\ \tilde{u}_{0mn} \psi_m(y) \psi_n(z) \\ \tilde{\varphi}_{0mn} \phi_m(y) \phi_n(z) \end{pmatrix}. \tag{3.12}$$

The Galerkin projection of (3.4), (3.5), (3.8) and (3.9) gives a generalized eigenvalue problem with the growth rate σ as the eigenvalue,

$$\tilde{A}_{ij} \tilde{x}_j = \sigma \tilde{B}_{ij} \tilde{x}_j, \tag{3.13}$$

where $\tilde{x}_j$ stands for $(\tilde{v}_{lmn}, \tilde{w}_{lmn}, \tilde{u}_{0mn}, \tilde{\varphi}_{0mn})^T$, with $l = \pm 1, \cdots, \pm L$. The equation is solved by the LAPACK routines, ZGESV and ZGEEV.

Recall that the travelling wave found in the previous section, which we refer to as ONWB hereafter, is invariant under the following transformations: the shift-and-reflection,

$$\mathbf{S} : \begin{pmatrix} u \\ v \\ w \end{pmatrix} (\xi, y, z) \to \begin{pmatrix} u \\ -v \\ w \end{pmatrix} (\xi + \frac{\pi}{\alpha}, -y, z), \tag{3.14}$$

and the mirror-reflection,

$$\mathbf{Z} : \begin{pmatrix} u \\ v \\ w \end{pmatrix} (\xi, y, z) \to \begin{pmatrix} u \\ v \\ -w \end{pmatrix} (\xi, y, -z), \tag{3.15}$$

where $\xi = x - ct$. The combination of $\mathbf{S}$ and $\mathbf{Z}$ leads to the shift-and-rotation,

$$\mathbf{\Omega} : \begin{pmatrix} u \\ v \\ w \end{pmatrix} (\xi, y, z) \to \begin{pmatrix} u \\ -v \\ -w \end{pmatrix} (\xi + \frac{\pi}{\alpha}, -y, -z). \tag{3.16}$$

Examining the governing equations for the perturbations, (3.4), (3.5), (3.8) and (3.9), we find that the following four symmetry groups for $\tilde{v}_l$, $\tilde{w}_l$, $\tilde{u}_0$ and $\tilde{\varphi}_0$ are admissible:

symmetry IA :

$$\tilde{v}_l \begin{cases} (l^{\,+}; e, e) \\ (l^{++}; o, e) \end{cases}, \ \tilde{w}_l \begin{cases} (l^{\,+}; o, o) \\ (l^{++}; e, o) \end{cases}, \ \tilde{u}_0(e, e), \ \tilde{\varphi}_0(o, o), \tag{3.17}$$

symmetry IB :

$$\tilde{v}_l \begin{cases} (l^{\,+}; e, o) \\ (l^{++}; o, o) \end{cases}, \ \tilde{w}_l \begin{cases} (l^{\,+}; o, e) \\ (l^{++}; e, e) \end{cases}, \ \tilde{u}_0(e, o), \ \tilde{\varphi}_0(o, e), \tag{3.18}$$

symmetry IC :

$$\tilde{v}_l \begin{cases} (l^{\,+}; o, e) \\ (l^{++}; e, e) \end{cases}, \ \tilde{w}_l \begin{cases} (l^{\,+}; e, o) \\ (l^{++}; o, o) \end{cases}, \ \tilde{u}_0(o, e), \ \tilde{\varphi}_0(e, o), \tag{3.19}$$

symmetry ID :

$$\tilde{v}_l \begin{cases} (l^{\,+}; o, o) \\ (l^{++}; e, o) \end{cases}, \ \tilde{w}_l \begin{cases} (l^{\,+}; e, e) \\ (l^{++}; o, e) \end{cases}, \ \tilde{u}_0(o, o), \ \tilde{\varphi}_0(e, e). \tag{3.20}$$

The symmetry IA is the same as the one that the solution ONWB possesses: the perturbations are invariant under the transformations $\mathbf{S}$ and $\mathbf{Z}$ (and therefore, $\mathbf{\Omega}$ also). It is immediately verified that the symmetry IB, IC and ID individually have the symmetry $\mathbf{S}$, $\mathbf{Z}$ and $\mathbf{\Omega}$, respectively.

Figure 3.1 shows the real part of the growth rate σ of the fundamental mode of the perturbations with symmetry IA imposed on ONWB with $\alpha = 1.14$. This travelling wave solution is unstable from its appearance at the saddle-node bifurcation at $Re = 827.5$: while the lower branch has two unstable eigenmodes the number of unstable eigenmodes increases on the upper branch as the Reynolds number increases. The solution on both branches always presents an eigenmode with zero growth rate, which corresponds to the infinitesimal translation in the streamwise direction. The magnified figure in figure 3.1(c) shows that the growth rates of the upper and lower branches join at the saddle-node. In particular, as expected from the nature of the saddle-node bifurcation, where the upper branch must have one more unstable direction than the lower branch, the third largest real growth rate on the upper branch connects with the third largest (negative) real growth rate of the lower branch at zero. The second and third largest real growth rates on the upper branch near the saddle-node join to become a complex conjugate pair as Re is slightly increased. All the growth rates which cross zero on the upper branch for larger

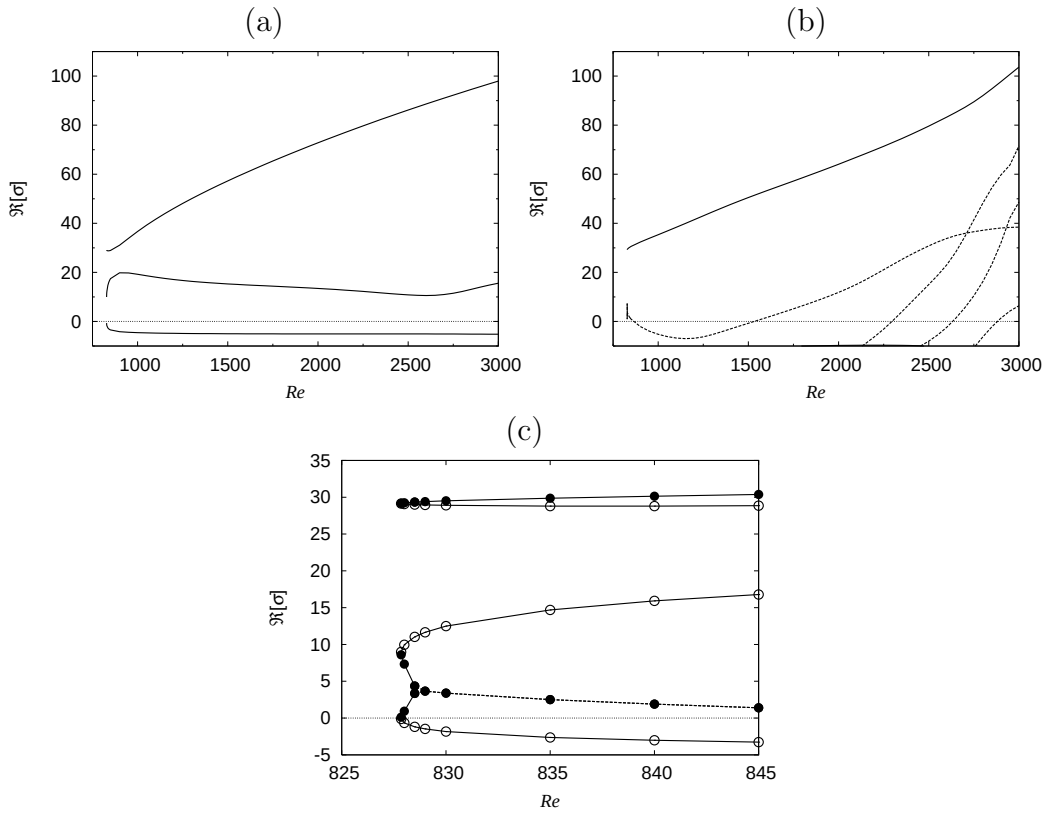

Figure 3.1: The real part of the growth rate, $\Re[\sigma]$, of the perturbations with the symmetry IA on the (a) lower and (b) upper branches of ONWB with $\alpha = 1.14$. Solid and dotted curves, respectively, indicate that the growth rates are real and complex conjugate. (c) The close-up. Curves with open and closed circles correspond to the lower and upper branch, respectively.

Re are associated with a complex conjugate pair so that time-periodic solutions in the frame moving with the travelling wave are expected to bifurcate there.

Figures 3.2(a) and (b) show the real part of the growth rate σ of the perturbations with the symmetry IB on the lower and upper branches of ONWB, respectively. On the lower branch, the most unstable eigenmode has a complex conjugate eigenvalue at $Re = 827.5$. It decreases as the Reynolds number increases. The neutral point is found at $Re \sim 1450$. The second largest eigenvalue, which starts as a complex conjugate pair, splits into two real eigenvalues at $Re \sim 1000$, and the larger one crosses zero at $Re \sim 1080$ (open circle). Figure 3.2(b) shows that the second eigenmode with symmetry IB, associated with a complex eigenvalue at the saddle-node of ONWB, crosses zero at $Re \sim 880$ and splits into two real modes at $Re \sim 1450$. The smaller one becomes neutral when $Re \sim 1480$ (closed circle). No other neutral points associated with a real

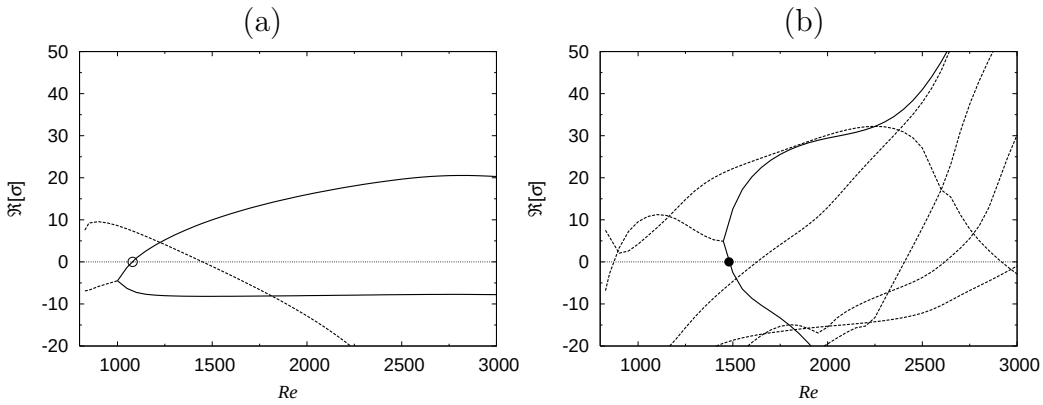

Figure 3.2: Same as figure 3.1 for the symmetry IB.

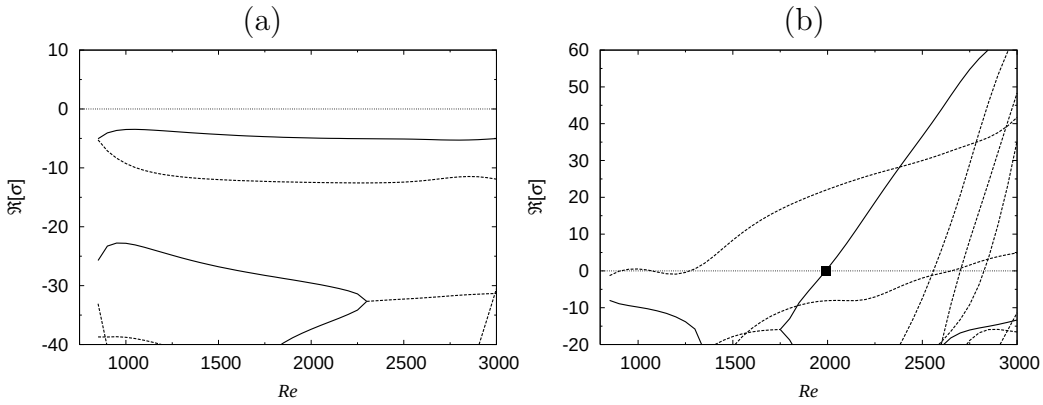

Figure 3.3: Same as figure 3.1 for the symmetry IC.

eigenvalue are found when $Re \leq 3000$.

Figure 3.3(a) shows the lower branch of ONWB is always stable to the perturbations with the symmetry IC within the parameter range of our investigation. On the upper branch, the leading eigenvalue appears as a complex conjugate pair. They cross zero three times until $Re \sim 1300$ and take positive growth rates afterward (see figure 3.3b). Only one neutral mode associated with a real eigenvalue for the symmetry IC is found at $Re \sim 1990$ on the upper branch (closed square).

The growth rate of the perturbations with the symmetry ID is shown in figure 3.4. No unstable eigemode appear when $Re \leq 3000$ on the lower branch of ONWB as shown in figure 3.4(a). Figure 3.4(b) represents the upper branch solution is stable to the perturbations with the symmetry ID until five unstable eigenmodes (one real and two complex conjugate pairs) appear almost at once near $Re = 1400$ (closed triangle). We find two eigenmodes with the real

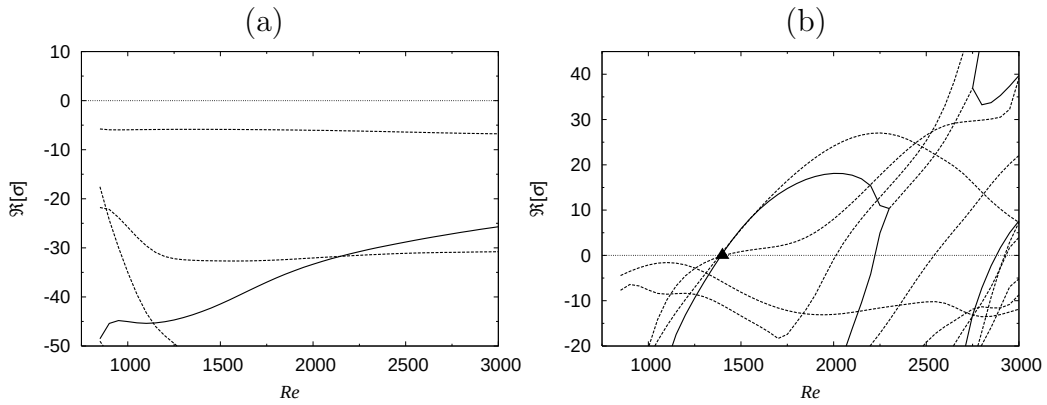

Figure 3.4: Same as figure 3.1 for the symmetry ID.

eigenvalue cross zero at $Re \sim 2220$ and $Re \sim 2880$.

3.2 Asymmetric solutions

We are interested in only nonlinear solutions that bifurcate from ONWB at the neutral points with the real eigenvalues because the bifurcating solution appears as the travelling wave state. Bifurcating solutions from a nonlinear solution with the symmetry I are classified into the following three groups depending on the symmetry of the perturbations.

symmetry I+II:

$$v_l \begin{Bmatrix} (l^+;e,e) \\ (l^+;e,o) \\ (l^{++};o,e) \\ (l^{++};o,o) \end{Bmatrix}, \; w_l \begin{Bmatrix} (l^+;o,o) \\ (l^+;o,e) \\ (l^{++};e,o) \\ (l^{++};e,e) \end{Bmatrix}, \; \hat{U} \begin{Bmatrix} (e,e) \\ (e,o) \end{Bmatrix}, \; \hat{\varphi} \begin{Bmatrix} (o,o) \\ (o,e) \end{Bmatrix}, \tag{3.21}$$

symmetry I+III:

$$v_l \begin{Bmatrix} (l^+;e,e) \\ (l^+;o,e) \\ (l^{++};o,e) \\ (l^{++};e,e) \end{Bmatrix}, \; w_l \begin{Bmatrix} (l^+;o,o) \\ (l^+;e,o) \\ (l^{++};e,o) \\ (l^{++};o,o) \end{Bmatrix}, \; \hat{U} \begin{Bmatrix} (e,e) \\ (o,e) \end{Bmatrix}, \; \hat{\varphi} \begin{Bmatrix} (o,o) \\ (e,o) \end{Bmatrix}, \tag{3.22}$$

symmetry I+IV:

$$v_l \begin{Bmatrix} (l^+;e,e) \\ (l^+;o,o) \\ (l^{++};o,e) \\ (l^{++};e,o) \end{Bmatrix}, \; w_l \begin{Bmatrix} (l^+;o,o) \\ (l^+;e,e) \\ (l^{++};e,o) \\ (l^{++};o,e) \end{Bmatrix}, \; \hat{U} \begin{Bmatrix} (e,e) \\ (o,o) \end{Bmatrix}, \; \hat{\varphi} \begin{Bmatrix} (o,o) \\ (e,e) \end{Bmatrix}. \tag{3.23}$$

The solutions with the symmetry I+II, I+III and I+IV bifurcate due to the instability of the perturbations with the symmetry IB, IC and ID, respectively

and therefore, they are invariant under the transformation **S**, **Z** and **Ω**, respectively.

Using the eigenfuction at the neutral points as an initial guess of the Newton-Raphson method, we obtain two bifurcating solutions from ONWB with $\alpha = 1.14$. The bulk Reynolds numbers for these solutions as well as ONWB are plotted against the Reynolds number in figure 3.5(a). The skin frictions against the bulk Reynolds number are also shown in figure 3.5(b). The dotted curve in figure 3.5 indicates the ONWB branch. A new solution, which results from the instability due to the symmetry IB and has the symmetry I+II, bifurcates subcritically from the lower branch of ONWB at $Re = 1077, Re_b = 468$ (open circle), undergoes two turning points at $Re = 969$ and 1753, and terminates on the upper branch of ONWB at $Re = 1483, Re_b = 490$ (closed circle). This solution branch connects the bifurcation points indicated by the open and closed circles in figure 3.2. We refer to this solution as the **S**-symmetric solution. Another new solution, which results from the instability due to the symmetry ID and has the symmetry I+IV, bifurcates supercritically from the upper branch at $Re = 1393, Re_b = 467$ (closed triangle). This solution is referred to as the **Ω**-symmetric solution. The solution with the symmetry I+III (i.e. the bifurcating solution due to the instability of the symmetry IC at $Re \sim 1990$) is not calculated here.

3.2.1 S-symmetric solution

The mean and the total flow of the **S**-symmetric solution with $\alpha = 0.7$ at $Re = 3000$ are shown in figure 3.6. The mirror-symmetry with respect to $z = 0$ of ONWB is broken (compare figure 3.6 and 2.12) and strong disturbances, which are composed of a pair of streamwise vortices and a low-speed streak, are observed near the side wall $z = +1$. The solution, which has the same structures near $z = -1$, is also a possibility by the symmetry of the system. The mean flow is mirror-symmetric with respect to $y = 0$ (taking the streamwise average of (3.14) leads to the symmetry for mean flow: $(\bar{U}, \bar{V}, \bar{W})(y, z) = (\bar{U}, -\bar{V}, \bar{W})(-y, z)$, where $\bar{U} = \int_0^{2\pi/\alpha} u \, \mathrm{d}x$, etc.). Figure 3.7 shows the iso-surfaces of the srreamwise vorticity and the streamwise velocity of the solution. A pair of quasi-streamwise vortices attached to one of the side walls is clearly seen. The disturbance velocity of the **S**-symmetric solution is shown in figure 3.8. The left and the right frames present the mean part and the instantaneous flow, respectively. These flow structures of this solution exhibits a striking similarity to those of the asymmetric solution in a pipe by Pringle & Kerswell (2007) (see figure 3.9). These two solutions possess the

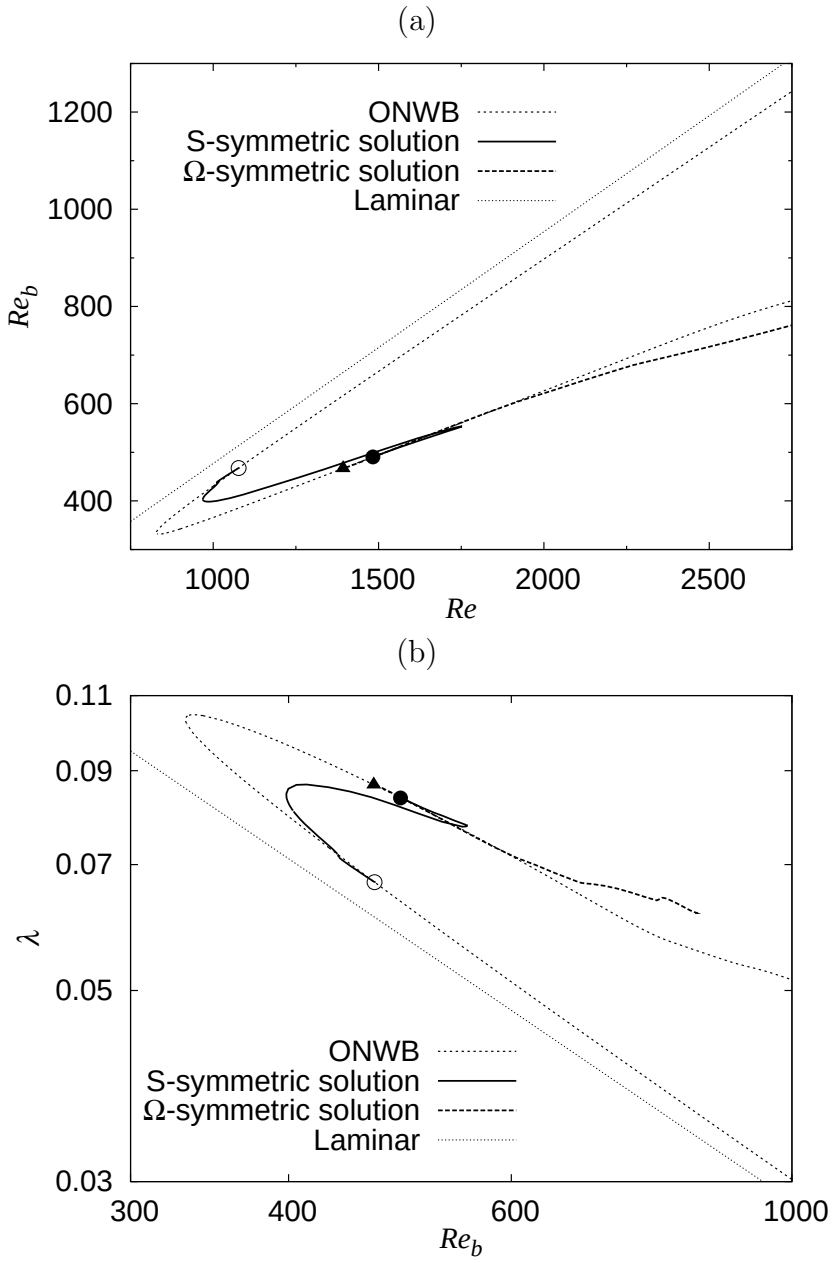

Figure 3.5: (a) The bulk Reynolds number versus the Reynolds number for $\alpha = 1.14$. Dotted curve: ONWB. Solid curve: The **S**-symmetric solution. Dashed curve: The **Ω**-symmetric solution. Thin dotted line: The laminar state, $Re_b = 0.47704Re$. The circles and the triangle show the bifurcation points. (b) The skin friction against the bulk Reynolds number. Thin dotted line: The laminar state, $\lambda = 28.45/Re_b$.

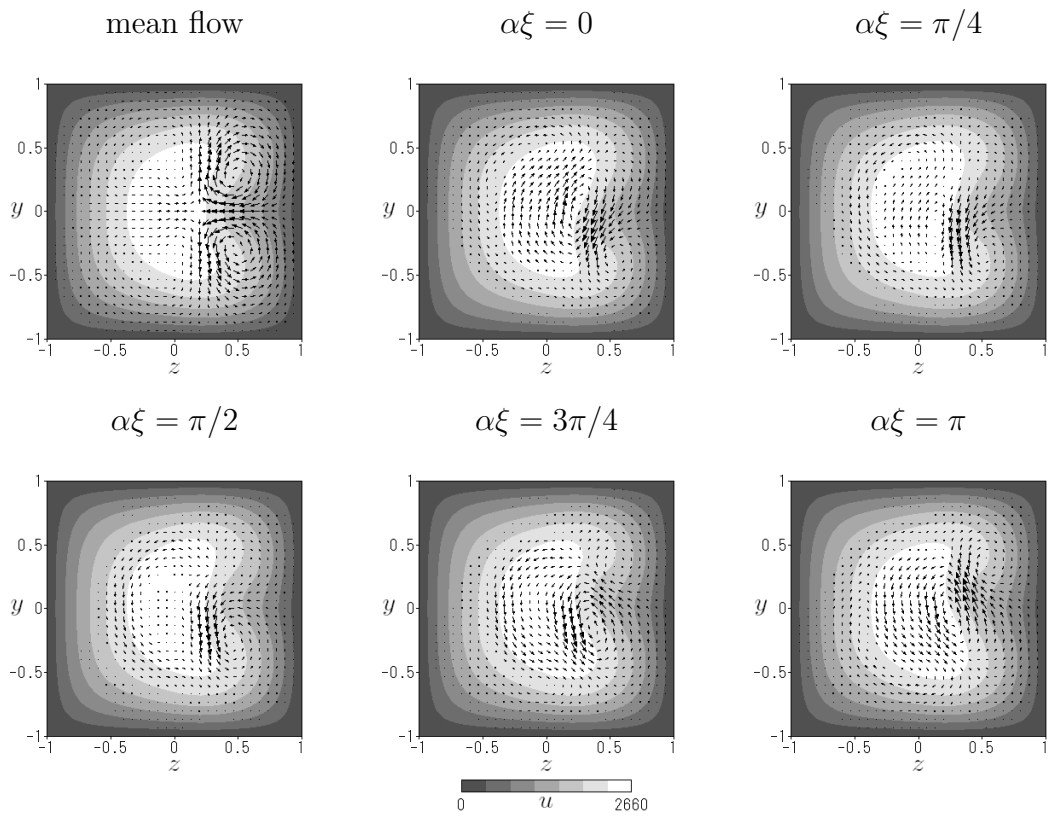

Figure 3.6: Mean flow $\bar{\boldsymbol{U}}$ (top-left) and images of the total flows $\boldsymbol{u}$ along ξ of the **S**-symmetric solution with $\alpha = 0.7$ at $Re = 3000$ ($Re_b = 1342$). The velocity components are shown on the y-z plane (arrows) and along the x-direction (grey scale). $\xi = x - ct$.

shift-and-reflect symmetry in common. Strong similarity for the two solutions is also observed in the skin friction (compare figure 3.5b with figure 3.10).

Figure 3.11 shows the existence domains of the **S**-symmetric solution. The solution connects the lower and the upper branch of ONWB. Our **S**-symmetric travelling waves appear at $\alpha = 1.36$, $Re = 924$ ($Re_b = 374$) and their minimum bulk Reynolds number is 365 at $\alpha = 1.38$, $Re = 952$. The existence domain has more turning points on the α–Re_b plane as the Reynolds number increases: the number of solutions increases for a fixed wavenumber.

The invariant set on the boundary between the laminar and turbulent states in phase space is called the edge state. The trajectory, which starts with an initial condition near the laminar-turbulent boundary transiently approaches the edge state before the flow uneventfully relaminalizes or evolves into turbulence (Biau & Bottaro 2009; Duguet, Willis & Kerswell 2008; Itano & Toh 2001; Mellibovsky & Meseguer 2009; Schneider *et al.* 2007, 2008; Schneider &

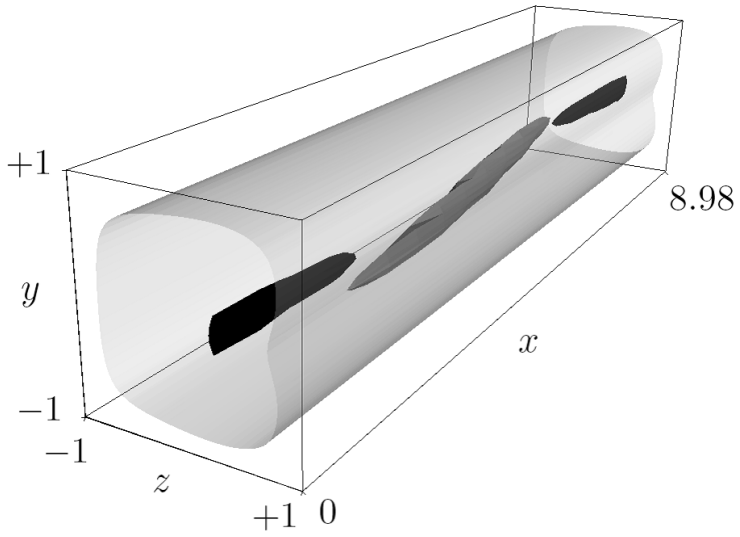

Figure 3.7: The iso-surfaces of the streamwise vorticity and the streamwise velocity of the **S**-symmetric solutions with $\alpha = 0.7$, $Re = 3000$ ($Re_b = 1342$). Black (dark grey) represents +70% (-70%) of the maximum vorticity and light grey represents 40% of the maximum velocity. The flow is from left to right.

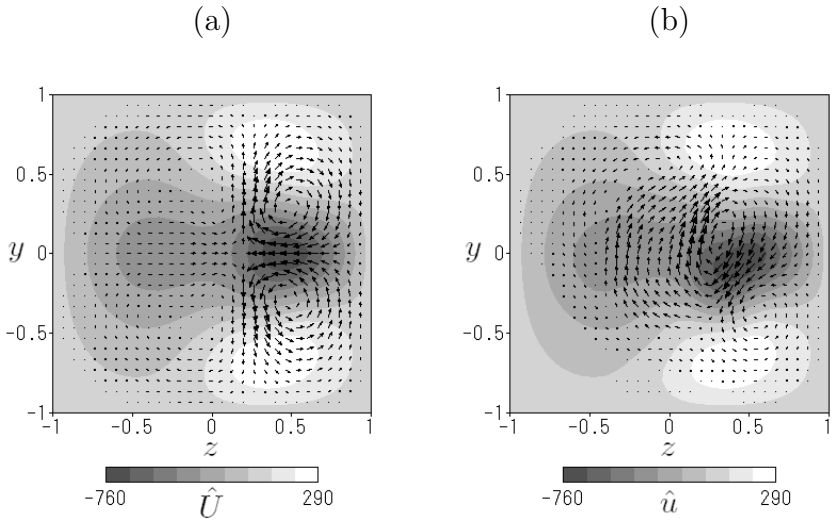

Figure 3.8: (a) The mean part and (b) the instantaneous flow of the disturbance of the **S**-symmetric solution with $\alpha = 0.7$, $Re = 3000$ ($Re_b = 1342$). The velocities on the y-z plane and along the x-direction are indicated by the arrows and the grey scale.

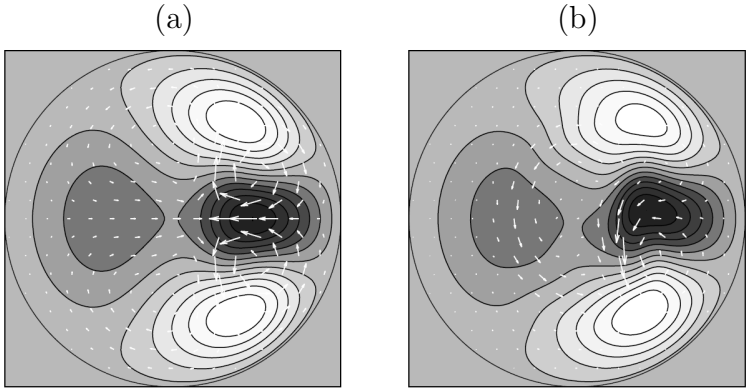

Figure 3.9: The top frames of figure 1 of Pringle & Kerswell (2007). Velocity fields of the disturbance for the asymmetric travelling wave in a pipe. (a) The mean part. (b) The instantaneous field.

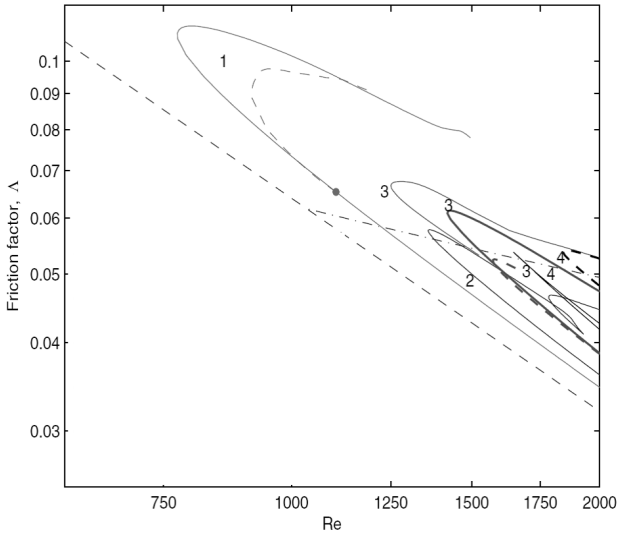

Figure 3.10: Figure 6 of Pringle & Kerswell (2007). Friction factor Λ against the bulk Reynolds number Re for the various travelling wave families. The dashed line indicates the laminar value $\Lambda_{\rm lam} = 64/\mathrm{Re}$. The dash-and-dotted line indicates the experimental data $1/\sqrt{\Lambda} = 2.0\log(\mathrm{Re}\sqrt{\Lambda})$. The labels m indicate the different travelling wave solutions with the rotational symmetry by $2\pi/m$. The mirror-symmetric solution and the asymmetric solution are shown by the solid and the dashed curves, respectively. The bifurcation point where the asymmetric solution appears is marked by the dot.

Eckhardt 2009; Wang *et al.* 2007). The temporal variation of the skin friction and the instantaneous secondary flows of the edge state in square duct flow is shown in figure 3.12 and 3.13, respectively. The edge state of square

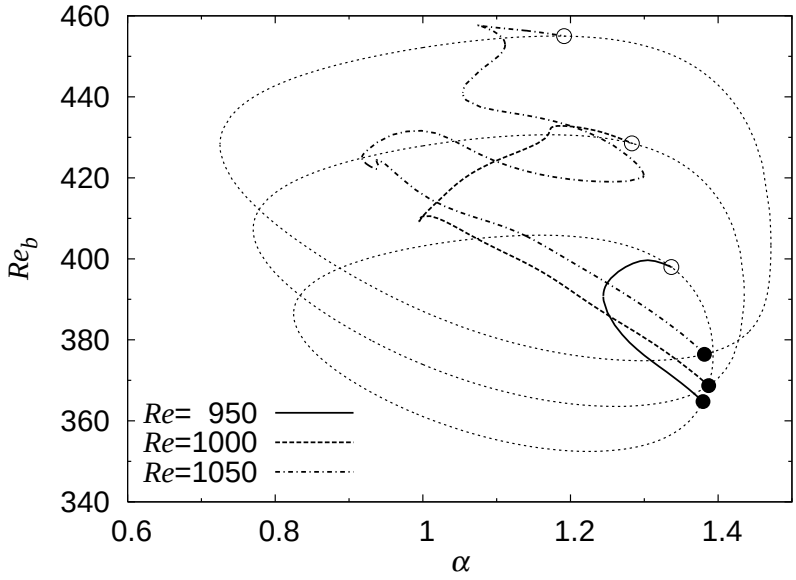

Figure 3.11: The existence domains of the **S**-symmetric solutions. Solid curve: $Re = 950$. Dashed curve: $Re = 1000$. Dash-and-dotted curve: $Re = 1050$. The dotted curves indicate ONWB at $Re = 950, 1000$ and 1050. The open and closed circles represent the bifurcation points on the lower and upper branches of ONWB.

duct flow is not steady but chaotic. Note that different walls become 'active' as time varies (here, active means a pair of vortices is attached to one of the sides). The mean flow of our **S**-symmetric solution resembles that of the edge state in square duct flow (Biau & Bottaro 2009) (compare the right frame of figure 3.8 with figure 3.13). The properties of the **S**-symmetric solution and the lower branch of other travelling wave solutions with $\alpha = 0.5$ for $Re = 3315$ (this parameter corresponds to $\alpha = 1.0, Re_\tau = 150$ in the notation of Biau & Bottaro 2009) are listed in table 3.1. The edge state takes $0.021 \lesssim \lambda \lesssim 0.024$, $2720 \lesssim Re_b \lesssim 2900$ and $214 \lesssim E_U \lesssim 250$ (see figure 3.12 and figure 7 of Biau & Bottaro 2009). The **S**-symmetric solution and ONWB take the values almost equal to the lower bound of the skin friction and the upper bound of the mean flow energy and the bulk Reynolds number of the edge state, while WBN and UKP have rather higher friction, lower energy and bulk Reynolds number than the edge state The **S**-symmetric solution has a fewer unstable eigenvalues and the values themselves are smaller than those of ONWB (see table 3.2). This implies that the **S**-symmetric solution is more accessible than ONWB in phase space. Note that no symmetry is applied to the perturbations to calculate the stability of the **S**-symmetric solution and ONWB in table 3.2. The edge state

of pipe flow also consists of a pair of streamwise vortices located off center (Duguet, Willis & Kerswell 2008; Mellibovsky & Meseguer 2009; Schneider *et al.* 2007; Schneider & Eckhardt 2009). We expect the edge state in square duct flow is formed around the **S**-symmetric solutions (four **S**-symmetric solutions exist due to the rotational symmetry by 90 degrees in square duct flow) and their heteroclinic connections similar to those shown in Duguet, Willis & Kerswell (2008) for pipe flow.

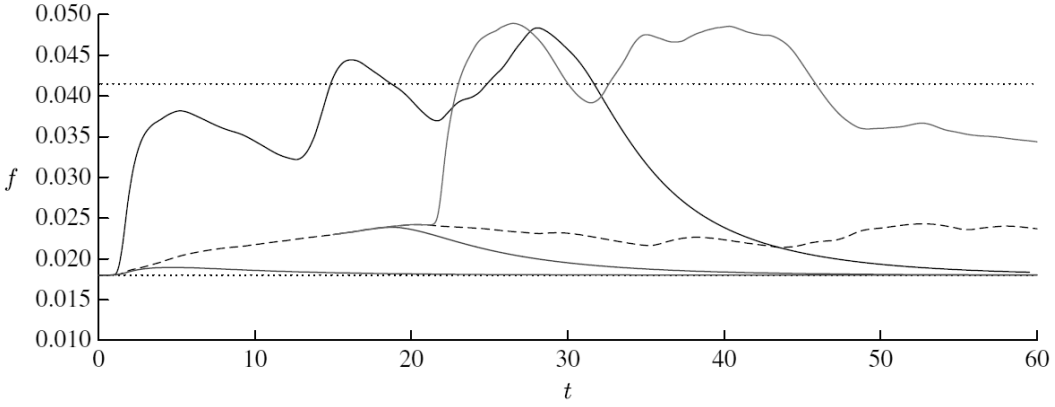

Figure 3.12: Figure 5 of Biau & Bottaro (2009). The skin friction f versus time. The definition of f is same as λ in (2.41). The dashed curve corresponds to the edge state for $\alpha = 0.5$, $Re = 3315$. The lower and upper dotted line indicate the laminar and turbulent values. The solid curves undergo relaminarization or evolution into turbulence. Time t is nondimensionalized by h/u_τ, where h is the side length of the square and u_τ is the friction velocity.

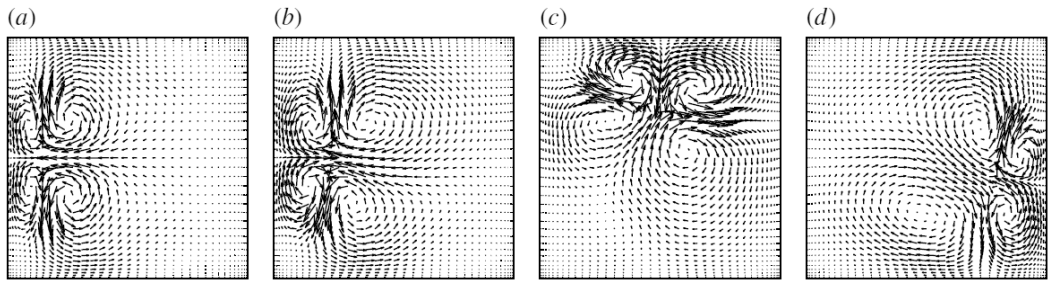

Figure 3.13: Figure 6 of Biau & Bottaro (2009). Instantaneous secondary flows of the solution on the edge for $\alpha = 0.5$, $Re = 3315$. (a) $t = 0.6$, (b) $t = 33$, (c) $t = 40$ and (d) $t = 54$.

Table 3.1: The skin friction λ, bulk Reynolds number Re_b and energy of the streamwise averaged flow $E_U = 1/4 \int_{-1}^{+1} \int_{-1}^{+1} (\bar{U}^2 + \bar{V}^2 + \bar{W}^2)/2 \, \mathrm{d}y\mathrm{d}z$ of the travelling waves with $Re = 3315, \alpha = 0.5$. The values in the bracket are normalized by the scales adopted in Biau & Bottaro (2009). The solutions reported in Wedin *et al.* (2009) and Uhlmann *et al.* (2010) are referred to as WBN and UKP, respectively.

Solution	λ	Re_b	E_U
S-symmetric	0.02087	1468 (2937)	1.439×10^6 (255.8)
ONWB (lower)	0.02099	1464 (2928)	1.429×10^6 (254.1)
WBN (lower)	0.03459	1145 (2290)	8.172×10^5 (145.3)
UKP (lower)	0.02568	1324 (2648)	1.120×10^6 (199.1)

Table 3.2: The five largest eigenvalues of the travelling waves with $Re = 3315, \alpha = 0.5$.

Solution	σ_1	σ_2	σ_3	σ_4	σ_5
S-symmetric	45.2	11.4	3.5	0	-5.2
ONWB (lower)	56.5	19.4	9.3	$7.1 \pm 56.9i$	0

3.2.2 Ω-symmetric solution

Figure 3.14 shows the velocity field of the **Ω**-symmetric solutions. These solutions almost look like the upper branch of ONWB. However, the mirror-symmetry **Z** with respect to $z = 0$ is broken by the pitchfork bifurcation, giving rise to two solutions which are mirror-symmetric with each other. The three-dimensional representation of the solutions is shown in figure 3.15. We can see in the left frame of figure 3.15 for one of the two solutions that the vortices with negative vorticity are elongated in the streamwise direction more than those with positive vorticity. The right figure for the other solution shows an opposite structure.

The existence domains of the **Ω**-symmetric solution are shown in figure 3.16. The solution appears through the saddle-node bifurcation at $\alpha = 1.43$, $Re = 1271$ ($Re_b = 427$). At a slightly larger Reynolds number, the **Ω**-symmetric solution begins to connect with the upper branch of ONWB via a pitchfork bifurcation (the bifurcation points are indicated by the closed triangles). The counterpart of this solution in pipe flow has not been reported yet.

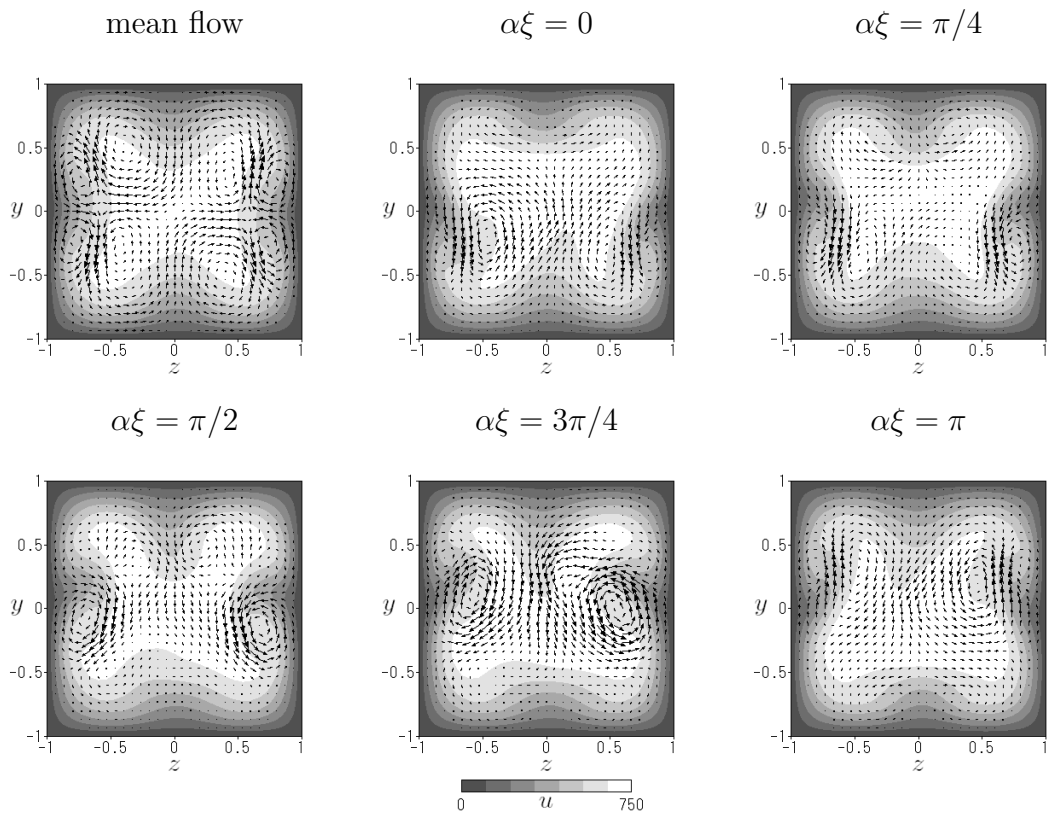

Figure 3.14: Same as figure 3.6 for the **Ω**-symmetric solution with $\alpha = 1.43$ at $Re = 1400$ ($Re_b = 461$).

3.3 Conclusion

We have performed the linear stability analysis of the mirror-symmetric travelling wave, ONWB, and found the neutral points with the real eigenvalue for the lower and upper branches. ONWB is shown to be unstable from the onset. Choosing the eigenfunction at the neutral points as an initial guess of the Newton-Raphson method, we obtain two asymmetric travelling waves, which emerge through the pitchfork bifurcation. One solution has the shift-and-reflect symmetry **S**. The other solution has the shift-and-rotate symmetry **Ω**. The **S**-symmetric solution is characterized by a pair of quasi-streamwise vortices and a low-speed streak near one of the side walls. The **S**-symmetric solution and its bifurcation nature is very similar to those of pipe flow found by Pringle & Kerswell (2007). Also, the mean flow structure and the properties such as the skin friction, the bulk Reynolds number and the mean flow energy of our **S**-symmetric solution shows striking closeness to the edge state calculated by Biau & Bottaro (2009). The **S**-symmetric solution has only three

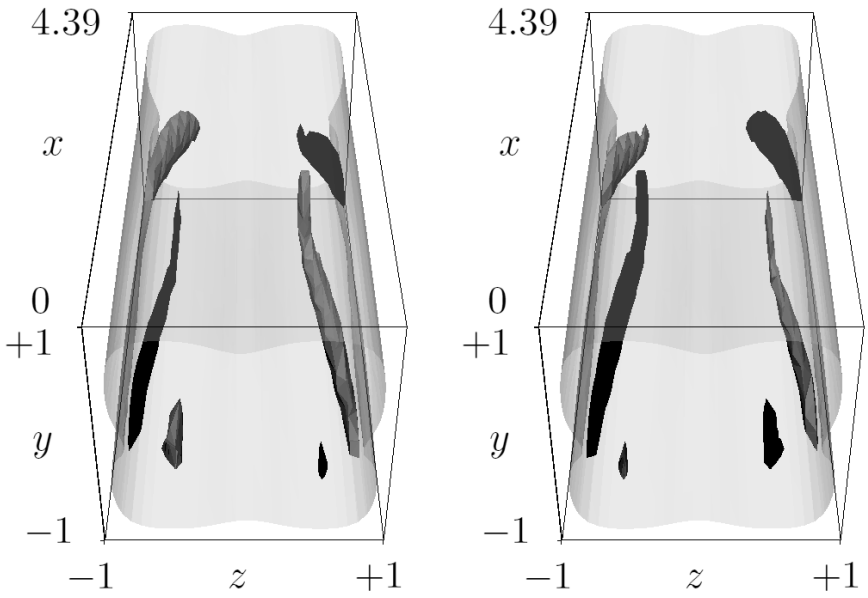

Figure 3.15: The iso-surfaces of the streamwise vorticity and the streamwise velocity of the $\mathbf{\Omega}$-symmetric solutions with $\alpha = 1.43$, $Re = 1400$ ($Re_b = 461$). Black (dark grey) represents +70% (-70%) of the maximum vorticity and light grey represents 40% of the maximum velocity. The flow is from bottom to top.

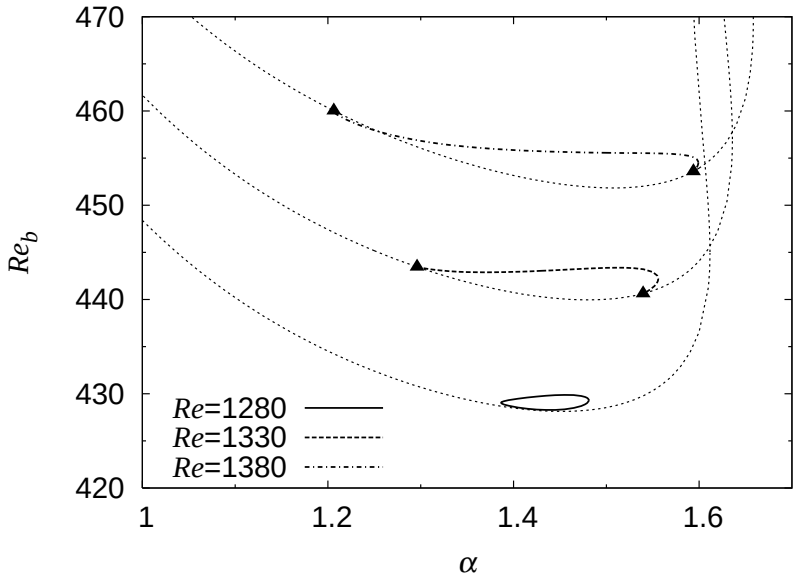

Figure 3.16: The existence domains of the $\mathbf{\Omega}$-symmetric solutions. Solid curve: $Re = 1280$. Dashed curve: $Re = 1330$. Dash-and-dotted curve: $Re = 1380$. The thin dotted curves indicate ONWB at $Re = 1280, 1330$ and 1380. The closed triangles represent the bifurcation points on the upper branches of ONWB.

unstable direction, while ONWB has five. The eigenvalues of the **S**-symmetric solution are smaller than those of ONWB. These results imply that the **S**-symmetric solution is more likely to appear in the laminar-turbulent boundary than ONWB. The **Ω**-symmetric solution is slightly deviated from ONWB. The solution in pipe flow, which corresponds to our **Ω**-symmetric solution, has not been reported yet. However, it is probable that such a solution will be found through the stability analysis of the mirror-symmetric solution by Pringle & Kerwsell (2007).

Our stability analysis exhibits that many solutions could emerge far below the transitional Reynolds number, $Re_b \sim 1000$, via symmetry breaking bifurcations (mainly from the upper branch), showing the richness of the nonlinear solutions due to the symmetry breaking and the complexity of phase space in the transitional regime. Solutions which bifurcate from neutral points with the complex eigenvalue are not considered here. These solutions are expected to be time-periodic in the frame of reference moving with a constant speed (relative periodic orbit). They might be captured numerically by using a time stepping code.

3.4 Appendix

3.4.1 Accuracy of the asymmetric travelling waves

The numerical accuracy of the asymmetric travelling waves is checked in table 3.3 and 3.4. The phase velocity, the bulk Reynolds number and the skin friction are listed as a function of the truncation level. We regard the **S**-symmetric solution with $(L, M, N) = (6, 33, 33)$ and **Ω**-symmetric solution with $(L, M, N) = (7, 37, 37)$ as converged. At least three digits agree for the characteristic quantities with the dashed underline in the tables.

Table 3.3: The phase velocity c, the bulk Reynolds number Re_b and the skin friction λ for the **S**-symmetric solution with $\alpha = 0.70$ at $Re = 3000$ as a function of the truncation level (L, M, N).

(L, M, N)	c	Re_b	λ
$(4, 33, 33)$	2207.1	1342.0	0.02261
$(6, 31, 31)$	2213.9	1342.1	0.02261
$(6, 33, 33)$	2207.2	1342.0	0.02261
$(6, 35, 35)$	2207.9	1341.5	0.02263
$(8, 33, 33)$	2207.2	1342.0	0.02261

Table 3.4: Same as table 3.3 for the **Ω**-symmetric solution with $\alpha = 1.43$ at $Re = 1400$.

(L, M, N)	c	Re_b	λ
$(5, 37, 37)$	591.79	460.62	0.08957
$(7, 35, 35)$	592.00	460.89	0.08946
$(7, 37, 37)$	592.24	461.03	0.08941
$(7, 39, 39)$	592.22	461.03	0.08941
$(9, 37, 37)$	592.15	460.96	0.08943

Chapter 4

A Variety of Travelling Wave Solutions

A number of travelling wave solutions in a square duct are discovered by a homotopy approach using artificially arranged body forces, following Waleffe, *Phys. Rev. Lett.* **81**, 4140-4143 (1998). Some of them appear at much lower Reynolds number than the transitional regime to turbulence, $Re_b \sim 1000$. It is found that most of the solutions presented in the thesis have their counterparts in pipe flow listed in Pringle *et al.*, *Phil. Trans. R. Soc.* A **367**, 457-472 (2009).

4.1 Continuation method using an artificial body force

In Chapter 2, we were successfully able to obtain the nonlinear solution in square duct flow, establishing the continuation from the internally heated flow to the isothermal flow. However, it is impossible to know beforehand whether the homotopy path using some parameter reaches the exact solution to the Navier-Stokes equations or not. For example, Barnes & Kerswell (2000) calculated the three-dimensional travelling wave solutions in rotating pipe flow. The attempt to find the nonlinear solution in pipe flow by reducing the rotation rate to zero failed. Waleffe (1998, 2003) calculated the exact solutions to plane Couette flow and plane Poiseuille flow by introducing an external body force, which creates the streamwise vortices. The streamwise vortices roll up the fluid in the vicinity of the wall, which is called the low-speed streak. The instability of the two-dimensional streaky flow leads to the subcritical bifurcation of the three-dimensional flow and the successful continuation to the exact solution to the Navier-Stokes equations without the external forcing. Following his approach, the method to calculate the nonlinear solutions in square duct

flow using an artificial body forces is described below.

The motion of the fluid is governed by the continuity equation,

$$\nabla \cdot \boldsymbol{u} = 0, \tag{4.1}$$

and the momentum equation

$$\partial_t \boldsymbol{u} + (\boldsymbol{u} \cdot \nabla)\boldsymbol{u} = -\nabla P + \nabla^2 \boldsymbol{u} + \boldsymbol{F}. \tag{4.2}$$

Here, $\boldsymbol{F}$ is an artificial body force, which depends on the coodinates in the cross section: $\boldsymbol{F} = (0, F_y(y,z), F_z(y,z))$. We impose the no-slip boundary condition,

$$\boldsymbol{u} = \boldsymbol{0} \quad \text{at} \quad y = \pm 1 \ \text{ and } \ z = \pm 1. \tag{4.3}$$

4.1.1 Laminar solution

We set $(u,v,w) = (U_B(y,z), V_B(y,z), W_B(y,z)), P = P_B = -\chi x$ as the laminar state. Substituting them into (4.2), we obtain

$$(V_B\partial_y + W_B\partial_z - \triangle_2)U_B = \chi, \tag{4.4}$$

$$(V_B\partial_y + W_B\partial_z - \triangle_2)V_B = F_y, \tag{4.5}$$

$$(V_B\partial_y + W_B\partial_z - \triangle_2)W_B = F_z. \tag{4.6}$$

We define the Reynolds number as follows,

$$Re = U_{B0}(0,0) = \frac{U_{B0*}(0,0)b_*}{\nu_*}, \tag{4.7}$$

where $U_{B0}(y,z)$ is the laminar flow without forcing (i.e. $U_{B0}(y,z)$ satisfies $-\triangle_2 U_{B0} = \chi$ and the no-slip boundary condition). The Reynolds number has the proportionality to the pressure gradient, $\chi = 3.3935Re$.

Note that V_B and W_B are separated from (4.4). As the continuity equation (4.1) leads to

$$\partial_y V_B + \partial_z W_B = 0, \tag{4.8}$$

we introduce the basic stream function in the cross section for the laminar flow:

$$V_B = \partial_z \varphi_B, \tag{4.9}$$

$$W_B = -\partial_y \varphi_B. \tag{4.10}$$

The equation for the stream function is obtained by $\partial_y(4.6) - \partial_z(4.5)$,

$$-(\partial_z\varphi_B\partial_y - \partial_y\varphi_B\partial_z - \triangle_2)\triangle_2\varphi_B = \partial_y F_z - \partial_z F_y \equiv \Omega_x. \tag{4.11}$$

An arbitrary motion in the cross section represented by φ_B is induced by applying the forcing, Ω_x defined in (4.11). Therefore, we initially give φ_B and solve (4.4) to obtain the laminar state. The stream function φ_B is expanded by the basis function, which satisfies the Dirichlet and Neumann conditions:

$$\varphi_B = \varepsilon \sum_{m=4}^{M} \sum_{n=4}^{N} \varphi_{Bmn} \phi_m(y) \phi_n(z), \tag{4.12}$$

where ϕ_m is given in (2.35). For instance,

$$\phi_5(y) = 16y(1-y^2)^2, \tag{4.13}$$

$$\phi_7(y) = 16y(1+4y^2)(1-y^2)^2. \tag{4.14}$$

The coefficients φ_{Bmn} are normalized as

$$\sum_{m=4}^{M} \sum_{n=4}^{N} |\varphi_{Bmn}| = 1. \tag{4.15}$$

We refer to the parameter ε as the strength of the roll. The typical choices of the basic stream function and the consequent laminar solutions are shown in figures 4.1 and 4.2. The four and eight-vortex state are produced by the artificial forcing in figure 4.1 and 4.2, respectively. These are the two dimensional flows.

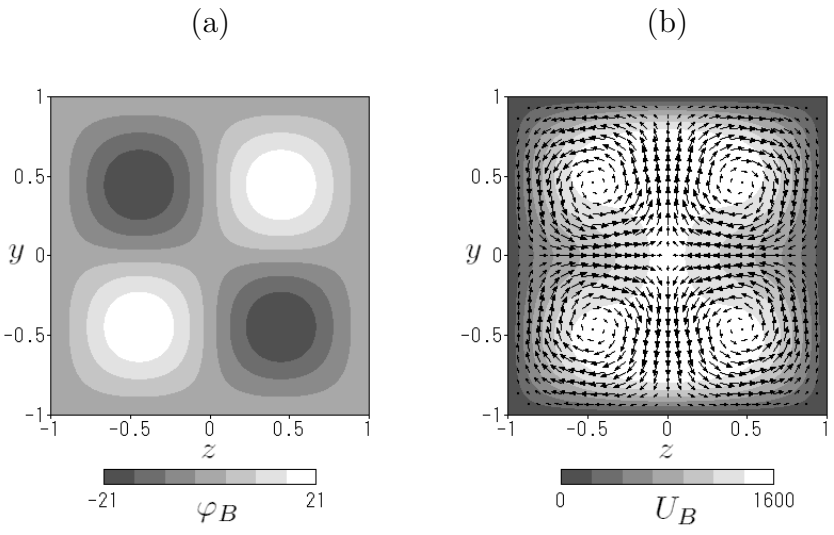

Figure 4.1: (a) The basic stream function $\varphi_B = \varepsilon\phi_5(y)\phi_5(z)$ with $\varepsilon = 1$ represented by the grey scale. (b) The laminar solution for $Re = 3000$ with $\varepsilon = 0.266$. The grey scale shows the streamwise velocity U_B.

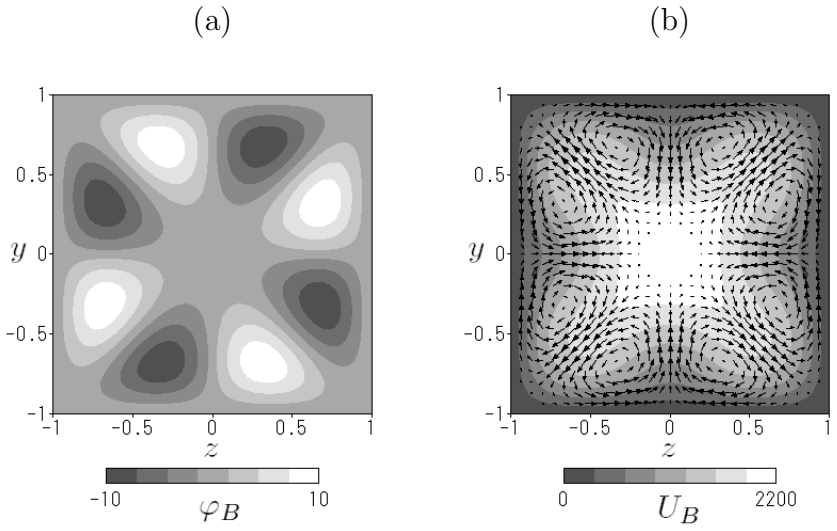

Figure 4.2: Same as figure 4.2. (a) $\varphi_B = \varepsilon\big(\phi_5(y)\phi_7(z) - \phi_7(y)\phi_5(z)\big)/2$ with $\varepsilon = 1$. (b) The laminar solution for $Re = 3000$ with $\varepsilon = 0.191$.

4.1.2 Linear stability analysis

The method to investigate the instability of the basic flow with the two-dimensional streamwise rolls is presented in this subsection. We superimpose perturbations, $\hat{\boldsymbol{u}}$ and $\hat{p}$, on the laminar state obtained by the last section, $\boldsymbol{U}_B = (U_B, V_B, W_B)$ and P_B:

$$\boldsymbol{u} = \boldsymbol{U}_B + \hat{\boldsymbol{u}}, \tag{4.16}$$

$$P = P_B + \hat{p}. \tag{4.17}$$

The perturbations are governed by the following equations,

$$\nabla \cdot \hat{\boldsymbol{u}} = 0, \tag{4.18}$$

$$\partial_t \hat{\boldsymbol{u}} + (\boldsymbol{U}_B \cdot \nabla)\hat{\boldsymbol{u}} + (\hat{\boldsymbol{u}} \cdot \nabla)\boldsymbol{U}_B + (\hat{\boldsymbol{u}} \cdot \nabla)\hat{\boldsymbol{u}} = -\nabla\hat{p} + \nabla^2\hat{\boldsymbol{u}}. \tag{4.19}$$

Neglecting the nonlinear terms in $\boldsymbol{e}_z \cdot \nabla\times$(4.19) and $\boldsymbol{e}_y \cdot \nabla\times$(4.19) leads to

$$\begin{aligned}
&\Big[\{\partial_t + (\boldsymbol{U}_B \cdot \nabla) - \nabla^2 + \partial_y V_B\}\partial_x - \partial_{yy}^2 U_B\Big]\hat{v} \\
&-\Big[\{\partial_t + (\boldsymbol{U}_B \cdot \nabla) - \nabla^2 + \partial_y V_B\}\partial_y + \partial_y W_B \partial_z\Big]\hat{u} \\
&\qquad + \Big(\partial_y U_B \partial_z - \partial_z U_B \partial_y - \partial_{yz}^2 U_B + \partial_z V_B \partial_x\Big)\hat{w} = 0,
\end{aligned} \tag{4.20}$$

$$\begin{aligned}
&\Big[\{\partial_t + (\boldsymbol{U}_B \cdot \nabla) - \nabla^2 + \partial_z W_B\}\partial_x - \partial_{zz}^2 U_B\Big]\hat{w} \\
&-\Big[\{\partial_t + (\boldsymbol{U}_B \cdot \nabla) - \nabla^2 + \partial_z W_B\}\partial_z + \partial_z V_B \partial_y\Big]\hat{u} \\
&\qquad + \Big(\partial_z U_B \partial_y - \partial_y U_B \partial_z - \partial_{yz}^2 U_B + \partial_y W_B \partial_x\Big)\hat{v} = 0.
\end{aligned} \tag{4.21}$$

We solve (4.18) for $\hat{u}$ to obtain

$$\hat{u} = -\partial_x^{-1}(\partial_y \hat{v} + \partial_z \hat{w}), \tag{4.22}$$

where ∂_x^{-1} is the integrating operator with respect to x. We give V_B and W_B by (4.9) and (4.10), and eliminate $\hat{u}$ using (4.22) in (4.20) and (4.21). The perturbations in the cross section, $\hat{v}$ and $\hat{w}$, are expanded in normal modes:

$$\begin{pmatrix} \hat{v} \\ \hat{w} \end{pmatrix}(x, y, z, t) = \begin{pmatrix} v_1(y, z) \\ w_1(y, z) \end{pmatrix} \exp[i\alpha(x - ct)]. \tag{4.23}$$

Here, the complex wave speed is expressed by c, whose imaginary part multiplied by the wavenumber α indicates the growth rate of the perturbations. After we expand v_1 and w_1 by the appropriate basis functions, which satisfy the boundary conditions, we substitute (4.23) into (4.20) and (4.21). The Galerkin projection leads to the generalized eigenvalue problem with the eigenvalue c.

4.1.3 Calculation of travelling waves

The three-dimensional solution, which bifurcates from the neutral point identified by the linear stability analysis, is calculated by the following procedure. We decompose perturbations, $\hat{\boldsymbol{u}}$ and $\hat{p}$, into the mean parts and the residuals.

$$\hat{\boldsymbol{u}}(x, y, z, t) = \hat{\boldsymbol{U}}(y, z, t) + \check{\boldsymbol{u}}(x, y, z, t), \tag{4.24}$$

$$\hat{p}(x, y, z, t) = \hat{P}(y, z, t) + \check{p}(x, y, z, t). \tag{4.25}$$

Note that $\nabla \hat{P} = 0$ because the pressure gradient is fixed. We define the mean flow, $\bar{\boldsymbol{U}} = (\bar{U}, \bar{V}, \bar{W}) = \int_0^{2\pi/\alpha} \boldsymbol{u}\, \mathrm{d}x$, and the mean deviation from the laminar flow without forcing, $\boldsymbol{U}' = (U', V', W') = \bar{\boldsymbol{U}} - U_{B0}\boldsymbol{e}_x$. Substituting (4.24) and (4.25) into (4.18) and (4.19) leads to

$$\partial_y V' + \partial_z W' + \nabla \cdot \check{\boldsymbol{u}} = 0, \tag{4.26}$$

$$\begin{aligned} \partial_t(\boldsymbol{U}' + \check{\boldsymbol{u}}) + (\boldsymbol{U}' \cdot \nabla)\bar{\boldsymbol{U}} + (\bar{\boldsymbol{U}} \cdot \nabla)\check{\boldsymbol{u}} + (\check{\boldsymbol{u}} \cdot \nabla)\bar{\boldsymbol{U}} + (\check{\boldsymbol{u}} \cdot \nabla)\check{\boldsymbol{u}} \\ = -\nabla\check{p} + \triangle_2 \boldsymbol{U}' + \nabla^2 \check{\boldsymbol{u}} + \boldsymbol{F}. \end{aligned} \tag{4.27}$$

Operations $\boldsymbol{e}_z \cdot \nabla\times$(4.27) and $\boldsymbol{e}_y \cdot \nabla\times$(4.27) lead to

$$\begin{aligned} &\Big[\{\partial_t + (\bar{\boldsymbol{U}} \cdot \nabla) - \nabla^2 + \partial_y V'\}\partial_x - \partial_{yy}^2 \bar{U}\Big]\check{v} \\ &-\Big[\{\partial_t + (\bar{\boldsymbol{U}} \cdot \nabla) - \nabla^2 + \partial_y V'\}\partial_y + \partial_y W' \partial_z\Big]\check{u} \\ &\qquad +\Big(\partial_y \bar{U}\partial_z - \partial_z \bar{U}\partial_y - \partial_{yz}^2 \bar{U} + \partial_z V'\partial_x\Big)\check{w} \\ &\qquad\quad -(\partial_t - \triangle_2)\partial_y U' - \partial_y(\boldsymbol{U}' \cdot \nabla)\bar{U} + \boldsymbol{e}_z \cdot \nabla \times \{(\check{\boldsymbol{u}} \cdot \nabla)\check{\boldsymbol{u}}\} = 0, \end{aligned} \tag{4.28}$$

$$\begin{aligned}
&\Big[\{\partial_t + (\bar{\boldsymbol{U}}\cdot\nabla) - \nabla^2 + \partial_z W'\}\partial_x - \partial_{zz}^2\bar{U}\Big]\check{w} \\
-&\Big[\{\partial_t + (\bar{\boldsymbol{U}}\cdot\nabla) - \nabla^2 + \partial_z W'\}\partial_z + \partial_z V'\partial_y\Big]\check{u} \\
&\quad +\Big(\partial_z\bar{U}\partial_y - \partial_y\bar{U}\partial_z - \partial_{yz}^2\bar{U} + \partial_y W'\partial_x\Big)\check{v} \\
&\quad -(\partial_t - \triangle_2)\partial_z U' - \partial_z(\boldsymbol{U}'\cdot\nabla)\bar{U} - \boldsymbol{e}_y\cdot\nabla\times\{(\check{\boldsymbol{u}}\cdot\nabla)\check{\boldsymbol{u}}\} = 0.
\end{aligned} \tag{4.29}$$

We take the streamwise average of (4.26) to obtain

$$\partial_y V' + \partial_z W' = 0. \tag{4.30}$$

Then, the stream function in the cross section, φ' is introduced as follows:

$$V' = \partial_z\varphi', \tag{4.31}$$

$$W' = -\partial_y\varphi'. \tag{4.32}$$

Operation on the streamwise average of $\boldsymbol{e}_x\cdot$(4.27) and $\boldsymbol{e}_x\cdot\nabla\times$(4.27) leads to

$$\partial_t U' + (\partial_z\varphi'\partial_y - \partial_y\varphi'\partial_z)\bar{U} - \triangle_2 U' + \partial_y\overline{\check{u}\check{v}} + \partial_z\overline{\check{u}\check{w}} = 0, \tag{4.33}$$

$$-(\partial_t + \partial_z\varphi'\partial_y - \partial_y\varphi'\partial_z - \triangle_2)\triangle_2\varphi' + (\partial_{yy}^2 - \partial_{zz}^2)\overline{\check{v}\check{w}} + \partial_{yz}^2\overline{\check{w}^2 - \check{v}^2} = \Omega_x, \tag{4.34}$$

where the overline means the streamwise average: $\overline{\cdot} \equiv \alpha/(2\pi)\int_0^{2\pi/\alpha}\cdot\,\mathrm{d}x$. Subtracting (4.30) from (4.26) and solving for $\check{u}$, we obtain

$$\check{u} = -\partial_x^{-1}(\partial_y\check{v} + \partial_z\check{w}). \tag{4.35}$$

The boundary condition for the variables are

$$\check{v} = \check{w} = \partial_y\check{v} = U' = \varphi' = \partial_y\varphi' = \partial_z\varphi' = 0 \quad \text{at} \quad y = \pm 1, \tag{4.36}$$

$$\check{v} = \check{w} = \partial_z\check{w} = U' = \varphi' = \partial_y\varphi' = \partial_z\varphi' = 0 \quad \text{at} \quad z = \pm 1. \tag{4.37}$$

We assume a travelling wave as a nonlinear solution. The residual $\check{v}, \check{w}$ are expanded by Fourier series in the streamwise direction as follows:

$$\begin{pmatrix}\check{v}\\ \check{w}\end{pmatrix}(x,y,z,t) = \sum_{\substack{l=-L\\ l\neq 0}}^{L}\begin{pmatrix}v_l(y,z)\\ w_l(y,z)\end{pmatrix}\exp[il\alpha(x-ct)]. \tag{4.38}$$

All the variables are expanded by the basis functions ϕ_m and ψ_n in the cross section,

$$\begin{pmatrix}v_l\\ w_l\\ U'\\ \varphi'\end{pmatrix} = \sum_{m=2}^{M}\sum_{n=2}^{N}\begin{pmatrix}v_{lmn}\phi_m(y)\psi_n(z)\\ w_{lmn}\psi_m(y)\phi_n(z)\\ U_{mn}\psi_m(y)\psi_n(z)\\ \varphi_{mn}\phi_m(y)\phi_n(z)\end{pmatrix}. \tag{4.39}$$

In order to fix the phase of the travelling wave, we set

$$\Im[v_{252}] = 0. \tag{4.40}$$

Eliminating V', W' and $\check{u}$ by (4.31), (4.32) and (4.35) in (4.28), (4.29), (4.33), (4.34) and (4.40), the Galerkin projection onto the appropriate basis leads to the quadratic equation:

$$A_{ij}x_j + B_{ijk}x_jx_k = 0,\ x_j = (v_{lmn}, w_{lmn}, U_{mn}, \varphi_{mn}, c)^T. \tag{4.41}$$

This algebraic equation is solved by the Newton-Raphson iteration. As the initial guess of the Newton iteration, we choose the eigenfunction near the neutral point. In order to measure the nonlinearity (or three-dimensionality) of the solutions, we define the energy of the fluctuating part of the disturbance as

$$E_{3D} = \frac{\alpha}{8\pi}\int_0^{2\pi/\alpha}\int_{-1}^{+1}\int_{-1}^{+1}\frac{|\check{\boldsymbol{u}}|^2}{2}\mathrm{d}x\mathrm{d}y\mathrm{d}z. \tag{4.42}$$

4.2 Result

We have calculated nine travelling wave solutions by the method described in the previous section. Three of them have already been reported (Wedin *et al.* 2009; Uhlmann *et al.* 2010; Okino *et al.* 2010). Other six are new solutions. We have imposed one of the symmetries I, II and III shown by (2.43)–(2.45) and (2.47) to the solutions. Hence, the bifurcating solutions, which have been presented in Chapter 3, are not reproduced here. All the travelling wave solutions we have obtained are listed in table 4.1 with their minimum bulk Reynolds number and minimum Reynolds number. Figures 4.3 and 4.4 show the skin frictions and the existence domains for some solutions. The wavenumbers of the solutions are chosen to minimize their bulk Reynolds number for figure 4.3. Figure 4.4 shows that the solutions, which appear far below the transitional Reynolds number ($Re_b \sim 1000$), take their minimum Reynolds number when their wavenumber is almost equal to one (see also table 4.1).

Table 4.1: Travelling wave solutions in square duct flow with their minimum values of the bulk Reynolds number and the Reynold number.

Solution	$\min Re_b(Re, \alpha)$	$\min Re(\alpha)$
$\nu 1$ (WBN)	598 $(Re = 1968, \alpha = 0.85)$	1952 $(\alpha = 0.87)$
$\mu 1$ (ONWB)	332 $(Re = 836, \alpha = 1.14)$	828 $(\alpha = 1.13)$
$\nu 2$ (UKP)	455 $(Re = 1579, \alpha = 0.90)$	1535 $(\alpha = 0.88)$
$\sigma 2$	498 $(Re = 1627, \alpha = 1.10)$	1607 $(\alpha = 1.08)$
$\sigma 4$a	1081 $(Re = 4308, \alpha = 3.06)$	4287 $(\alpha = 3.11)$
$\sigma 4$b	1011 $(Re = 2726, \alpha = 3.20)$	2714 $(\alpha = 3.12)$
$\mu 2$	903 $(Re = 3285, \alpha = 2.35)$	3138 $(\alpha = 2.27)$
$\zeta 2$	624 $(Re = 2313, \alpha = 1.20)$	2179 $(\alpha = 1.16)$
$\delta 2$	670 $(Re = 2225, \alpha = 1.32)$	2187 $(\alpha = 1.21)$
$\sigma 1$ (**S**-symmetric)	365 $(Re = 952, \alpha = 1.38)$	924 $(\alpha = 1.36)$
$\omega 1$ (**Ω**-symmetric)	427 $(Re = 1272, \alpha = 1.43)$	1271 $(\alpha = 1.43)$

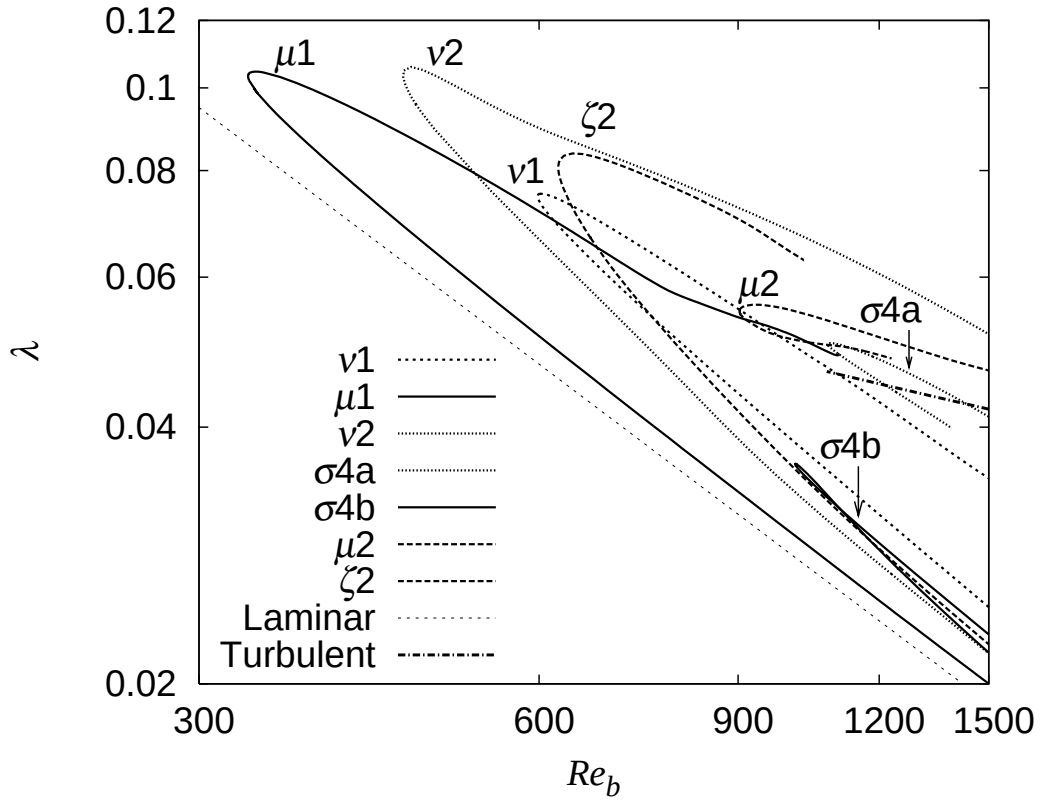

Figure 4.3: The skin friction λ against the bulk Reynolds number for the travelling waves in square duct flow. The laminar state is represented by $\lambda = 28.45/Re_b$. The turbulent state obeys the empirical formula by Jones (1976): $\lambda^{-1/2} = 2\log_{10}(2.25 Re_b \lambda^{1/2}) - 0.8$.

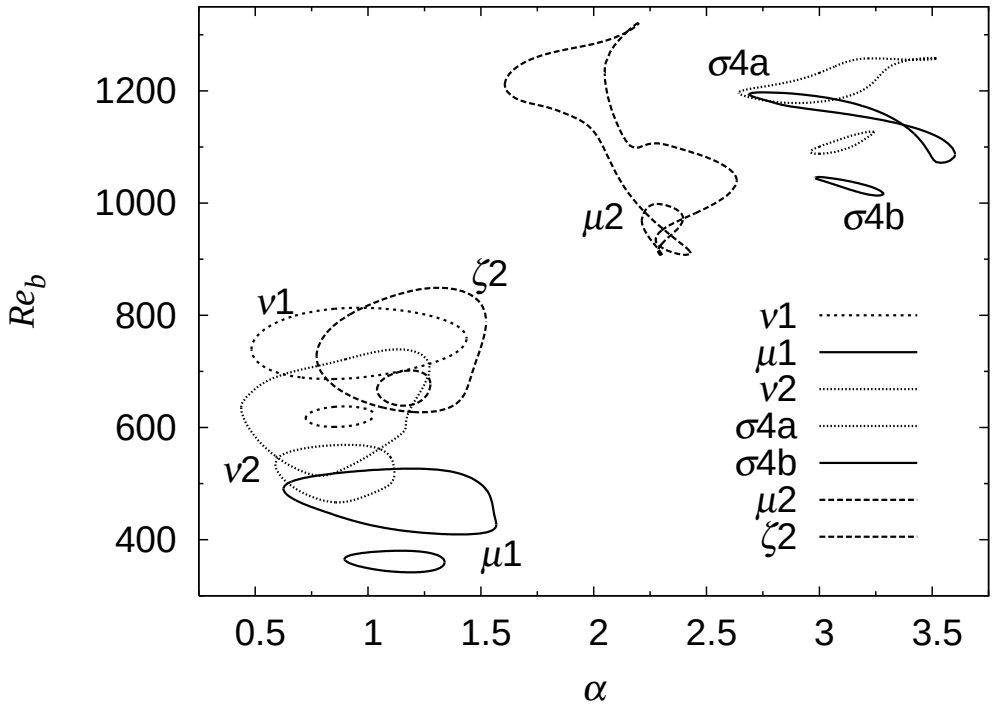

Figure 4.4: The existence domains of the travelling wave solutions. The Reynolds numbers of the solutions are 2000 and 2400 for $\nu 1$, 900 and 1200 for $\mu 1$, 1700 and 2000 for $\nu 2$, 4400 and 5000 for $\sigma 4$a, 2750 and 3000 for $\sigma 4$b, 3200 and 3400 for $\mu 2$, 2200 and 2400 for $\zeta 2$. The domains become larger as the Reynolds number increases.

4.2.1 Symmetry I

We obtain the travelling waves, WBN and ONWB, by choosing the streamwise function as $\varphi_B = \varepsilon\phi_5(y)\phi_5(z)$ and $\varphi_B = \varepsilon(\phi_5(y)\phi_7(z) - \phi_7(y)\phi_5(z))/2$ (see figures 4.1 and 4.2), and rename them $\nu 1$ and $\mu 1$, respectively, in order to link the nomenclature of the solutions, N1 and M1, in pipe flow by Pringle *et al.* (2009). For instance, taking $\varphi_B = \varepsilon\phi_5(y)\phi_5(z)$, the growth rate of the perturbations with $\alpha = 0.85$ at $Re = 2500$ as a function of the strength of the roll, ε, is shown in figure 4.5(a). The neutral point is found at $\varepsilon \sim 0.285$. Figure 4.5(b) show the energy of the fluctuating part of the disturbance against ε as a bifurcation diagram. The solution bifurcates subcritically from the critical point at $\varepsilon = 0.285$ (shown by the closed circle) and cross the line, $\varepsilon = 0$. This intersection (open circle) represents the solution to the Navier-Stokes equations without any artificial body force. The solution curve continues to decrease until it undergoes the turning point at $\varepsilon = -0.275$ and crosses zero again. This is

how we calculate the solution $\nu 1$ (WBN). The velocity field of the lower branch of $\nu 1$ is shown in figure 4.6. The similarity between $\nu 1$ and N1 is mentioned in Wedin *et al.* (2009) (see also figure 4.7). We find the minimum bulk Reynolds number of $\mu 1$ is lower than those of any other solutions we have obtained (see table 4.1 and figure 4.3).

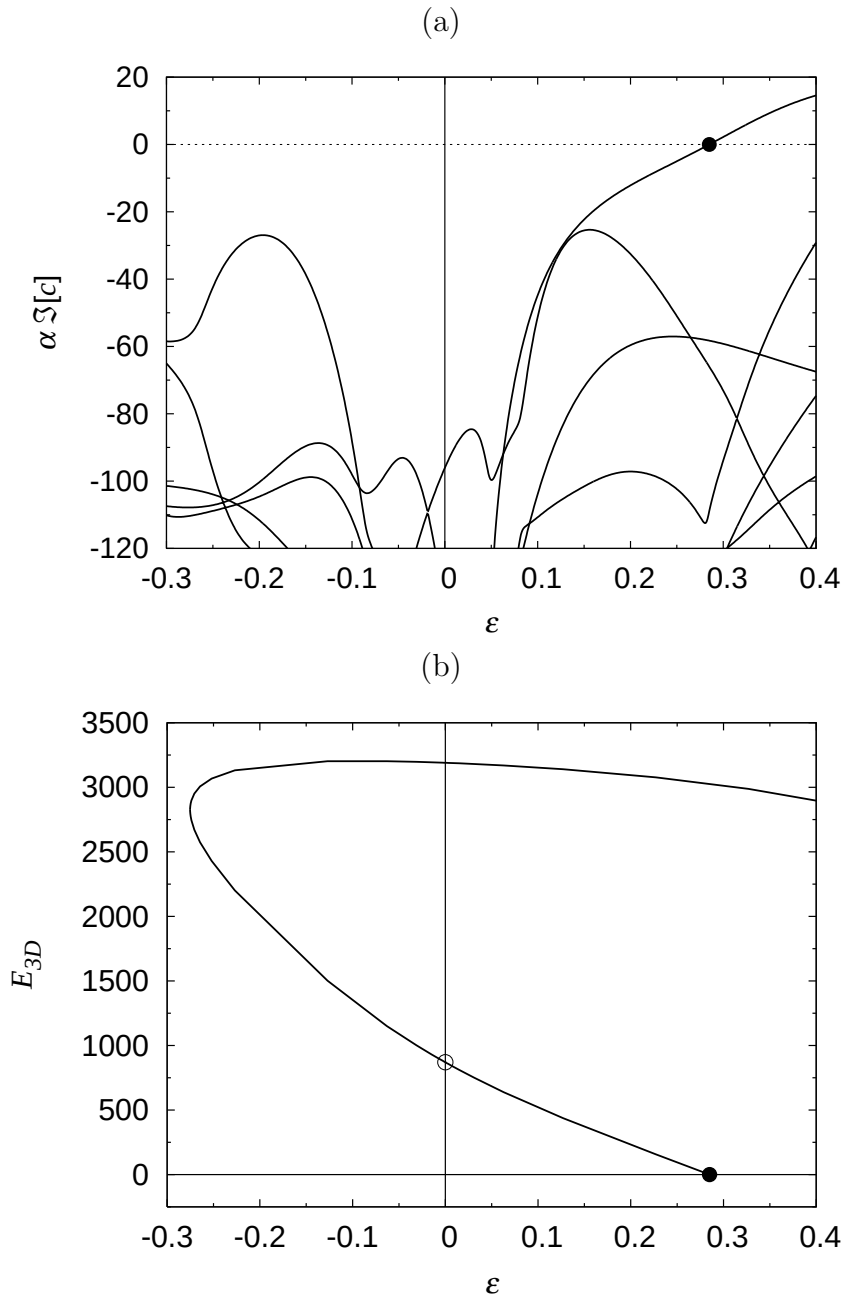

Figure 4.5: (a) The growth rate of the perturbations, $\alpha\Im[c]$, with $\alpha = 0.85$ at $Re = 2500$. (b) The bifurcation diagram of the solution $\nu 1$ with $\alpha = 0.85$ at $Re = 2500$. The bifurcation point is indicated by the closed circle.

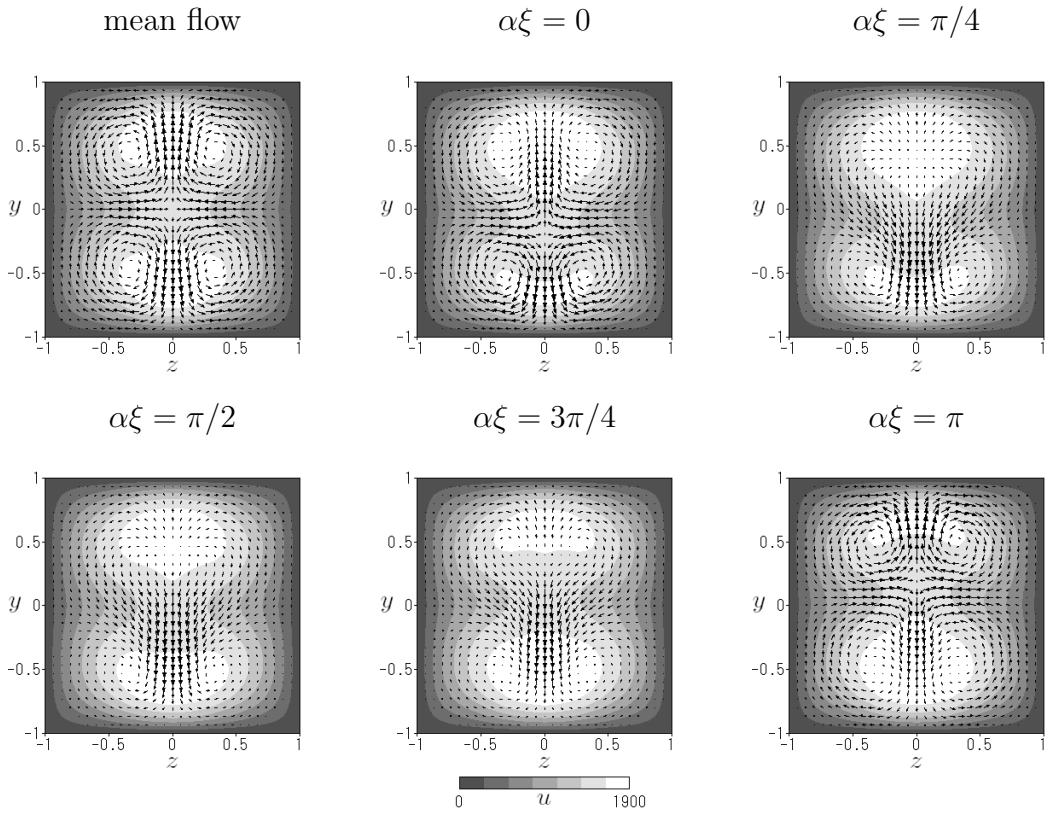

Figure 4.6: Mean flow $\bar{\boldsymbol{U}}$ (top-left) and images of the total flows $\boldsymbol{u}$ along ξ of the lower branch solution of $\nu 1$ with $\alpha = 0.85$ at $Re = 3000$ ($Re_b = 1056$). The velocity components are shown on the y-z plane (arrows) and along the x-direction (grey scale). $\xi = x - ct$.

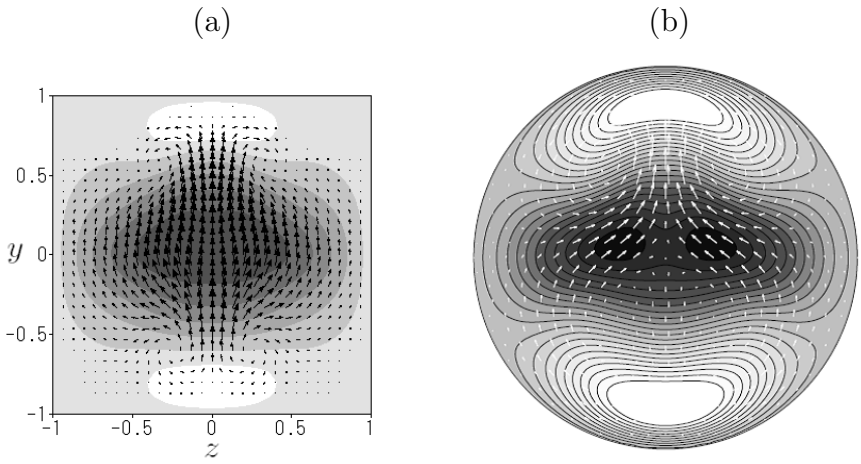

Figure 4.7: The instantaneous disturbance velocity field for (a) $\nu 1$ with $\alpha = 0.85$ and $Re = 3000$ ($Re_b = 1056$) (b) N1 (figure 5b in Pringle *et al.* 2009). The streamwise component is shown by grey scale. Grey and white represent slow and fast region, respectively.

4.2.2 Symmetry II

The nonlinear solutions with the symmetry II represented by (2.44) and (2.47) are invariant under the following transformations: the shift by half the wavelength in the streamwise direction and reflection with respect to y,

$$\mathbf{S}: \begin{pmatrix} u \\ v \\ w \end{pmatrix} (\xi, y, z) \to \begin{pmatrix} u \\ -v \\ w \end{pmatrix} (\xi + \frac{\pi}{\alpha}, -y, z),$$

the rotation by 180 degrees in the cross section,

$$\mathbf{R}_2: \begin{pmatrix} u \\ v \\ w \end{pmatrix} (\xi, y, z) \to \begin{pmatrix} u \\ -v \\ -w \end{pmatrix} (\xi, -y, -z). \tag{4.43}$$

The combination of $\mathbf{S}$ and $\mathbf{R}_2$ shows the shift by half the wavelength in the streamwise direction and reflection with respect to z:

$$\mathbf{S}': \begin{pmatrix} u \\ v \\ w \end{pmatrix} (\xi, y, z) \to \begin{pmatrix} u \\ v \\ -w \end{pmatrix} (\xi + \frac{\pi}{\alpha}, y, -z). \tag{4.44}$$

The schematic expression of the flow with the symmetry II in the cross section is presented in figure 4.8.

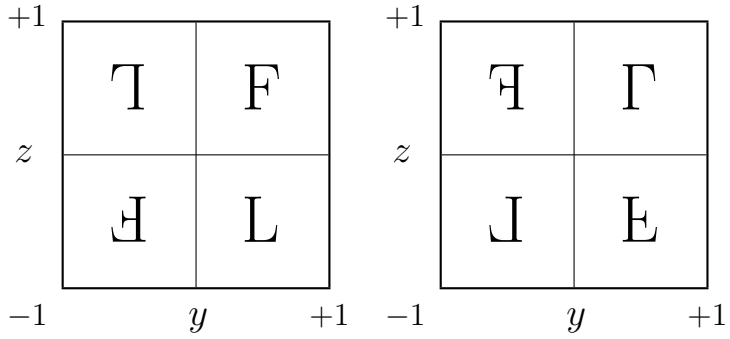

Figure 4.8: The schematic flow pattern with the symmetry II in the cross section at (left) $\xi = \xi_0$ and (right) $\xi = \xi_0 + \pi/\alpha$, where ξ_0 is an arbitrary constant. The letters "F" and "L" show some different flow patterns in the cross section.

Choosing the basic stream function $\varphi_B = \varepsilon(\phi_5(y)\phi_7(z) - \phi_7(y)\phi_5(z))/2$, we have reproduced the solution by Uhlmann *et al.* (2010), which is referred to as

$\nu 2$ hereafter. Examining the coefficient vector, it is found that the solution $\nu 2$ has the additional symmetry. The coefficients of $\nu 2$ have the following relation:

$$\begin{cases} v_{lmn} = w_{lnm}, \\ U_{mn} = U_{nm}, \\ \varphi_{mn} = -\varphi_{nm}. \end{cases} \tag{4.45}$$

It is easily verified that this inherent symmetry means the diagonal symmetry,

$$\mathbf{D} : \begin{pmatrix} u \\ v \\ w \end{pmatrix} (\xi, y, z) \rightarrow \begin{pmatrix} u \\ w \\ v \end{pmatrix} (\xi, z, y). \tag{4.46}$$

For example,

$$\begin{aligned} v(\xi, y, z) =& V'(y, z) + \check{v}(\xi, y, z) \\ =& \partial_z \varphi'(y, z) + \check{v}(\xi, y, z) \\ =& \sum_{m,n} \varphi_{mn} \phi_m(y) \phi'_n(z) + \sum_{l,m,n} v_{lmn} \phi_m(y) \psi_n(z) \exp[il\alpha\xi] \\ =& \sum_{m,n} -\varphi_{nm} \phi_m(y) \phi'_n(z) + \sum_{l,m,n} w_{lnm} \phi_m(y) \psi_n(z) \exp[il\alpha\xi] \\ =& \sum_{m,n} -\varphi_{mn} \phi'_m(z) \phi_n(y) + \sum_{l,m,n} w_{lmn} \psi_m(z) \phi_n(y) \exp[il\alpha\xi] \\ =& -\partial_y \varphi'(z, y) + \check{w}(\xi, z, y) \\ =& W'(z, y) + \check{w}(\xi, z, y) = w(\xi, z, y), \end{aligned}$$

where the prime in the 4th–6th lines indicates the derivative. The flow field of $\nu 2$ is shown in figure 4.9. As mentioned in Uhlmann *et al.* (2010), the mean flow shows the diagonally symmetric eight-vortex structure, which is consistent with the mean flow of the fully developed turbulence in square duct flow. It is clearly seen that the vortex pattern and the position of the low-speed streak of $\nu 2$ are very similar to those of N2 in pipe flow (see figure 4.10).

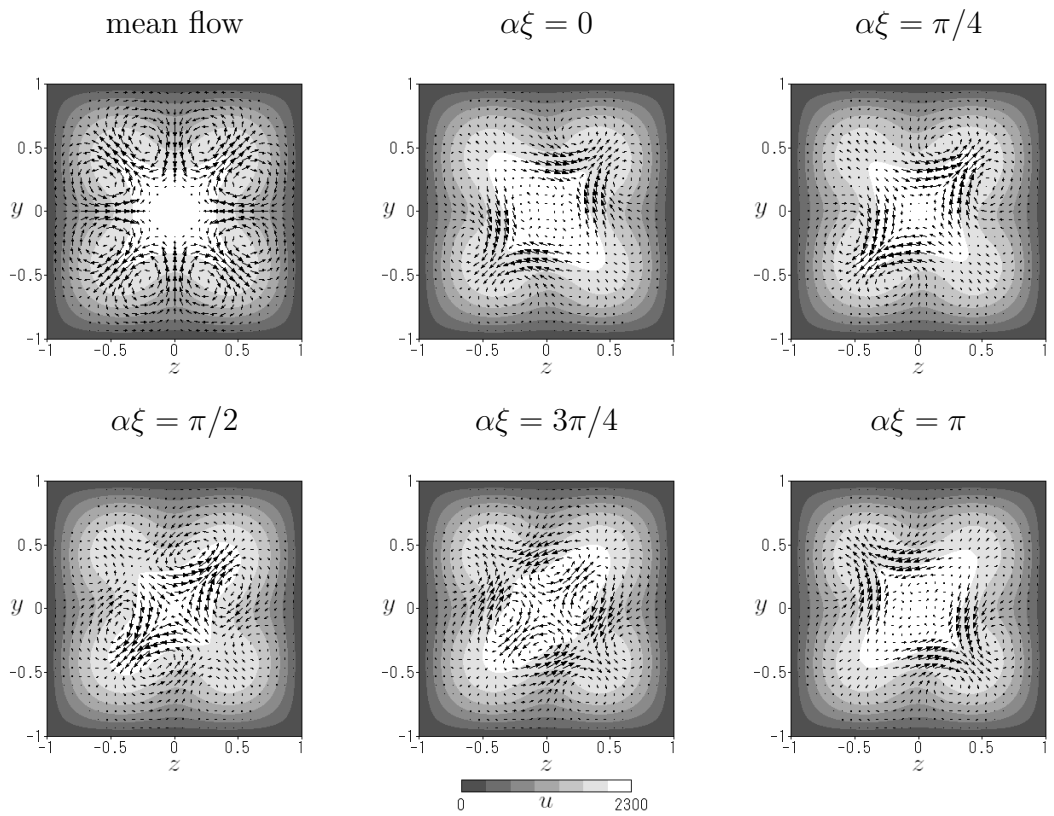

Figure 4.9: Same as figure 4.6 for $\nu 2$ with $\alpha = 0.9$ at $Re = 3000$ ($Re_b = 1230$).

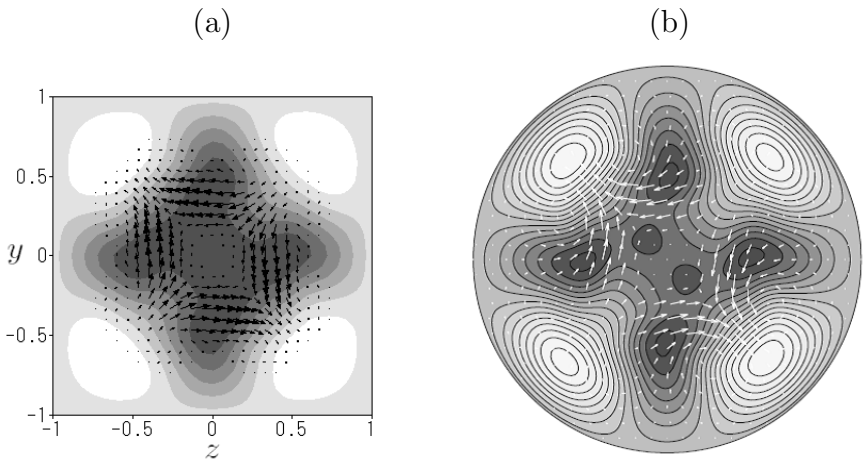

Figure 4.10: Same as figure 4.7 for (a) $\nu 2$ with $\alpha = 0.9$ at $Re = 3000$ ($Re_b = 1230$) and (b) N2 (figure 1b of Pringle *et al.* 2009).

σ2

We apply the forcing to induce the motion in the cross section represented by the stream function, $\varphi_B = \varepsilon\phi_5(y)\phi_5(z)$. Figure 4.11 shows (a) the growth rate of the perturbations and (b) the bifurcation diagram of the three dimensional solution with $\alpha = 2.0$ at $Re = 2750$. The neutral point of the first eigenvalue ($\varepsilon = 0.157$) is indicated by the closed circle in figure 4.11(a). The three dimensional solution, which bifurcates subcritically from the critical point at $\varepsilon = 0.1568$ (the closed circle in figure 4.11b), cross $\varepsilon = 0$ (open circle). The solution curve has the turning point at $\varepsilon = -0.0134$, and intersects $\varepsilon = 0$ again. We refer to the two solutions found here as σ2. The solution, which takes smaller value of E_{3D}, is on the lower branch of σ2 and the other is on the upper branch solution: these two solutions connect with each other when the Reynolds number is decreased. The velocity field of σ2 is shown in figure 4.12. The mean flow has the four-vortex structure (see the top-left of figure 4.12). The solution has two pairs of streamwise vortices, oscillating along the side walls alternately. This pattern is very similar to that of the solution S2 in pipe flow (see figure 4.13).

Figure 4.14 shows the existence domains of ν2 and σ2. We find that the solution σ2 bifurcates from ν2 by breaking the symmetry **D** (the bifurcation points are indicated by the circles). The bifurcation is the pitchfork type: two different solutions, which are identical under the rotation by 90 degrees in the cross section, appear at the same time. The solution also emerges through the saddle-node bifurcation at $\alpha \sim 1.15$, $Re_b \sim 675$ (see the closed-loop at the middle of figure 4.14).

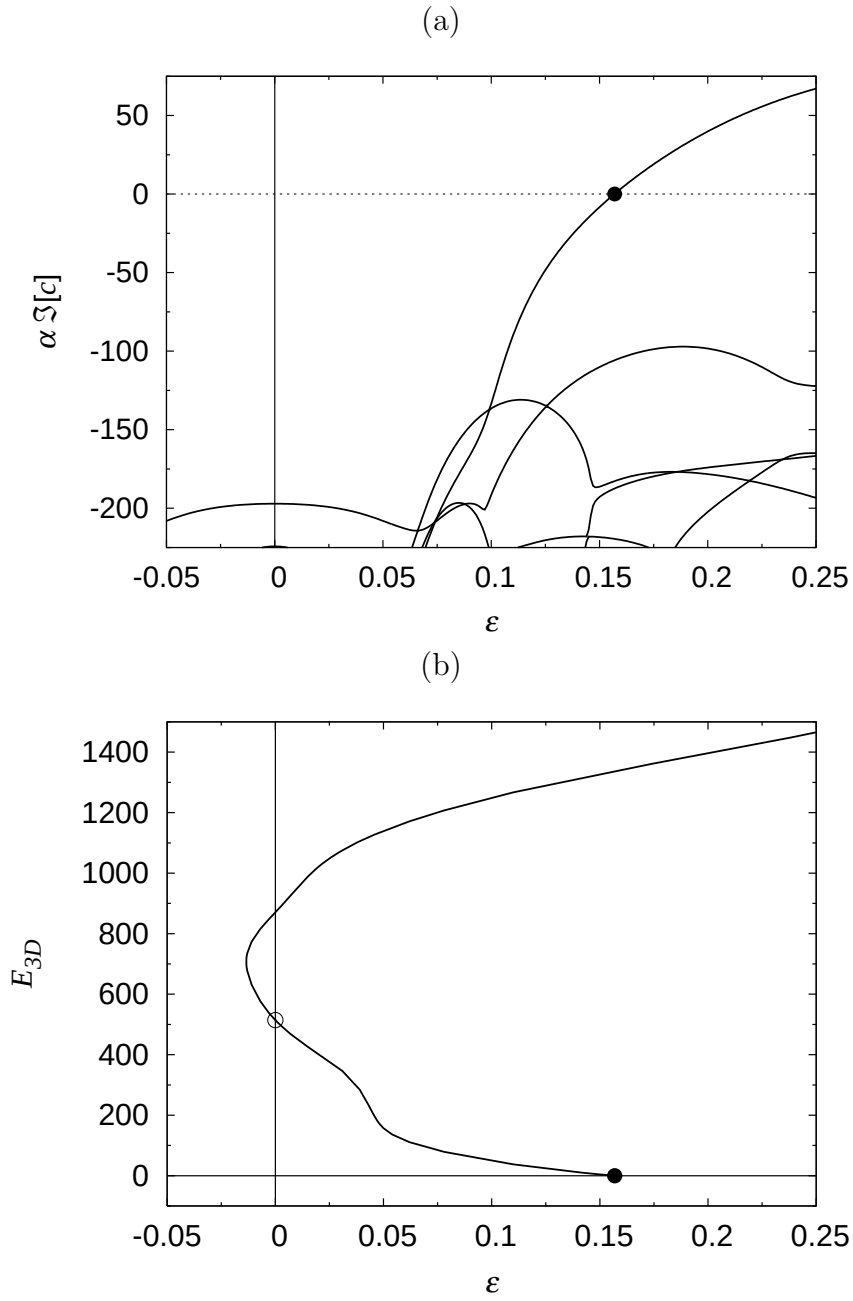

Figure 4.11: (a) The growth rate of the perturbations, $\alpha\Im[c]$, with $\alpha = 2.0$ at $Re = 2750$. (b) The bifurcation diagram of the solution $\sigma 2$ with $\alpha = 2.0$ at $Re = 2750$. The bifurcation point is indicated by the closed circle.

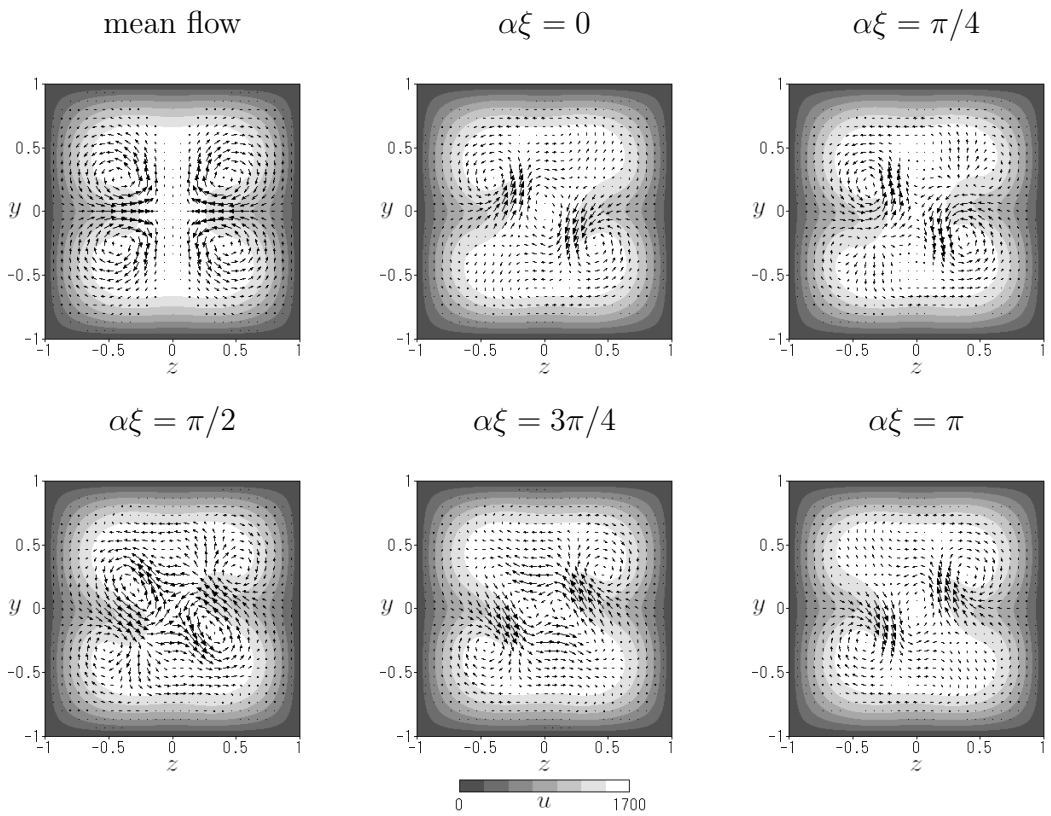

Figure 4.12: Mean flow $\bar{\boldsymbol{U}}$ (top-left) and images of the total flows $\boldsymbol{u}$ along ξ of $\sigma 2$ with $\alpha = 2.0$ at $Re = 2750$ ($Re_b = 1053$).

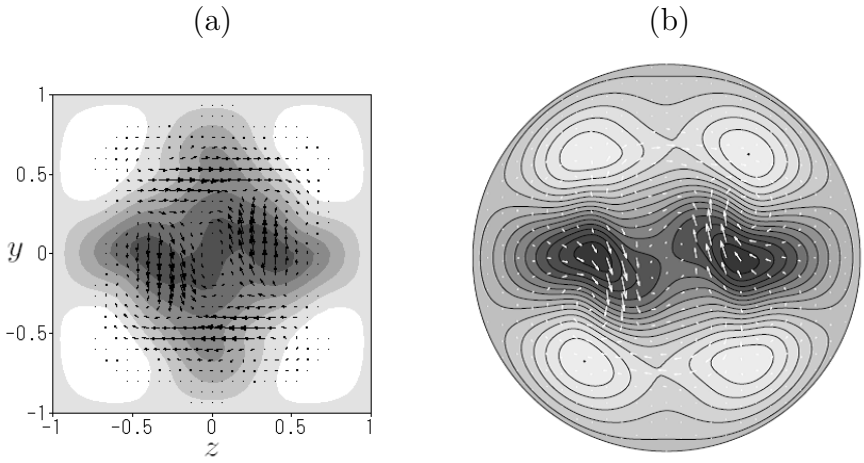

Figure 4.13: Same as figure 4.7 for (a) $\sigma 2$ with $\alpha = 1.1$ at $Re = 2500$ ($Re_b = 1010$) and S2 (figure 5d in Pringle *et al.* 2009, rotated by 90 degrees).

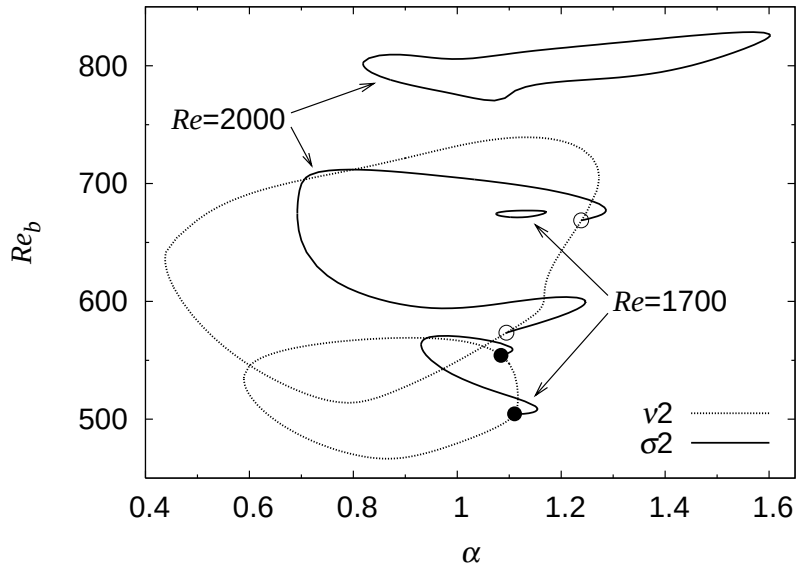

Figure 4.14: The existence domains of the solutions $\nu 2$ and $\sigma 2$ for $Re = 1700$ and 2000. Dotted curve: $\nu 2$. Solid curve: $\sigma 2$. The bifurcation points of $\sigma 2$ at $Re = 1700$ and 2000 are indicated by the closed and open circles, respectively.

σ4

We choose the artificial rolls as $\varphi_B = \varepsilon(\phi_5(y)\phi_7(z) - \phi_7(y)\phi_5(z))/2$. In this case, the opposite sign of ε results in the different solutions. Figure 4.15(a) shows the growth rate with $\alpha = 3.2$ at $Re = 5000$. The basic flow becomes unstable when $\varepsilon \sim 0.30$. The bifurcating solution from the neutral point is calculated (the solid curve in figure 4.15). Though the bifurcation is subcritical, the solution undergoes the turning point at $\varepsilon = 0.037$. The solution passes the other two turning points at $\varepsilon = 2.242, -0.334$ and intersect with $\varepsilon = 0$ twice. The lower branch solution is indicated by the open circle. We refer to the solutions obtained here as σ4a. The other neutral point is found at $\varepsilon \sim -0.29$ (see the closed diamond in figure 4.15a). The bifurcation curve, which subcritically starts from $\varepsilon = -0.287$, reaches the exact solution in square duct flow represented by the intersection with the line $\varepsilon = 0$ (see the open diamond in figure 4.15b). After passing through the turning point at $\varepsilon = 0.036$, it crosses zero again. These solutions are labelled as σ4b. Figures 4.16 and 4.17 present the velocity fields of σ4a and σ4b, respectively. Note that the

solutions has the rotational symmetry by 90 degrees,

$$\mathbf{R}_4 : \begin{pmatrix} u \\ v \\ w \end{pmatrix} (\xi, y, z) \to \begin{pmatrix} u \\ w \\ -v \end{pmatrix} (\xi, -z, y). \tag{4.47}$$

This symmetry is derived from the imposed symmetries (2.44), (2.47) and the inherent relation of the coefficients of the solution shown below:

$$\begin{cases} v_{lmn} = (-1)^l w_{lnm}, \\ U_{mn} = U_{nm}, \\ \varphi_{mn} = -\varphi_{nm}. \end{cases} \tag{4.48}$$

The mean flows for both solutions have the diagonally symmetric 16-vortex patterns (two major vortices near the wall and two minor vortices around the center in each quadrant). For σ4a, each pair of vortices oscillates along the boundary, producing the low-speed streak about the centre of the side (see figure 4.16), while the low-speed streaks are located at the corners of the square for σ4b. The motion of σ4a is essentially same as σ4b if it is rotated by 45 degrees. It is verified that the motions of σ4a and σ4b resemble that of S4 in pipe flow (the instantaneous flow of S4 is not presented in any documents. The movies of the travelling waves in pipe flow are available at `http://rsta.royalsocietypublishing.org/content/367/1888/457/suppl/DC1`). It should be noted that σ4a appears at much higher Reynolds number than σ4b, while their minimum bulk Reynolds numbers are almost the same (see table 4.1). Their minimum bulk Reynolds number is close to the transitional Reynolds number. Also, σ4a takes a higher value of the skin friction than σ4b and resides around the turbulent statistic by Jones (1976) (see figure 4.3).

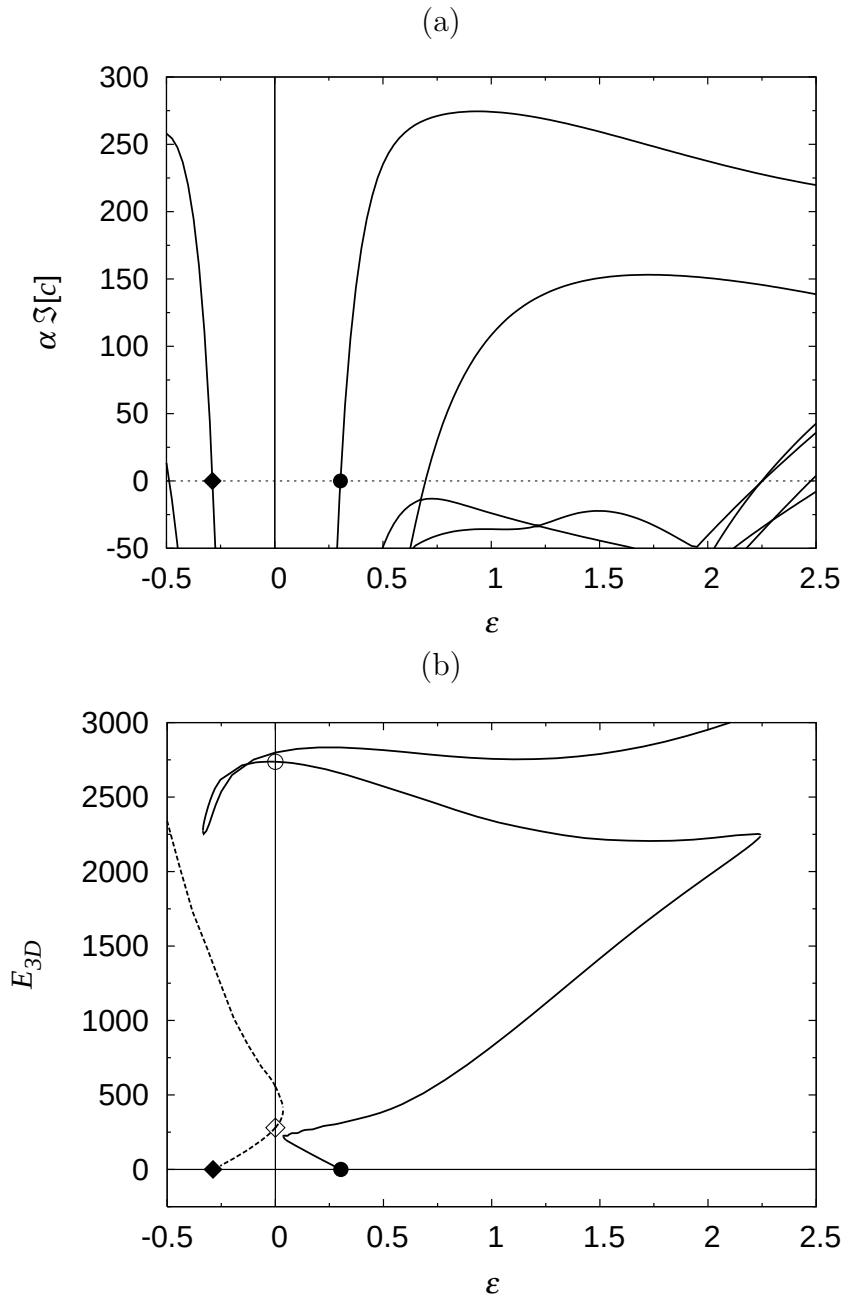

Figure 4.15: (a) The growth rate of the perturbations, $\alpha\Im[c]$, with $\alpha = 3.2$ at $Re = 5000$. (b) The bifurcation diagram of the solution σ4a (solid curve) and σ4b (dashed curve) with $\alpha = 3.2$ at $Re = 5000$. The bifurcation points are indicated by the closed circle and the closed triangle.

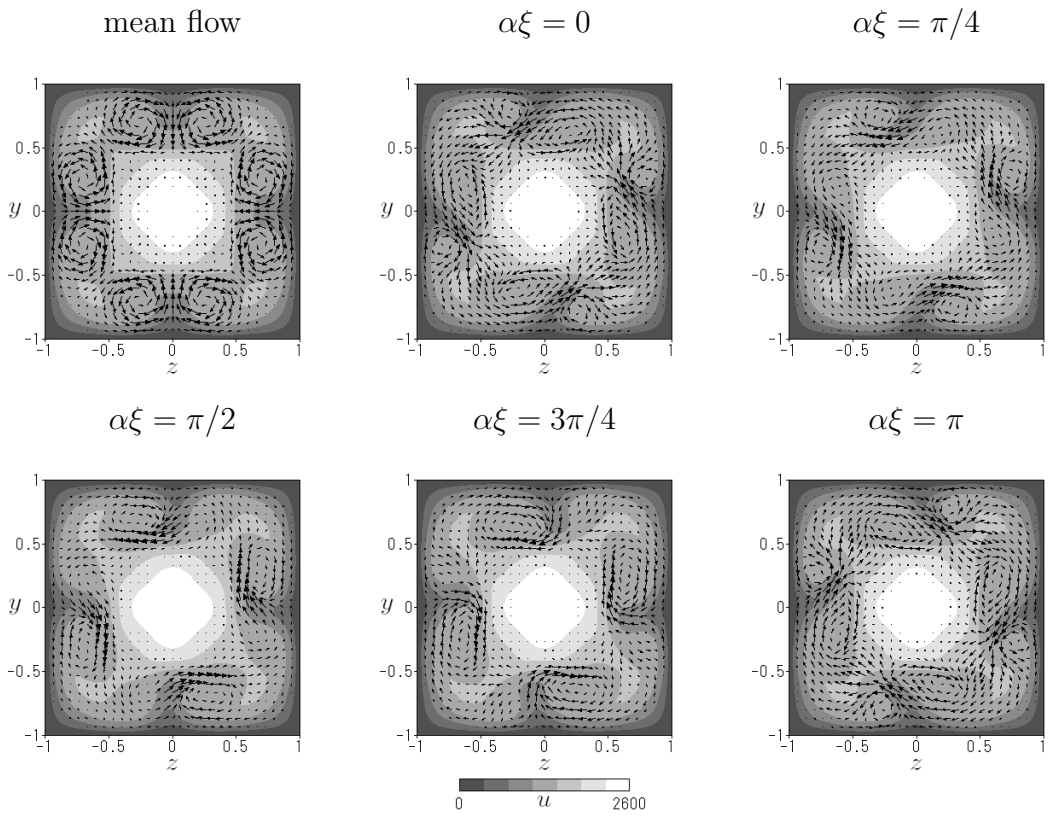

Figure 4.16: Same as figure 4.6 for σ4a with $\alpha = 3.2$ at $Re = 5000$ ($Re_b = 1262$).

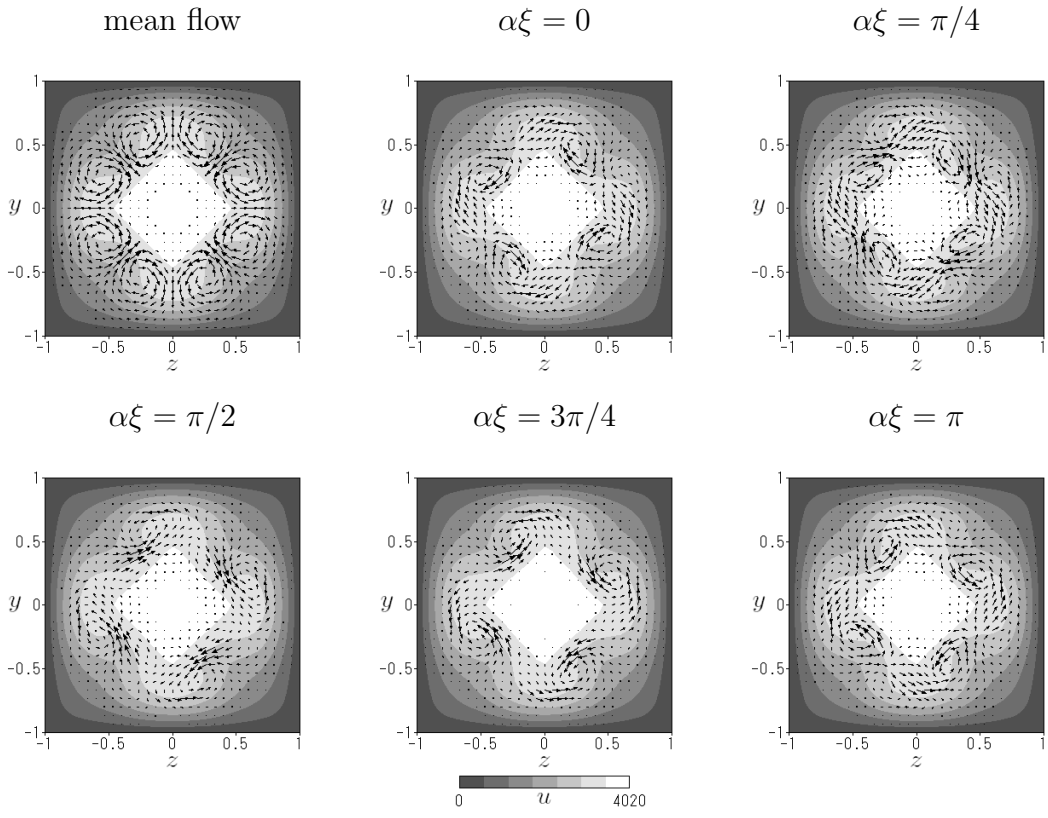

Figure 4.17: Same as figure 4.6 for σ4b with $\alpha = 3.2$ at $Re = 5000$ ($Re_b = 2025$).

μ**2**

We obtain the other solution with the symmetry II, named $\mu 2$, using the mean flow pattern of σ4a with $\alpha = 3.2$ at $Re = 5000$ ($Re_b = 1262$) as the basic stream function (see figure 4.18). This basic stream function creates eight major vortices near the side wall and eight minor ones around the centre of the duct. The bifurcating solution with $\alpha = 2.5$ at $Re = 5000$, which emerges from the neutral point of the third eigenvalue ($\varepsilon = 3.50$), leads to the solution $\mu 2$. It is found that the solution $\mu 2$ is invariant under the transformation $\mathbf{D}$ by examining the coefficient vector. Figure 4.19 shows the flow pattern of $\mu 2$. The mean flow of $\mu 2$ is the 16-vortex structure with the symmetry with respect to the diagonals, which is the same pattern as that of σ4a. The solution consists of four pairs of vortices as σ4a. However, the motion of $\mu 2$ is different from that of σ4a because $\mu 2$ has the diagonal symmetry $\mathbf{D}$, while σ4a has the rotational symmetry by 90 degrees $\mathbf{R}_4$. The flow patterns of $\mu 2$ and M2 in pipe flow shows the similarity (see figure 4.20). The solution $\mu 2$ emerges at the transitional regime and their skin friction is slightly larger than that of turbulence (see figure 4.3).

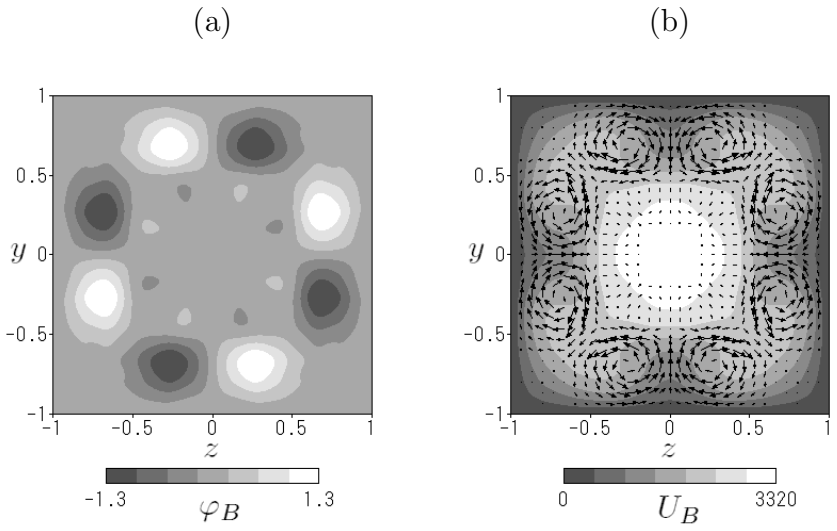

Figure 4.18: (a) The basic stream function φ_B with $\varepsilon = 1$ to calculate the solution $\mu 2$. The strength of φ_B is represented by the grey scale. (b) The laminar solution for $Re = 5000$ with $\varepsilon = 3.50$. The grey scale shows the streamwise velocity U_B.

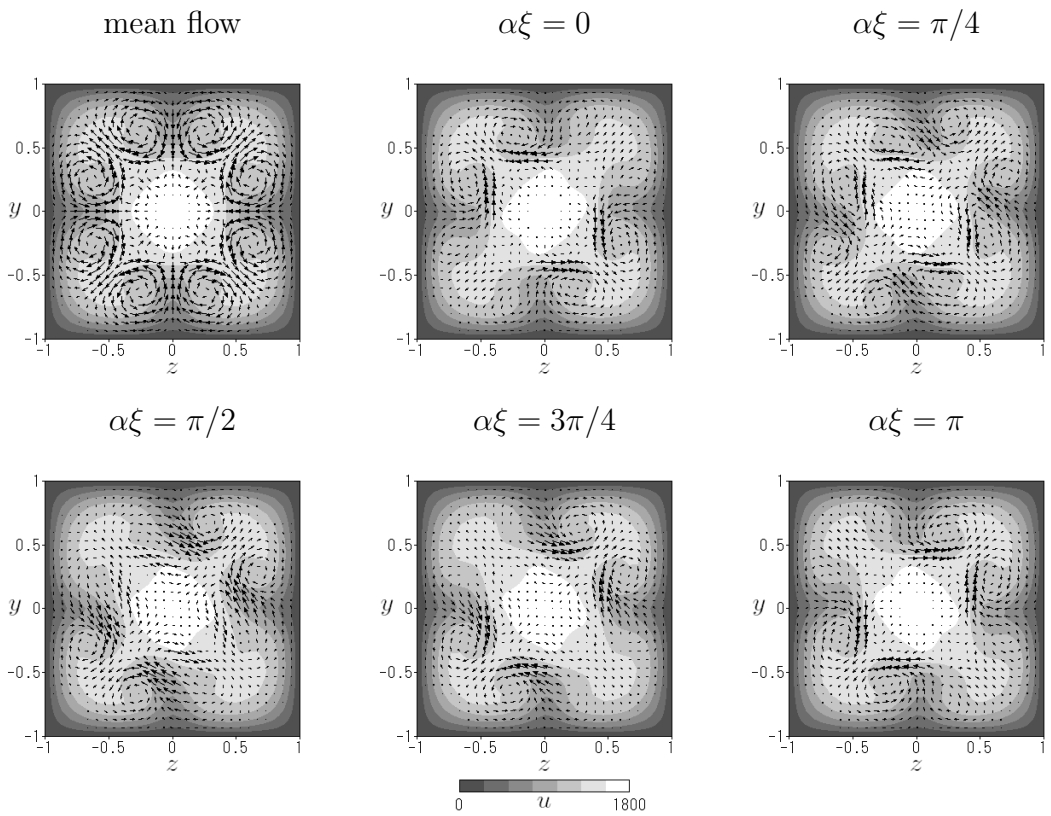

Figure 4.19: Same as figure 4.12 for $\mu 2$ with $\alpha = 2.5$ at $Re = 3300$ ($Re_b = 989$).

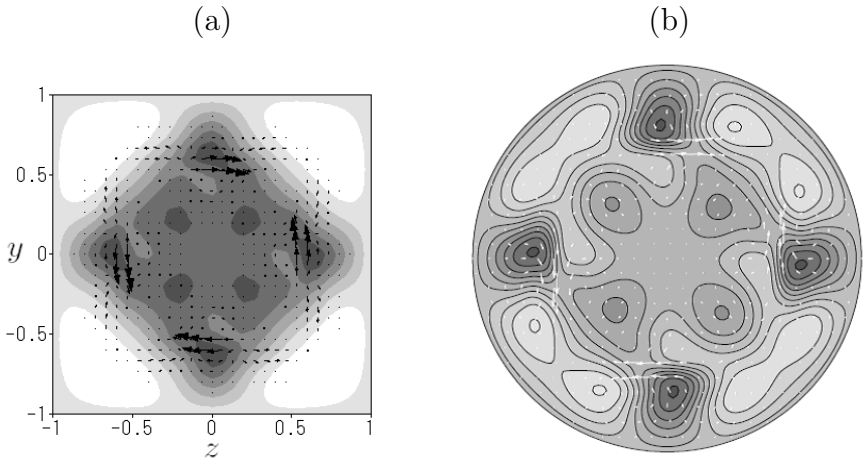

Figure 4.20: Same as figure 4.7 for (a) $\mu 2$ with $\alpha = 2.3$ at $Re = 5000$ ($Re_b = 1976$) and (b) M2 (figure 5a in Pringle *et al.* 2009).

4.2.3 Symmetry III

The symmetry III represented by (2.45) and (2.47) indicates that the flow is unchanged under the transformations shown below: the mirror reflection with respect to z,

$$\mathbf{Z}: \begin{pmatrix} u \\ v \\ w \end{pmatrix} (\xi, y, z) \to \begin{pmatrix} u \\ v \\ -w \end{pmatrix} (\xi, y, -z),$$

and the mirror reflection with respect to y

$$\mathbf{Z}': \begin{pmatrix} u \\ v \\ w \end{pmatrix} (\xi, y, z) \to \begin{pmatrix} u \\ -v \\ w \end{pmatrix} (\xi, -y, z). \tag{4.49}$$

The combination of the two transformations means the rotation by 180 degrees with respect to the origin,

$$\mathbf{R}_2: \begin{pmatrix} u \\ v \\ w \end{pmatrix} (\xi, y, z) \to \begin{pmatrix} u \\ -v \\ -w \end{pmatrix} (\xi, -y, -z).$$

Figure 4.21 presents the schematic representation of the flow with the symmetry III.

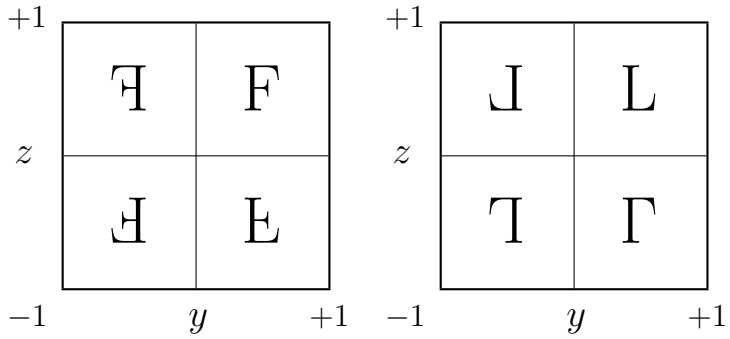

Figure 4.21: Same as figure 4.8 for the symmetry III.

As shown in the following paragraphs, two nonlinear solutions with the symmetry III are obtained.

ζ**2**

Choosing the basic stream function as $\varphi_B = \varepsilon(\phi_5(y)\phi_7(z) - \phi_7(y)\phi_5(z))/2$ with the negative sign of ε leads to one solution with the symmetry III, which is

labelled as $\zeta 2$. We find that the motion has not only the symmetries $\mathbf{Z}$, $\mathbf{Z}'$ and $\mathbf{R}_2$ but also the symmetry $\mathbf{\Omega}_2$ defined as:

$$\mathbf{\Omega}_2 : \begin{pmatrix} u \\ v \\ w \end{pmatrix} (\xi, y, z) \to \begin{pmatrix} u \\ w \\ -v \end{pmatrix} (\xi + \frac{\pi}{\alpha}, -z, y). \tag{4.50}$$

This is because the coefficients of the solutions satisfy the following relation:

$$\begin{cases} v_{lmn} = (-1)^l w_{lnm}, \\ U_{mn} = U_{nm}, \\ \varphi_{mn} = -\varphi_{nm}. \end{cases} \tag{4.51}$$

The transformation $\mathbf{\Omega}_2$ means the shift by half the wavelength and the rotation by 90 degrees around the origin. The mean flow of the solution has a diagonally symmetric eight-vortex pattern with flows directing from the corner toward the centre (see the top-left of figure 4.22). The instantaneous flows are also shown in figure 4.22. The flow pattern of $\zeta 2$ looks like Z2 in a pipe as shown in figure 4.23. However, the relevance between $\zeta 2$ and Z2 is unclear, because $\zeta 2$ appears at much smaller Reynolds number than the transitional value, $Re_b \sim 1000$, while Z2 is reported to appear far above the transitional regime.

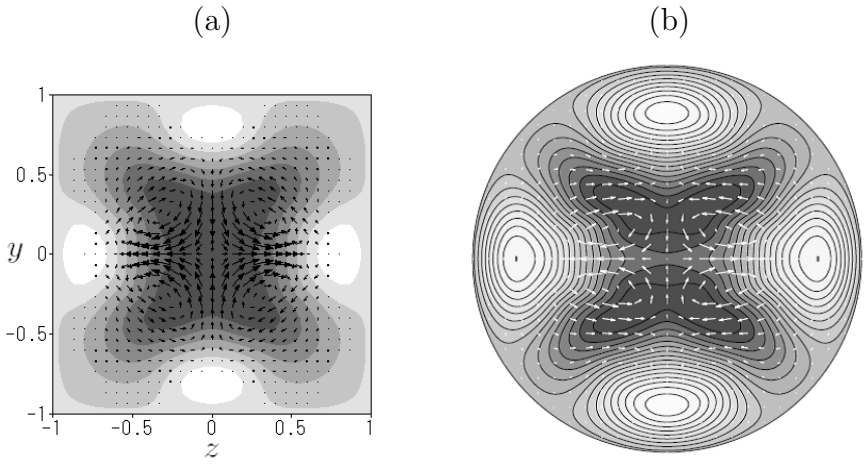

Figure 4.23: Same as figure 4.7 for (a) $\zeta 2$ with $\alpha = 1.0$ at $Re = 3000$ ($Re_b = 1151$) and (b) Z2 (figure 5c in Pringle *et al.* 2009).

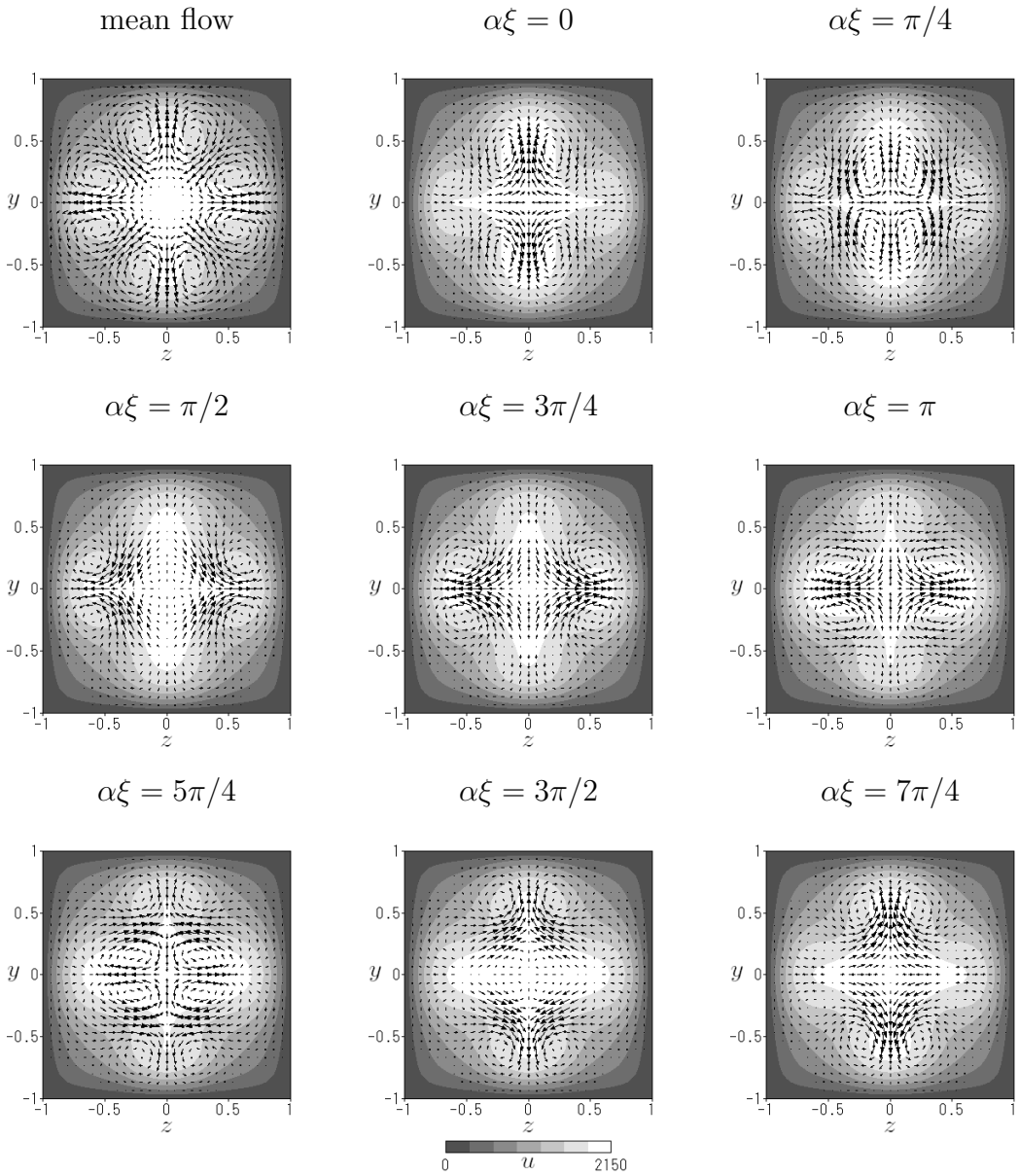

Figure 4.22: Same as figure 4.6 for $\zeta 2$ with $\alpha = 1.0$ at $Re = 3000$ ($Re_b = 1151$).

$\delta 2$

The other solution, which is referred to as $\delta 2$, is obtained by applying the mean flow pattern of $\sigma 2$ with $\alpha = 1.1$ at $Re = 2500$ ($Re_b = 1001$) as the basic stream function (see figure 4.24). The solution has the eight-vortex mean flow structure without the diagonal symmetry. In the top-left of figure 4.25, the vortices near $z = \pm 1$ are slightly smaller and stronger than those near $y = \pm 1$. Though the instantaneous flow is similar to those of $\zeta 2$, the solution $\delta 2$ does not have the symmetry $\mathbf{\Omega}_2$ (compare the top-centre and the middle-right of figure 4.25).

The existence domains of $\zeta 2$ and $\delta 2$ are presented in figure 4.26. It is found that $\delta 2$ is the bifurcating solution from $\zeta 2$ through the pitchfork bifurcation: the solution, which is obtained by rotating $\delta 2$ by 90 degrees, appears simultaneously. The solution $\delta 2$ connects the lower and upper branches of $\zeta 2$ (the bifurcation points are indicated by the circles).

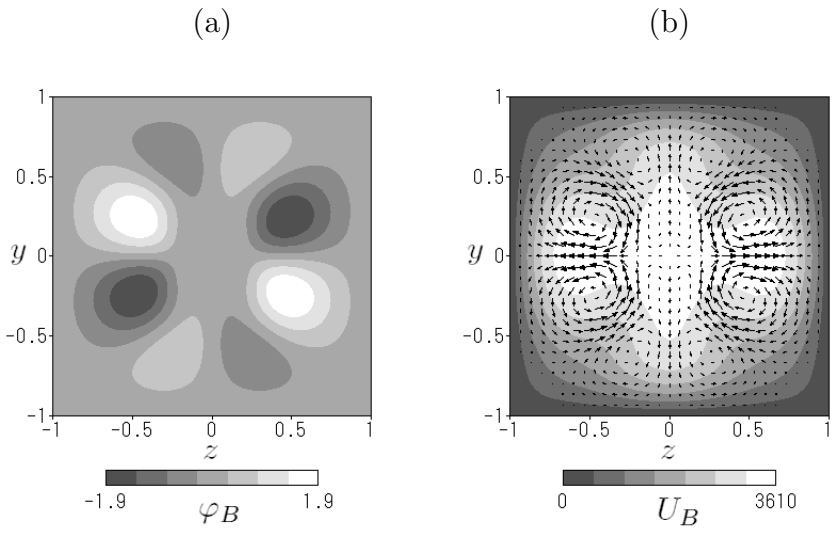

Figure 4.24: (a) The basic stream function φ_B with $\varepsilon = 1$ to calculate the solution $\delta 2$. The strength of φ_B is represented by the grey scale. (b) The laminar solution for $Re = 5000$ with $\varepsilon = -1.87$. The grey scale shows the streamwise velocity U_B.

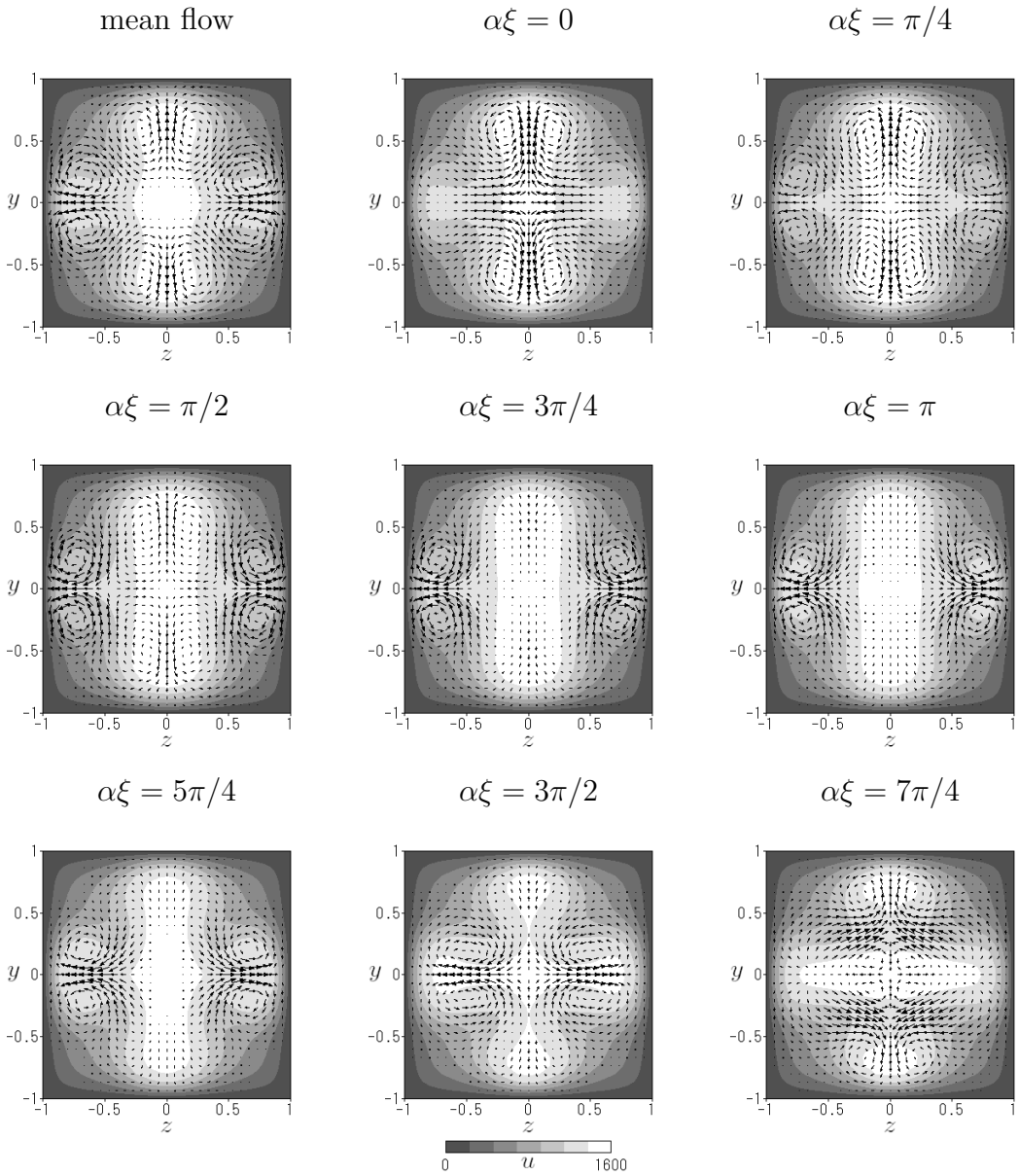

Figure 4.25: Same as figure 4.12 for $\delta 2$ with $\alpha = 1.0$ at $Re = 3000$ ($Re_b = 894$).

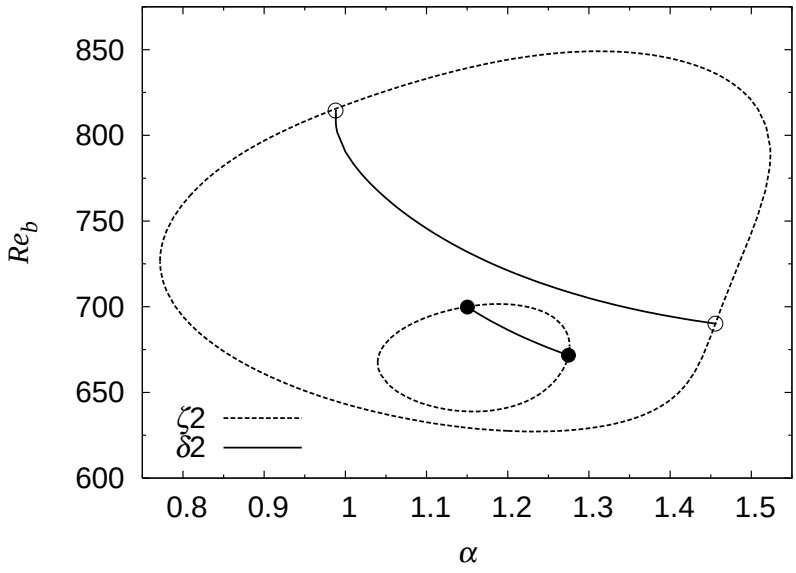

Figure 4.26: The existence domains of the solutions $\zeta 2$ and $\delta 2$ for $Re = 2200$ and 2400. Dotted curve: $\zeta 2$. Solid curve: $\delta 2$. The bifurcation points of $\delta 2$ at $Re = 2200$ and 2400 are indicated by the closed and open circles, respectively.

4.3 Conclusion

We have found a number of travelling waves solutions in square duct flow by introducing the artificially body forces, taking a similar approach to Waleffe (1998, 2003). The solutions, $\nu 1$, $\mu 1$, $\nu 2$, $\sigma 2$, $\zeta 2$ and $\delta 2$, appear at much lower bulk Reynolds number than the transitional regime, $Re_b \sim 1000$, and they take much larger skin friction than the statistic of square duct turbulence (see table 4.1 and figure 4.3). It is noteworthy that these solutions have the wavenumber almost equal to one when they take the minimum Reynolds number (see table 4.1 and figure 4.4). We have found the solution, $\sigma 4$a, $\sigma 4$b and $\mu 2$, which emerge at the transitional regime. These solutions have a rather larger wavenumber at their onset. Their flow patterns are more complex than those of the other solutions.

As listed in table 4.2, most of the solutions presented here have their corresponding solutions in pipe flow. The similarity between square duct flow and pipe flow shown throughout this thesis implies that these two pressure driven flows become turbulent through a common mechanism despite the difference between their cross-sectional geometries. The presence of the corners of a square does not seem to play a crucial role in transition to turbulence.

Table 4.2: The symmetries of the travelling wave solutions in square duct flow and their counterpart in pipe flow. The nomenclature of the solutions in pipe flow is based on Pringle *et al.* (2009).

Solution	Symmetry	Transformation	Solution in pipe flow
$\nu 1$ (WBN)	I	$\mathbf{S}$, $\mathbf{Z}$, $\mathbf{\Omega}$	N1
$\mu 1$ (ONWB)	I	$\mathbf{S}$, $\mathbf{Z}$, $\mathbf{\Omega}$	M1
$\nu 2$ (UKP)	II	$\mathbf{S}$, $\mathbf{R}_2$, $\mathbf{S}'$ $+\mathbf{D}$	N2
$\sigma 2$	II	$\mathbf{S}$, $\mathbf{R}_2$, $\mathbf{S}'$	S2
$\sigma 4$a	II	$\mathbf{S}$, $\mathbf{R}_2$, $\mathbf{S}'$ $+\mathbf{R}_4$	S4
$\sigma 4$b	II	$\mathbf{S}$, $\mathbf{R}_2$, $\mathbf{S}'$ $+\mathbf{R}_4$	S4
$\mu 2$	II	$\mathbf{S}$, $\mathbf{R}_2$, $\mathbf{S}'$ $+\mathbf{D}$	M2
$\zeta 2$	III	$\mathbf{Z}$, $\mathbf{Z}'$, $\mathbf{R}_2$ $+\mathbf{\Omega}_2$	unknown
$\delta 2$	III	$\mathbf{Z}$, $\mathbf{Z}'$, $\mathbf{R}_2$	unknown
$\sigma 1$ ($\mathbf{S}$-symmetric)	I+II	$\mathbf{S}$	S1
$\omega 1$ ($\mathbf{\Omega}$-symmetric)	I+IV	$\mathbf{\Omega}$	unknown

4.4 Appendix

4.4.1 Accuracy of the travelling waves

The results of the accuracy check for the travelling wave solutions presented in Chapter 4 are shown in tables 4.3-4.10. The values in the tables seems to converge well with the truncation level indicated by the dashed underline. Each truncation level is adopted to calculate the minimum Reynolds numbers shown in table 4.1.

Table 4.3: The phase velocity c, the bulk Reynolds number Re_b and the skin friction λ for the upper branch of $\nu 1$ with $\alpha = 0.85$ at $Re = 2000$ as a function of the truncation level (L, M, N).

(L, M, N)	c	Re_b	λ
$(4, 33, 33)$	933.79	600.29	0.07536
$(6, 29, 29)$	935.25	600.97	0.07517
$(6, 33, 33)$	935.23	600.96	0.07517
$(6, 37, 37)$	935.22	600.95	0.07517
$(8, 33, 33)$	934.93	600.93	0.07518

Table 4.4: Same as table 4.3 for the upper branch of $\nu 2$ with $\alpha = 0.90$ at $Re = 1550$.

(L, M, N)	c	Re_b	λ
$(10, 29, 29)$	645.16	456.95	0.10076
$(12, 25, 25)$	645.87	457.23	0.10064
$(12, 29, 29)$	645.29	457.03	0.10073
$(12, 33, 33)$	645.25	457.00	0.10074
$(14, 29, 29)$	645.33	457.05	0.10072

Table 4.5: Same as table 4.3 for $\sigma 2$ with $\alpha = 1.10$ at $Re = 1700$.

(L, M, N)	c	Re_b	λ
$(\ 8, 33, 33)$	749.18	520.41	0.08520
$(10, 29, 29)$	748.54	520.05	0.08532
$(10, 33, 33)$	747.87	519.67	0.08545
$(10, 37, 37)$	747.86	519.67	0.08545
$(12, 33, 33)$	747.65	519.55	0.08549

Table 4.6: Same as table 4.3 for the upper branch of $\sigma 4$a with $\alpha = 3.00$ at $Re = 4400$.

(L, M, N)	c	Re_b	λ
$(3, 53, 53)$	1127.4	1076.3	0.05156
$(4, 49, 49)$	1161.7	1124.9	0.04720
$(4, 53, 53)$	1118.4	1088.0	0.05045
$(4, 57, 57)$	1119.3	1087.1	0.05054
$(5, 53, 53)$	1121.1	1084.9	0.05074

Table 4.7: Same as table 4.3 for the upper branch of $\sigma 4$b with $\alpha = 3.19$ at $Re = 2750$.

(L, M, N)	c	Re_b	λ
$(4, 45, 45)$	1329.1	1016.8	0.03611
$(5, 41, 41)$	1325.4	1016.9	0.03610
$(5, 45, 45)$	1332.2	1017.8	0.03604
$(5, 49, 49)$	1331.0	1017.2	0.03608
$(6, 45, 45)$	1331.4	1017.6	0.03605

Table 4.8: Same as table 4.3 for $\mu 2$ with $\alpha = 2.30$ at $Re = 3200$.

(L, M, N)	c	Re_b	λ
$(3, 49, 49)$	1066.9	924.89	0.05078
$(4, 45, 45)$	1073.1	928.98	0.05033
$(4, 49, 49)$	1068.9	926.47	0.05060
$(4, 53, 53)$	1069.5	926.90	0.05056
$(5, 49, 49)$	1069.8	927.16	0.05053

Table 4.9: Same as table 4.3 for the upper branch of $\zeta 2$ with $\alpha = 1.20$ at $Re = 2250$.

(L, M, N)	c	Re_b	λ
$(6, 37, 37)$	944.93	627.08	0.07767
$(8, 33, 33)$	946.08	627.60	0.07754
$(8, 37, 37)$	945.61	627.38	0.07759
$(8, 41, 41)$	945.70	627.42	0.07758
$(10, 37, 37)$	945.73	627.44	0.07758

Table 4.10: Same as table 4.3 for $\delta 2$ with $\alpha = 1.32$ at $Re = 2250$.

(L, M, N)	c	Re_b	λ
$(6, 37, 37)$	1035.5	672.76	0.06748
$(8, 33, 33)$	1038.6	674.31	0.06717
$(8, 37, 37)$	1039.1	674.59	0.06711
$(8, 41, 41)$	1038.9	674.49	0.06713
$(10, 37, 37)$	1039.4	674.74	0.06708

Chapter 5

Conclusion

In this thesis, eleven nonlinear travelling wave solutions in square duct flow are presented. These solutions are obtained by the following three approaches:

- Homotopy approach from the internally heated duct flow (Chapter 2),
- Investigation of linear stability of $\mu 1$ and subsequent bifurcations via symmetry breaking (Chapter 3),
- Homotopy approach using artificial body forces (Chapter 4).

In Chapter 2, we have performed the nonlinear analysis of viscous flow with the internal heat source in a vertically placed square duct, extending the linear stability analysis by Uhlmlann & Nagata (2006). The path from the linear critical point due to the instability caused by the inflectional property of the basic flow to the isothermal solution ($\mu 1$) is established. The solution $\mu 1$ appears through the saddle-node bifurcation in Re. The mean flow of $\mu 1$ shows eight-vortex structure: one major vortex near the wall and one minor vortex around the centre of the duct for each quadrant. This is similar to the DNS result at the transitional Reynolds number by Uhlmann *et al.* (2007).

The nonlinear solution $\mu 1$ is invariant under the transformations, $\mathbf{S}$, $\mathbf{Z}$ and $\mathbf{\Omega}$. In Chapter 3, the linear stability of $\mu 1$ to the perturbations, which are divided into four groups depending on their symmetry, is investigated. The solution $\mu 1$ is shown to be unstable from its onset at the saddle-node point. We have obtained two asymmetric travelling wave solutions ($\sigma 1$ and $\omega 1$), which arise from breaking the mirror symmetry of $\mu 1$. The solution $\sigma 1$ retains the shift-and-reflect symmetry $\mathbf{S}$, while the other solution $\omega 1$ possesses the shift-and-rotate symmetry $\mathbf{\Omega}$. The flow field of $\sigma 1$ consists of a pair of streamwise vortices and a low-speed streak near one of the side walls. This flow pattern is

very similar to that of the edge state in square duct flow identified by Biau & Bottaro (2009). The characteristic quantities such as the skin friction and the bulk Reynolds number for $\sigma 1$ and $\mu 1$ take the close value to those of the edge state. Our stability analysis shows that $\sigma 1$ is less unstable than $\mu 1$. These results suggest that $\sigma 1$ is embedded in the edge state. Especially, we expect the edge state is organized around $\sigma 1$ (at least four $\sigma 1$ solutions exist because of the geometrical symmetry of a square) and their heteroclinic connections.

Following Waleffe (1998), the continuation method using artificially arranged body forces is formulated in Chapter 4. The advantage of this approach is to enable us to calculate various kinds of solutions by choosing an arbitrary forcing function. We have reproduced three solutions ($\nu 1$, $\mu 1$ and $\nu 2$), which have already been reported in Wedin *et al.* (2009), Okino *et al.* (2010) and Uhlmann *et al.* (2010), and obtained six new solutions ($\sigma 2$, $\sigma 4$a, $\sigma 4$b, $\mu 2$, $\zeta 2$ and $\delta 2$). A lot of nonlinear solutions ($\nu 1$, $\mu 1$, $\nu 2$, $\sigma 2$, $\zeta 2$ and $\delta 2$) appear at much lower bulk Reynolds number than the transitional value ($Re_b \sim 1000$), and their flow patterns are rather simple. It is noteworthy that these solutions have the wavenumber almost equal to one when they take the minimum Reynolds number. We find that $\mu 1$ takes the lowest Reynolds number at the saddle-node among the solutions presented so far. On the other hand, the solutions, $\sigma 4$a, $\sigma 4$b and $\mu 2$, emerge at the transitional regime, and have more complex flow structures.

It is found that most of the solutions presented in this thesis have their counterparts in pipe flow (Pringle *et al.* 2009). The similarity between square duct flow and pipe flow suggests that the two pressure driven flows in a straight tube with different cross sections have some transition mechanism in common.

Throughout this thesis, it is shown that a number of nonlinear travelling wave solutions appear below the transitional Reynolds number and more and more solutions would bifurcate due to their instabilities. The richness of the nonlinear solutions implies the complexity of the phase space and they are considered to be the fundamental building blocks to describe the turbulence in a square duct. Though we restricted our attention to the travelling waves, relative periodic orbits are also thought to be important in turbulent dynamics. Recently, such solutions are efficiently calculated by Viswanath (2007) for plane Couette flow and Duguet, Pringle & Kerswell (2008) for pipe flow using the Newton-Krylov method. Calculation of relative periodic orbits in square

duct flow should be addressed in the future. Also, in order to give an explanation to laminar-turbulent transition from the view point of a dynamical system, the linear stability of the nonlinear solutions and their heteroclinic and homoclinic connections should be investigated thoroughly. Heteroclinic connections between nonlinear solutions are calculated by Halcrow *et al.* (2009) for plane Couette flow and Duguet, Willis & Kerswell (2008) for pipe flow.

The other interest is the nonlinear solutions in rectangular duct flow (the case when the aspect ratio is larger than unity). As our preliminarily work, we have obtained a solution, whose disturbances are localized in the spanwise direction when the aspect ratio of $\mu 1$ is enlarged as shown in figure 5.1. Recently Schneider *et al.* (2010) have obtained solutions with a localized structure for plane Couette flow. These solutions are expected to be a clue to elucidate the localized structures, which are normally observed in the onset of the turbulence, such as a puff in turbulent pipe flow and a turbulent spot in plane Couette flow and plane Poiseuille flow.

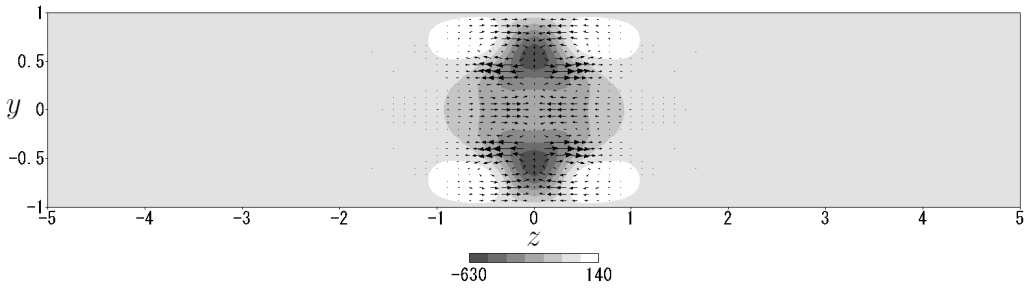

Figure 5.1: The mean velocity profile of the disturbances of the solution in rectangular duct flow. The aspect ratio of the cross section is five. The velocity in the streamwise direction is shown by the grey scale. Grey and white represent slow and fast, respectively. The arrows show the velocity in the cross section. The disturbances are almost confined to $-1 \leq z \leq +1$.

Bibliography

Barnes, D. B. & Kerswell, R. R. 2000 New result in rotating Hagen-Poisuille flow. *J. Fluid Mech.* **417**, 103-126.

Biau, D. & Bottaro, A. 2009 An optimal path to transition in a duct. *Phil. Trans. Roy. Soc.* A **367**, 529-544.

Biau, D., Soueid, H. & Bottaro, A. 2008 Transition to turbulence in duct flow. *J. Fluid Mech.* **596**, 133-142.

Chapman, S. J. 2002 Subcritical transition in channel flows. *J. Fluid Mech.* **451**, 35-97.

Clever, R. M. & Busse, F. H. 1992 Three-dimensional convection in a horizontal fluid layer subjected to a constant shear. *J. Fluid Mech.* **234**, 511-527.

Darbyshire, A. G. & Mullin, T. 1995 Transition to turbulence in constant-mass-flux pipe flow. *J. Fluid Mech.* **289**, 83-114.

Davey, A. & Drazin, P. G. 1969 The stability of Poiseuille flow in a pipe. *J. Fluid Mech* **36**(2), 209-218.

Drazin, P. G. & Reid, W. H. 1981 *Hydrodynamic Stability*, Cambridge University Press.

Duguet, Y., Pringle, C. C. T. & Kerswell, R. R. 2008 Relative periodic orbits in transitional pipe flow *Phys. Fluids* **20**, 114102.

Duguet, Y., Willis, A. P. & Kerswell, R. R. 2008 Transition in pipe flow: the saddle structure on the boundary of turbulence. *J. Fluid Mech.* **613**, 255-274.

Faisst, H. & Eckhardt, B. 2003 Traveling waves in pipe flow. *Phys. Rev. Lett.* **91**, 224502.

Gavarini, M. I., Bottaro, A. & Nieuwstadt, F. T. M. 2005 Optimal and robust control of streaks in pipe flow. *J. Fluid Mech.* **537**, 187-219.

Gavrilakis, S. 1992 Numerical simulation of low-Reynolds-number turbulent flow through a straight square duct. *J. Fluid Mech.* **224**, 101-129.

Generalis, S. C. & Nagata, M. 2003 Transition in homogeneously heated inclined plane parallel shear flows. *J. Heat Trans.* **125**, 795-803.

Halcrow, J., Gibson, J. F., Cvitanovic, P. & Viswanath, D. 2009 Heteroclinic connections in plane Couette flow. *J. Fluid Mech.* **621**, 365-376.

Hof, B., Juel, A. & Mullin, T. 2003 Scaling of the turbulence transition threshold in a pipe. *Phys. Rev. Lett.* **91**, 244502.

Huser, A. & Biringen, S. 1993 Direct numerical simulation of turbulent flow in a square duct. *J. Fluid Mech.* **257**, 65-95.

Itano, T. & Toh, S. 2001 The dynamics of bursting process in wall turbulence. *J. Phys. Soc. Jpn.* **70**, 703-716.

Jones, O. C. 1976 An improvement in the calculation of turbulent friction in rectangular ducts. *ASME J. Fluids Engng* **98**, 173-181.

Kawahara, G. & Kida, S. 2001 Periodic motion embedded in plane Couette turbulence: regeneration cycle and burst. *J. Fluid Mech.* **449**, 291-300.

Kerswell, R. R. & Tutty, O. R. 2007 Recurrence of travelling waves in transitional pipe flow. *J. Fluid Mech.* **584**, 69-102.

Meseguer, A. & Trefethen, L. N. 2003 Linearized pipe flow to Reynolds number 10^7. *J. Comput. Phys.* **186**, 178-197.

Mellibovsky, F. & Meseguer. A. 2009 Critical threshold in pipe flow transition. *Phil. Trans. R. Soc.* A **367**, 545-560.

Nagata, M. 1986 Bifurcation in Couette flow between almost corotating cylinders. *J. Fluid Mech.* **169**, 229-250.

Nagata, M. 1988 On wavy instabilities of the Taylor-vortex flow between corotating cylinders. *J. Fluid Mech.* **188**, 585-598.

Nagata, M. 1990 Three-dimensional finite-amplitude solutions in plane Couette flow: bifurcation from infinity. *J. Fluid Mech.* **217**, 519-527.

Okino, S., Nagata, M., Wedin, H. & Bottaro, A. 2010 A new nonlinear vortex state in square-duct flow. *J. Fluid Mech.* **657**, 413-429.

Pinelli, A., Uhlmann, M., Sekimoto, A. & Kawahara, G. 2010 Reynolds number dependence of mean flow structure in square duct turbulence. *J. Fluid Mech.* **644**, 107-122.

Pringle, C. C. T. & Kerswell, R. R. 2007 Asymmetric, helical and mirror-symmetric travelling waves in pipe flow. *Phys. Rev. Lett.* **99**, 074502.

Pringle, C. C. T., Duguet, Y. & Kerswell, R. R. 2009 Highly symmetric travelling waves in pipe flow. *Phil. Trans. R. Soc.* A **367**, 457-472.

Reynolds, O. 1883 An experimental investigation of the circumstances which determine whether the motion of water shall be direct or sinuous and of the law of resistance in parallel channels. *Phil. Trans. R. Soc.* **174**, 935-982.

Romanov, V. A. 1973 Stability of plane-parallel Couette flow. *Functional Anal. Appl.* **7**, 137-146.

Salwen, H. & Grosch, C. E. 1972 The stability of Poiseuille flow in a pipe of circular cross-section. *J. Fluid Mech.* **54**(1), 93-112.

Salwen, H., Cotton, F. W. & Grosch, C. E. 1980 Linear stability of Poiseuille flow in a circular pipe. *J. Fluid Mech.* **98**(2), 273-284.

Schneider, T. M., Eckhardt, B. & Yorke, J. A. 2007 Turbulence transition and the edge of chaos in pipe flow. *Phys. Rev. Lett.* **99**, 034502.

Schneider, T. M., Gibson, J. F., Lagha, M., Lillo, F. D. & Eckhardt, B. 2008 Laminar-turbulent boundary in plane Couette flow *Phys. Rev.* E **78**, 037301.

Schneider, T. M. & Eckhardt, B. 2009 Edge states intermediate between laminar and turbulent dynamics in pipe flow. *Phil. Trans. R. Soc.* A **367**, 577-587.

Schneider, T. M., Gibson, J. F. & Burke, J. 2010 Snakes and ladders: localized solutions of plane Couette flow. *Phys. Rev. Lett.* **104**, 104501.

Tatsumi, T. & Yoshimura, T. 1990 Stability of the laminar flow in a rectangular duct. *J. Fluid Mech.* **212**, 437-449.

Uhlmann, M. & Nagata, M. 2006 Linear stability of flow in an internally heated rectangular duct. *J. Fluid Mech.* **551**, 387-404.

Uhlmann, M., Pinelli, A., Kawahara, G. & Sekimoto, A. 2007 Marginally turbulent flow in a square duct. *J. Fluid Mech.* **588**, 153-162.

Uhlmann, M., Kawahara, G. & Pinelli, A. 2010 Travelling-waves consistent with turbulence-driven secondary flow in a square duct. *Phys. Fluids* **22**, 084102.

Viswanath, D. 2007 Recurrent motions within plane Couette turbulence. *J. Fluid Mech.* **580**, 339-358.

Wang, J., Gibson. J. F. & Waleffe, F. 2007 Lower branch coherent states in shear flows: transition and control. *Phys. Rev. Lett.* **98**, 204501.

Waleffe, F. 1997 On a self-sustaining process in shear flows. *Phys. Fluids* **9**, 883-900.

Waleffe, F. 1998 Three-dimensional coherent states in plane shear flows. *Phys. Rev. Lett.* **81**, 4140-4143.

Waleffe, F. 2001 Exact coherent structures in channel flow. *J. Fluid Mech.* **435**, 93-102.

Waleffe, F. 2003 Homotopy of exact coherent structures in plane shear flows. *Phys. Fluids* **15**, 1517-1534.

Waleffe, F. & Wang, J. 2005 Transition threshold and the self-sustaining process. In *IUTAM Symposium on Laminar-Turbulent Transition and Finite Amplitude Solutions* (ed. T. Mullin & R. Kerswell), pp. 85-106. Springer.

Wedin, H. & Kerswell, R. R. 2004 Exact coherent structures in pipe flow: travelling wave solutions. *J. Fluid Mech.* **508**, 333-371.

Wedin, H., Biau, D., Bottaro, A. & Nagata, M. 2008 Coherent flow states in a square duct. *Phys. Fluids* **20**, 094105.

Wedin, H., Bottaro, A. & Nagata, M. 2009 Three-dimensional traveling waves in a square duct. *Phys. Rev.* E **79**, 065305.

Willis, A. P. & Kerswell, R. R. 2008 Coherent structures in localized and global pipe turbulence. *Phys. Rev. Lett.* **100**, 124501.